DESIGN OF EFFICIENT PLASMA DISPLAY PANEL CELLS USING A MULTIFLUID KINETIC MODEL OF ELECTRICAL MICRODISCHARGES

A DISSERTATION
SUBMITTED TO THE DEPARTMENT OF ELECTRICAL ENGINEERING
AND THE COMMITTEE ON GRADUATE STUDIES
OF STANFORD UNIVERSITY
IN PARTIAL FULFILLMENT OF THE REQUIREMENTS
FOR THE DEGREE OF
DOCTOR OF PHILOSOPHY

Georgios Veronis
June 2002

I certify that I have read this dissertation and that in my opinion it is fully adequate, in scope and quality, as a dissertation for the degree of Doctor of Philosophy.

Umran S. Inan
(Principal Adviser)

I certify that I have read this dissertation and that in my opinion it is fully adequate, in scope and quality, as a dissertation for the degree of Doctor of Philosophy.

Victor P. Pasko

I certify that I have read this dissertation and that in my opinion it is fully adequate, in scope and quality, as a dissertation for the degree of Doctor of Philosophy.

Shanhui Fan

Approved for the University Committee on Graduate Studies:

Abstract

Plasma display panels (PDPs) are one of the leading candidates in the competition for large-size, high-brightness flat panel displays, suitable for high definition television (HDTV) wall-mounted monitors. Recent progress of PDP technology development and manufacturing has been remarkable. One of the most critical issues in ongoing PDP research is the improvement of the luminous efficiency, which is still low compared to conventional cathode ray tube displays (CRTs). Another important problem is the relatively high operating voltages.

We first use a fundamental kinetic model to compare the electron excitation efficiency of different compositions of inert gas mixtures in plasma display panels. Electron excitation efficiency is an increasing function of the Xe concentration in both the Ne-Xe and He-Xe cases. The fractional increase in efficiency is very small for Xe concentrations higher than $\sim$10%. We also use a two-dimensional self-consistent simulation model to study the effect of the geometric parameters on the operating voltages and the efficiency of a coplanar-electrode plasma display panel cell. For the standard coplanar-electrode geometry it is found that there is a trade-off between high efficiency and low operating voltages as the electrode gap, or other parameters of the upper dielectric are varied, while variation of the sustain electrode width has no significant effect on either the operating voltages or efficiency. Finally, we put forth several non-standard cell geometry designs involving two-dimensional variations of the coplanar-electrode PDP cell and analyze their performance using the simulation model. A PDP cell with modified shape of sustain electrodes is found to have $\sim$20% larger luminous efficiency without substantial increase of the operating voltages. Similar performance improvement is achieved by new designs with different shapes of the upper dielectric, or by those involving two different dielectric layers. The dependence of PDP performance on the geometrical design parameters of these new structures is quantified.

Acknowledgements

I would like to thank Professor Umran S. Inan, my principal adviser, first for giving me the opportunity to come to Stanford. I also deeply appreciate his respect and trust in me as well as his guidance, encouragement and moral support during the whole period of my studies. I have been really impressed by his infinite reservoir of energy and enthusiasm.

I would also like to thank my associate advisor Professor Victor P. Pasko. Victor helped me decisively during my first years at Stanford. I really appreciate the fact that he was always available to discuss my research and provide invaluable suggestions and comments.

I would like to thank Professor Robert W. Dutton for chairing my oral examination committee, Professor Shanhui Fan both for being a member of my oral examination committee and for carefully reading this dissertation, and Professor Mark A. Cappelli for being a member of my oral examination committee.

I would like to express my appreciation to Professors Don Carpenter, Martin Walt, Robert Helliwell and Dr. Timothy Bell for their support. I am grateful to present and former students of the VLF group for their friendship and help as well as the many interesting discussions on various topics: Steve Cummer, Steve Reising, David Lauben, Mehmet Demirkol, Michael Johnson, Sean Lev-Tov, Chris Barrington-Leigh, Nikolai Lehtinen, Elizabeth Gerken, Maria Spasojevic, Troy Wood, Michael Chevalier, Jacob Bortnik, Timothy Chevalier, Robert Moore, Joseph Payne, Manuel Platino, Benjamin Mossawir, and Charles Wang. I would like to specially thank Timothy Chevalier for maintaining, troubleshooting, and administrating the computers that I used for my research. I would also like to thank Shaolan Min for her valuable everyday help with administrative work.

This dissertation would not have become a reality without the knowledge and experience which I had acquired before my Stanford years in Greece. I am grateful to my high school teachers Lefteris Spetsakis and Yiannis Dimitriou for conveying their love for math and physics to me. I would like to thank my Professors at the National Technical University of

Athens for educating me and supporting me during my undergraduate years.

My grandfathers Georgios and Yiannis have always been a moral example and source of inspiration for me.

Above all, I would like to thank Marianna for her love and support and my brother Stefanos, my mother Mina, and my father Yiannis, for everything. A few words here cannot express my gratitude to them.

This research was supported by the National Science Foundation under grants ATM-9731170 and ATM-9908766 to Stanford University, and by the Office of Technology Licensing of Stanford University under grant 127P316.

Contents

List of Tables

List of Figures

Chapter 1

Introduction

Plasma display panels are one of the leading candidates in the competition for large-size, high-brightness, high-contrast-ratio flat panel displays, suitable for high definition television (HDTV) wall-mounted monitors [e.g., *Sobel*, 1998; *Kamegaya*, 1990, p. 131]. Their advantages include large screen size, high resolution, wide viewing angle, low weight, small thickness and simple manufacturing process for fabrication. Recent progress of PDP technology development and manufacturing has been remarkable [e.g., *Kanazawa et al.*, 1999; *Hashimoto et al.*, 2001]. However, there are still problems that need to be resolved to popularize the PDP as a home commodity. One of the most critical issues in ongoing PDP research is the improvement of the luminance and luminous efficiency of the display, which are still low compared to conventional cathode ray tube displays (CRTs). Another important problem is the relatively high operating voltages which adversely affect the cost of the electronics and consequently the overall cost of the display. Figure 1.1 shows a 60 inch diagonal plasma display panel.

1.1 Structure of the plasma display panel

Typical color plasma displays consist of two glass plates, each with parallel electrodes deposited on their surfaces (Fig. 1.2). The most common type of color plasma display is the coplanar-electrode PDP. In this PDP type, each cell is formed by the intersection of a pair of transparent sustain electrodes X and Y on the front plate, and an address electrode A on the back plate. The electrodes are covered with dielectric films typically made of enamel or alumina. A protective MgO layer is deposited above the dielectric film on the

Figure 1.1 A 60 inch diagonal color plasma display panel. The display has an array of 1366×768 full color pixels, and a total viewing area of 1328×747mm. It weighs 75kg and has a 5 inch thickness.

front plate. The role of this layer is to decrease the breakdown voltage due to the relatively high secondary electron emission coefficient of MgO. On the back plate barrier ribs are formed, which separate both electrically and optically adjacent cells with different colors. In each cell phosphors are deposited that emit one primary color, red, green or blue. Each PDP pixel consists of three adjacent cells. The two plates are sealed together with their electrodes at right angles, and the gap between the plates is first evacuated and then filled with an inert gas mixture. When sufficiently high voltages are applied to the electrodes of the PDP cell, breakdown occurs which results in ionization and UV emission. Some of the UV photons emitted by the discharge hit and excite the phosphors deposited on the walls of the PDP cell. The phosphors emit visible photons, some of which come out of the front plate and reach the observer.

1.2 Operation of the plasma display panel

As we mentioned above, the two plates are sealed with their electrodes at right angles, so that one of the two plates shown in Fig. 1.2 has to be rotated by 90°. PDP cells are formed

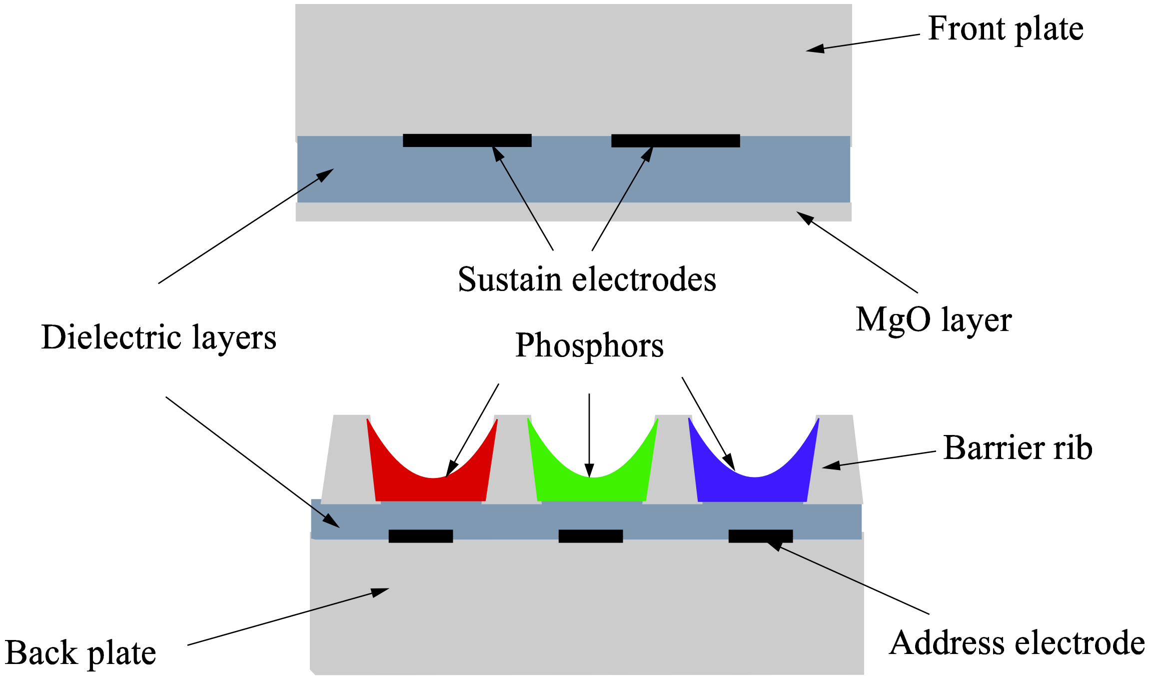

Figure 1.2 Typical structure of a coplanar-electrode color plasma display panel. Only a portion of the cross section of the two plates is shown. Both plates are uniform in the third dimension and periodic in the horizontal direction. The two plates are sealed together with their electrodes at right angles. In other words, one of the two plates shown here has to be rotated by 90°. Each pair of sustain electrodes deposited on the front plate corresponds to a line of the display. Each address electrode deposited on the back plate corresponds to a column of the display. A PDP cell is formed at the intersection of a pair of sustain electrodes on the front plate, and an address electrode on the back plate. Each PDP pixel consists of three adjacent cells.

at the intersection of electrodes on the front and back plates (Fig. 1.3).

The operation of the plasma display panel consists of two phases: the addressing phase, and the sustaining phase. During the addressing phase, 'scan' pulses are applied successively to each one of the parallel Y sustain electrodes, also known as scan electrodes. During the application of the 'scan' pulse at a specific line of the display, 'data' pulses are applied only to those address electrodes A which correspond to cells in that specific line which have to be turned on (Fig. 1.3). The application of the 'scan' voltage pulse $-V_{\mathrm{SW}}$ and of the 'data' pulse V_{D} on the Y and A electrodes respectively results in an electric field $\mathbf{E}$ in the gap between the two dielectrics sufficient to cause breakdown (Fig. 1.4a). The discharge results in ionization and consequently production of positively and negatively charged particles, ions and electrons. Positive and negative charges move under the influence of the applied electric field in opposite directions and are deposited to the walls of the dielectric layers. The electric field of the deposited surface charge opposes the electric field of the applied voltage and the discharge is eventually quenched (Fig. 1.4b).

During the sustaining phase, sustain voltage pulses V_{S} are applied to the sustain electrodes in all cells. The electric field produced by the applied voltage is by itself not enough to cause breakdown. However, in those cells that have been previously addressed, the electric field due to the applied voltage adds to the electric field induced by the deposited surface charge, so that the total field is sufficient for breakdown (Fig. 1.4c). Positive and negative charges are again produced through ionization and move in opposite directions, until the electric field of the newly deposited surface charge opposes the electric field of the applied voltage and the discharge is eventually quenched (Fig. 1.4d). However, on the next sustain cycle the sustain pulse is applied to the other sustain electrode so that now the induced electric field of the surface charge adds onto the field due to the voltage (Fig. 1.4e.) The discharge is again eventually quenched (Fig. 1.4f), and the same process is repeated during the sustaining phase.

PDP cells can operate only if the applied sustaining voltage V_{S} is held within certain limits known as the minimum sustaining voltage V_{Smin} and the firing voltage V_{f}. The initial address pulses trigger a discharge between the A and Y electrodes. This discharge is quenched by surface charges accumulated on the dielectrics. Subsequent sustain discharges occur only in the addressed cells, since the sustain voltage V_{S} is below the breakdown voltage, as discussed above. The minimum sustaining voltage V_{Smin} is defined as the minimum value of V_{S} which leads to a steady sequence of sustaining discharges in an addressed cell [*Shinoda*

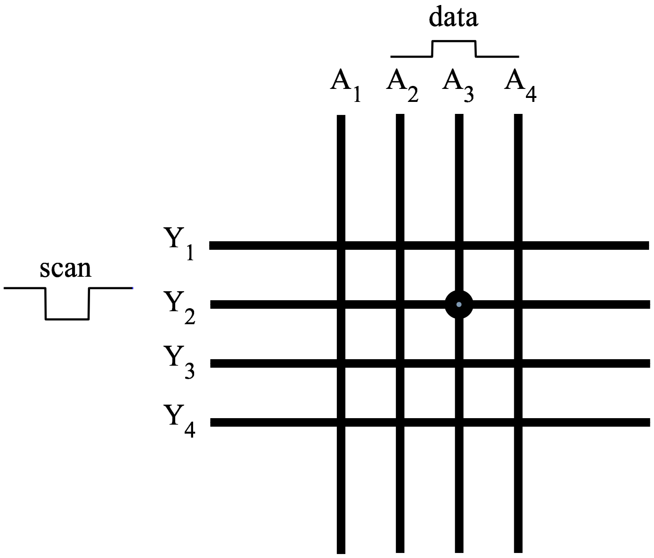

Figure 1.3 The two plates of the PDP are sealed together so that their electrodes are at right angles (Fig. 1.2). Here we show the address electrodes A deposited on the back plate, and the Y sustain electrodes deposited on the front plate. The X sustain electrodes are not shown. Each pair of sustain electrodes, X and Y, corresponds to a line of the display. Each address electrode A corresponds to a column of the display. During the addressing phase, a cell is turned ON by applying 'scan' and 'data' pulses to the corresponding Y and A electrodes respectively.

et al., 2000]. The firing voltage $V_{\rm f}$ is defined as the breakdown voltage in an unaddressed cell. The sustaining voltage $V_{\rm S}$ must at all times be less than $V_{\rm f}$ in order to avoid discharges in cells which are not addressed. The voltage margin of the cell is thus defined as $V_{\rm f} - V_{\rm Smin}$. In real PDPs $V_{\rm f}$ and $V_{\rm Smin}$ exhibit some statistical variation, since cells have slightly different dimensions [*Shinoda et al.*, 2000]. The voltage margin of the cell should therefore be as large as possible to ensure reliable operation of the display.

In order to achieve color resolution, each TV field (with typical duration of 16.7ms) is divided into subfields [e.g., *Shinoda*, 1998]. Each subfield consists of an addressing and a sustaining phase. The duration of the sustaining phases in the different subfields are proportional to powers of 2 so that each one of them corresponds to one bit of resolution. Sustain frequencies are typically 50-350 kHz, so that a very large number of sustain pulses occur during each TV field.

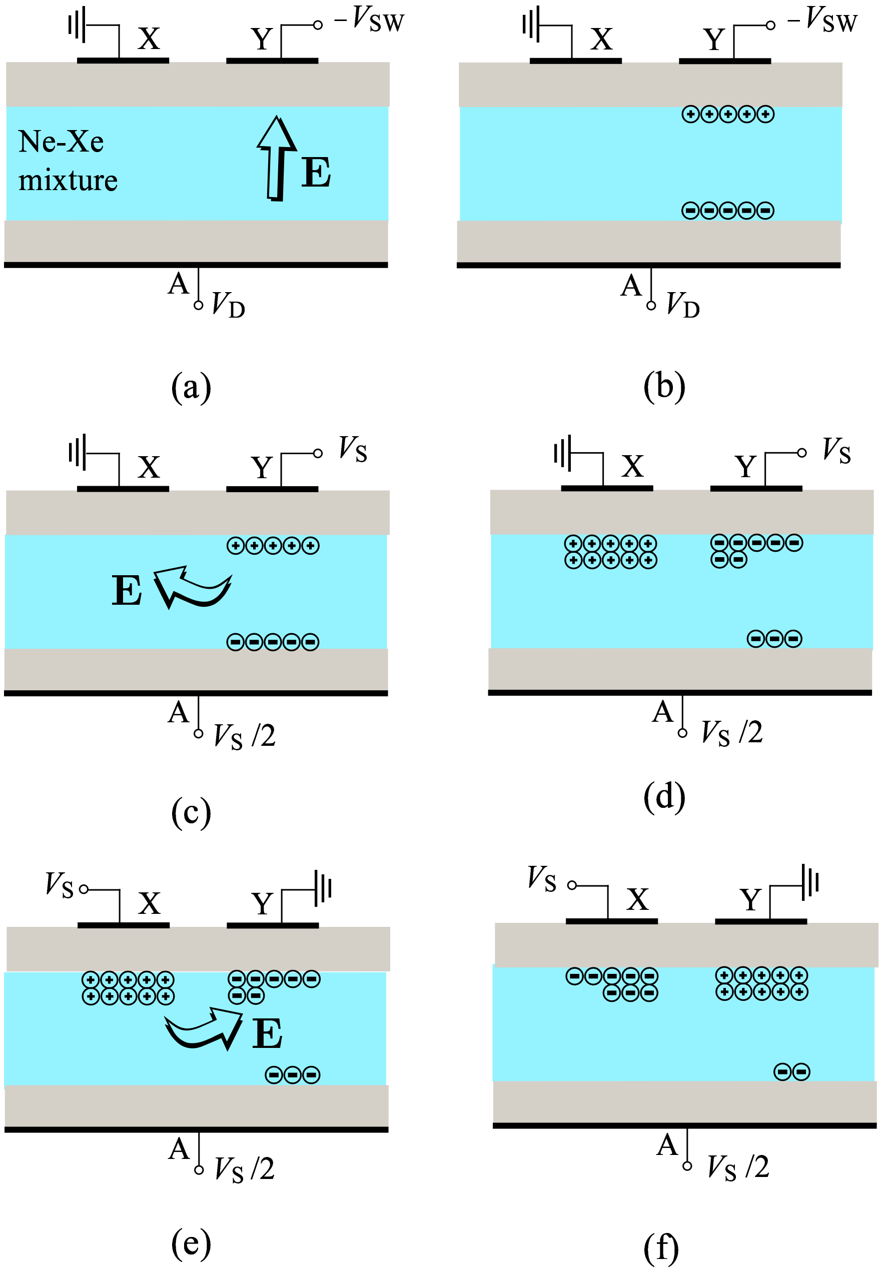

Figure 1.4 Operation of the PDP cell; (a), (b): Addressing phase; (c), (d), (e), (f): Sustaining phase

1.3 Scientific contributions

The specific scientific contributions of this work can only be appreciated in the context of the current state of PDP technology and related previous modeling work. As mentioned above, the recent progress of PDP technology development has been remarkable. The major remaining issues are the improvement of luminance and luminous efficiency, and the cost reduction.

PDP cells are small (cell height is $\sim$150μm) and provide limited access for diagnostic measurements. As a result, experimental studies of the transient plasma discharges in PDPs are extremely difficult, and computer-based modeling is currently essential for understanding PDP physics and optimizing its operation [e.g., *Yoon et al.*, 2001]. Computer simulations are effective in identifying the basic properties of the discharge dynamics and the dominant mechanisms of light emission. In addition, simulation models are usually successful in predicting the effects on the performance of the device of variations in design parameters, such as cell geometry, applied voltage waveforms, and gas mixture. Although simulation results are usually in qualitative rather than quantitative agreement with experimental display measurements, they are used very effectively to provide directions for future PDP design.

Several PDP models have already been developed [e.g., *Rauf and Kushner*, 1999a; *Punset et al.*, 1998]. Simulation studies concerning the efficiency and the operating voltages of the PDP cell were carried out [e.g., *Rauf and Kushner*, 1999b; *Punset et al.*, 1999; *Hagelaar et al.*, 2001]. However, none of these works considered the effect of geometric cell design parameters on the performance of the device.

In addition, several alternative designs have been proposed as a means to increase the luminous efficiency of the PDP. These designs modified the arrangement of individual cells of the display or the three-dimensional structure of the electrodes [*Hashimoto et al.*, 2001; *Yoon et al.*, 2001]. Other methods were based on RF sustain pulses [*Kang et al.*, 2000] or different inert gas mixture composition [*Oversluizen et al.*, 2000]. However, the effect of simpler two-dimensional variations of the PDP cell geometry on the performance of the device was not investigated in detail, although limited studies of two-dimensional variations have been carried out [*Shin et al.*, 1999; *Shon et al.*, 2001].

The specific scientific contributions of this work are:

1. The development of a fundamental kinetic model for inert gas mixtures used in plasma

display panels and the determination of the dependence of electron excitation efficiency on percentage Xe concentration [*Veronis et al.*, 2000].

2. The development of a two-dimensional simulation model of a standard coplanar-electrode plasma display panel cell and the quantitative investigation of the effect of geometrical parameters on the operating voltages and the luminous efficiency of the cell [*Veronis and Inan*, 2002a].
3. The demonstration of the unavoidable trade-off between low operating voltages and high luminous efficiency for the standard coplanar geometry [*Veronis and Inan*, 2002a].
4. The discovery of new cell geometry designs which provide for significantly ($> 15\%$) increased luminous efficiency without a corresponding increase in operating voltages [*Veronis and Inan*, 2002b].

Chapter 2

Physics of collisional, low temperature, partially ionized plasmas

In this chapter, we discuss the basic physics of collisional, low temperature ($T_e \sim$ 1-10 eV, where T_e is the electron temperature), partially ionized ($n_e/N \sim 10^{-6} - 10^{-2}$, where n_e, N are the electron and neutral densities respectively) plasmas. These plasmas have a variety of commercial applications including plasma displays, lamps, gas lasers, plasma switches, and plasma processing of materials (etching and deposition) [e.g., *Lieberman and Lichtenberg*, 1994]. An important feature of these plasmas is the fact that, due to the low degree of ionization, electron collisions with neutrals dominate over collisions with ions or other electrons.

2.1 The distribution function and the Boltzmann equation

In collisional, low temperature, partially ionized plasmas various different particle species exist including charged (electrons, atomic and molecular ions) and neutral (excited atoms and molecules) species. Each species is described by its own distribution function $f(\mathbf{r}, \mathbf{v}, t)$ in six-dimensional phase space, which is defined as follows: the quantity $f d\mathbf{r} d\mathbf{v}$ is the number of particles at time t in a volume element $d\mathbf{r}$ around a point $\mathbf{r}$ with velocities between $\mathbf{v}$ and $\mathbf{v} + \mathbf{dv}$. The distribution function is a general microscopic description of the plasma.

All macroscopic quantities of interest (e.g., flux, momentum, and energy) can be obtained from $f(\mathbf{r},\mathbf{v},t)$ by suitable ensemble averaging. Thus, for the *particle density* $n(\mathbf{r},t)$ we have

$$n(\mathbf{r},t) = \int f(\mathbf{r},\mathbf{v},t)d\mathbf{v}$$

and for the *particle flux* $\mathbf{\Gamma}(\mathbf{r},t)$ we have

$$\mathbf{\Gamma}(\mathbf{r},t) \equiv n(\mathbf{r},t)\mathbf{u}(\mathbf{r},t) = \int \mathbf{v} f(\mathbf{r},\mathbf{v},t)d\mathbf{v}$$

where $\mathbf{u}(\mathbf{r},t)$ is the ensemble averaged particle velocity. In general, the macroscopic (ensemble averaged) value $X(\mathbf{r},t)$ of a physical property $\chi(\mathbf{r},\mathbf{v},t)$ is given by

$$X(\mathbf{r},t) = <\chi(\mathbf{r},\mathbf{v},t)> = \int \chi(\mathbf{r},\mathbf{v},t)f(\mathbf{r},\mathbf{v},t)d\mathbf{v} \Big/ \int f(\mathbf{r},\mathbf{v},t)d\mathbf{v}$$

where the symbol $< >$ denotes averaging over velocity space.

The particle distribution function $f(\mathbf{r},\mathbf{v},t)$ is governed by the Boltzmann equation

$$\frac{\partial f}{\partial t} + \mathbf{v}\cdot\nabla f + \nabla_v \cdot \left(\frac{\mathbf{F}}{m} f\right) = \left(\frac{\partial f}{\partial t}\right)_{\text{collisions}} \tag{2.1}$$

where

$$\nabla \equiv \hat{\mathbf{x}}\frac{\partial}{\partial x} + \hat{\mathbf{y}}\frac{\partial}{\partial y} + \hat{\mathbf{z}}\frac{\partial}{\partial z}$$

$$\nabla_v \equiv \hat{\mathbf{x}}\frac{\partial}{\partial v_x} + \hat{\mathbf{y}}\frac{\partial}{\partial v_y} + \hat{\mathbf{z}}\frac{\partial}{\partial v_z}$$

$\mathbf{F}$ is the external force acting on the particles, m is the particle mass, and $\left(\frac{\partial f}{\partial t}\right)_{\text{collisions}}$ is the time rate of change of the distribution function due to collisions. The Boltzmann equation is a particle conservation equation in phase space [*Raizer*, 1997, p. 77].

In the plasma context, the primary force acting on the particles is the Lorentz force

$$\mathbf{F} = q(\mathbf{E} + \mathbf{v}\times\mathbf{B})$$

where q is the particle charge, and $\mathbf{E}$, $\mathbf{B}$ are the electric and magnetic field respectively. In this work, we do not consider magnetized plasmas (i.e., plasmas under the influence of a static magnetic field) and we deal primarily with electrons having relatively low energies (and hence low values of v) so that the magnetic field component of the force can be neglected and the Boltzmann equation (2.1) may be rewritten as

$$\frac{\partial f}{\partial t} + \mathbf{v} \cdot \nabla f + \frac{q\mathbf{E}}{m} \cdot \nabla_v f = \left(\frac{\partial f}{\partial t} \right)_{\text{collisions}} \tag{2.2}$$

2.2 Collision cross sections

As mentioned above, in weakly ionized plasmas electron-neutral collisions dominate over electron-ion and electron-electron collisions. Thus, in this work we only consider electron-neutral collisions. Such collisions are generally classified as *elastic* or *inelastic* collisions (to be defined later), the latter consisting of a wide variety of physical interaction processes characteristic of the particular neutral constituents. A list of the processes for Ne-Xe mixtures is provided in Chapter 3. The probabilities of collisions are expressed in terms of equivalent cross sections. For a specific collision process, the *collision cross section* σ_c is defined as the number of particles scattered per unit time and per unit incident flux, in all directions from the scattering center [*Bittencourt*, 1995, p. 576].

Collision cross sections are functions of the incident particle energy ε, i.e., $\sigma_c = \sigma_c(\varepsilon)$ and can be either measured experimentally or calculated theoretically. Classical calculation of cross sections requires knowledge of the interaction potential between the two colliding particles. The classical treatment is valid (i.e., a quantum mechanical treatment is not required) if the de Broglie wavelength of each particle is much smaller than the average interparticle separation [*Bittencourt*, 1995, p. 576]. In all plasmas considered in this work, the plasma density is low enough that this condition is easily satisfied. Figure 2.1 shows two selected measured collision cross sections (namely the momentum transfer cross section σ_m and ionization cross section σ_i) for Ne and Xe as a function of electron energy [*Siglo Series*, 1998]. The complete solution of the Boltzmann equation (2.2) requires consideration of all of the non negligible elastic and inelastic processes, as listed in Chapter 3 for the Ne-Xe case.

Consider electrons incident from a given direction on a slab of area A and thickness dx containing neutrals with density N (Figure 2.2) [*Chen*, 1977, p. 136]. The neutrals are imagined to be opaque spheres with cross-sectional area σ_c, so that every time an electron passes within the area blocked by the neutral, an electron-neutral collision event is

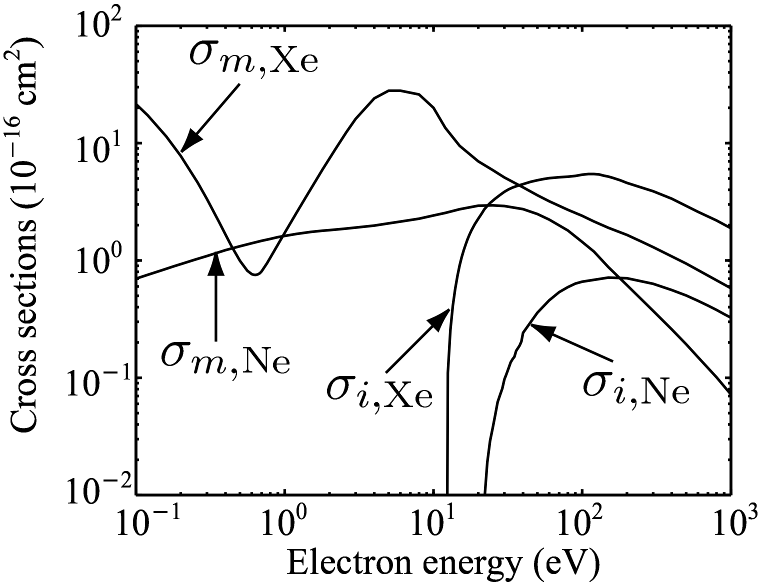

Figure 2.1 Selected collision cross sections for Ne and Xe as a function of electron energy. $\sigma_{m,\mathrm{Ne}}$ and $\sigma_{m,\mathrm{Xe}}$ are the momentum transfer collision cross sections for Ne and Xe respectively. $\sigma_{i,\mathrm{Ne}}$ and $\sigma_{i,\mathrm{Xe}}$ are the electron impact ionization cross sections for Ne and Xe respectively.

considered to occur. The fraction of the area of the slab blocked by neutrals is

$$NAdx\sigma_c/A = N\sigma_c dx$$

so that the change with distance of the incident electron flux Γ is given by

$$d\Gamma = -\Gamma N\sigma_c dx$$

so that we have

$$\Gamma = \Gamma_0 \exp(-N\sigma_c x) = \Gamma_0 \exp(-x/\lambda_c)$$

where λ_c is the *mean free path* for collisions

$$\lambda_c = \frac{1}{N\sigma_c}$$

After traveling a distance λ_c, a particle will have had a probability of making a collision equal to $p_c = 1 - \exp(-1)$. The *mean collision frequency* (i.e., the occurrence rate of collisions) is then given by

$$\nu_c(v) = v/\lambda_c = N\sigma_c v$$

While the above expression is the velocity dependent collision frequency, the macroscopic value of the collision frequency for a specific collision process is found by ensemble averaging over the velocity space

$$< \nu_c >= N < \sigma_c(\varepsilon)v > \tag{2.3}$$

Collisions can be divided into elastic and inelastic. As we will see in Section 2.3.2, the energy loss of electrons in elastic collisions is very small compared with the loss in inelastic collisions. Inelastic collisions include the processes of excitation of atoms and molecules, as well as the creation (loss) of electrons as a result of ionization (recombination) processes [e.g., *Raizer*, 1997, p. 52]. Although inelastic collisions are much less frequent than elastic collisions, they are of special interest in all commercial applications of plasmas. Neutral gases become partially ionized due to ionization processes. The formation of plasmas requires production of positive ions and electrons through ionization which is usually achieved either by applying an electric field or by directly heating the gas. Electrons with energies

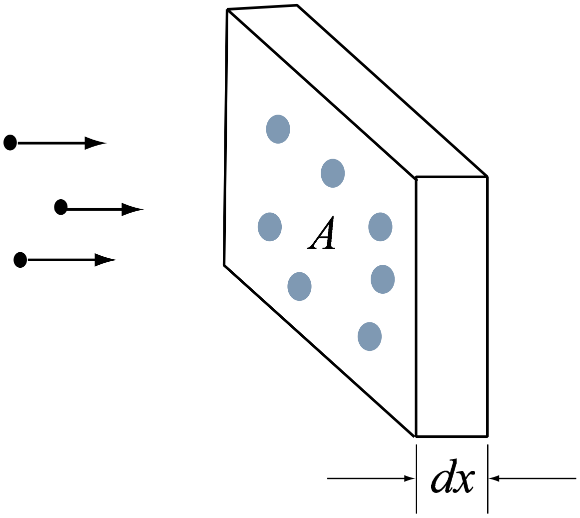

Figure 2.2 Electrons incident on a slab containing neutrals with density N.

higher than the energy level of ionized atomic and molecular states have a finite probability of liberating an electron from an atom or molecule through an ionization collision. Excitation of atoms and molecules is also of special interest in many applications. In the case of gas displays, lamps, and lasers the useful radiation is due to certain excited atomic or molecular states which emit photons. Electrons with energies higher than the energy level of excited atomic and molecular states have a finite probability of exciting an atom or molecule through an excitation collision.

Ionization processes have special importance in the context of the present work, in both the formation and eventual quenching of the discharges that are the ultimate source of luminosity. The highly nonlinear dependence of the ionization cross section on electron energy presents the most important challenge in quantitative modeling of plasma discharges.

2.3 Solution for electrons in constant and uniform electric field

The modeling of the electrodynamics in a plasma display panel cell involves the determination of the particle distribution function by solving (2.2). We first consider the case of electrons in a constant and uniform electric field in a homogeneous medium [*Raizer*, 1997, p.

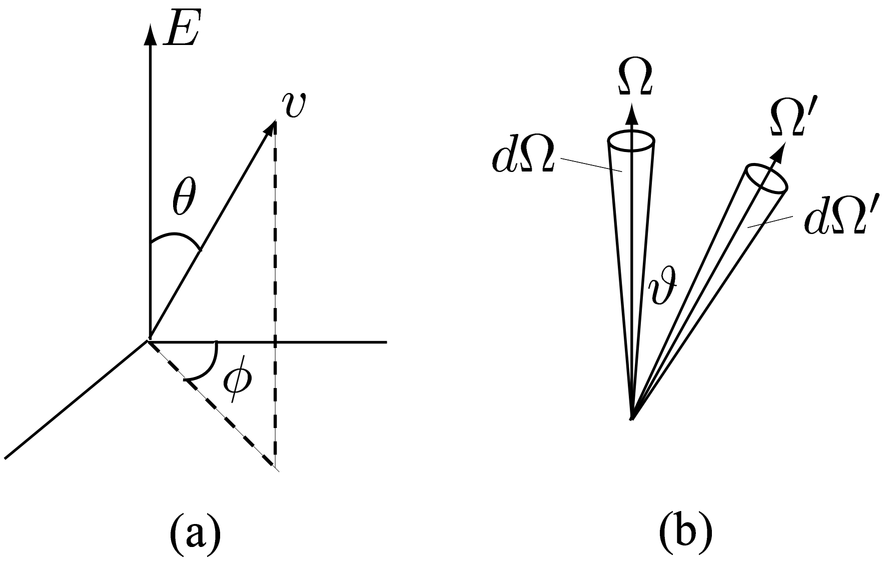

Figure 2.3 (a) Coordinate system for the solution of the Boltzmann equation in a constant and uniform electric field: The electric field $\mathbf{E} = E\hat{\mathbf{z}}$ defines a preferred direction. (b) Direction of the electron velocity before ($\boldsymbol{\Omega}$) and after ($\boldsymbol{\Omega}'$) an elastic collision. The probability of scattering from one direction to another depends only on the scattering angle ϑ between them.

80]. The coordinate system is shown in Fig. 2.3a, with the electric field defining a preferred direction. Due to symmetry the distribution function depends only on the angle θ and not on the angle ϕ, so that we have $f = f(v, \theta, t)$. Since we consider a homogeneous medium, we also have $\nabla f = 0$. In spherical coordinates we then have

$$\nabla_v \equiv \mathbf{e}_v \frac{\partial}{\partial v} + \mathbf{e}_\theta \frac{1}{v}\frac{\partial}{\partial \theta} + \mathbf{e}_\phi \frac{1}{v \sin\theta}\frac{\partial}{\partial \phi}$$

so that the Boltzmann equation (2.2) may be written as

$$\frac{\partial f}{\partial t} - \frac{eE}{m}\left[\cos\theta \frac{\partial f}{\partial v} + \frac{\sin^2\theta}{v} \cdot \frac{\partial f}{\partial(\cos\theta)}\right] = \left(\frac{\partial f}{\partial t}\right)_{\text{collisions}} \tag{2.4}$$

As mentioned above, collisions can be divided into elastic $I(f)$ and inelastic $Q(f)$

$$\left(\frac{\partial f}{\partial t}\right)_{\text{collisions}} = I(f) + Q(f)$$

Although inelastic collisions are normally much less frequent than elastic collisions, they play a dominant role in the dynamics of weakly ionized plasmas due to the highly nonlinear dependence of the cross sections on electron energy.

We neglect for the moment the energy loss in elastic collisions which is on the order of m/M (where M is the mass of neutrals) [*Raizer*, 1997, p. 81] and assume that the neutrals are at rest. This assumption amounts to assuming that the magnitude of their velocity (i.e., v) is conserved. Let $q(v, \mathbf{\Omega}, \mathbf{\Omega}')d\Omega'$ be the probability of a colliding electron (with velocity magnitude v and initial direction $\mathbf{\Omega}$) to change its direction to that within a solid angle $d\Omega'$ around a direction $\mathbf{\Omega}'$. We must then have

$$\int_{\Omega'} q(v, \mathbf{\Omega}, \mathbf{\Omega}')d\Omega' = 1$$

Since the probability of scattering from one direction to another depends only on the scattering angle ϑ between them (Figure 2.3b), we also have

$$q(v, \mathbf{\Omega}, \mathbf{\Omega}') = q(v, \mathbf{\Omega}', \mathbf{\Omega}) = q(v, \vartheta)$$

The elastic collision term can now be expressed as

$$I[f(v, \mathbf{\Omega}, t)] = \nu_c(v) \int_{\Omega'} [f(v, \mathbf{\Omega}', t) - f(v, \mathbf{\Omega}, t)]q(v, \vartheta)d\Omega' \tag{2.5}$$

where $\nu_c(v)f(v, \mathbf{\Omega}', t)q(v, \vartheta)$ represents the number of electrons (per unit time) with velocity magnitude v scattering from direction $\mathbf{\Omega}'$ to direction $\mathbf{\Omega}$, while $\nu_c(v)f(v, \mathbf{\Omega}, t)q(v, \vartheta)$ represents the number of electrons (again per unit time) with velocity magnitude v scattering from direction $\mathbf{\Omega}$ to direction $\mathbf{\Omega}'$. In other words, the quantity $I[f(v, \mathbf{\Omega}, t)]$ represents the net increase per unit time in the number of electrons at the velocity space location $(v, \mathbf{\Omega})$ at time t. The inelastic collision term $Q(f)$ will be specified later, in Section 2.3.3.

2.3.1 Expansion of the distribution function into spherical harmonics

We observe that the collision term involves an integral of the distribution function so that the Boltzmann equation (2.4) is a complicated integro-differential equation. One method of solution of such an equation is the method of moments [*Raizer*, 1997, p. 83]. The distribution function $f(v,\theta,t)$ is first expanded into a series of Legendre polynomials

$$f(v,\theta,t)=\sum_{n=0}^{\infty} f_n(v,t)P_n(\cos\theta)$$

where $P_n(x)$ can be expressed as

$$P_n(x)=\frac{1}{2^n n!}\frac{d^n}{dx^n}(x^2-1)^n$$

Under most practical conditions, the anisotropy in the distribution function due to the electric field is small enough so that only the first two terms have to be retained in the expansion

$$f(v,\theta,t)\simeq f_0(v,t)+f_1(v,t)\cos\theta$$

It can be shown [*Raizer*, 1997, p. 90] that the two-term series expansion is valid for $f_1 \ll f_0$ or equivalently $v_{\text{drift}} \ll v_{\text{thermal}}$ where v_{drift} and v_{thermal} are the electron drift and thermal velocity respectively. These conditions are violated in exceptionally strong fields where the energy gain of electrons from the electric field in one free path becomes comparable to the excitation and ionization potentials of atoms (defined in Section 2.3.3).

For the distribution function of particle energy $n(\varepsilon,t)$, where $\varepsilon=mv^2/2$, defined by the relation

$$n(\varepsilon,t)d\varepsilon \equiv v^2dv\int_{\Omega} f(v,\mathbf{\Omega},t)d\Omega$$

we obtain

$$n(\varepsilon,t)d\varepsilon=4\pi v^2 f_0(v,t)dv \tag{2.6}$$

Due to symmetry, the electron flux points along the field and its magnitude is given by

$$\Gamma=\mathbf{\Gamma}\cdot\hat{\mathbf{z}}=\frac{4\pi}{3}\int_v v^3 f_1 dv$$

Thus, we observe that the electron energy distribution $n(\varepsilon,t)$ is associated with the symmetric part f_0 of f, while the electron flux is associated with f_1.

In order to derive equations for the unknown functions $f_n(v,t)$ based on the method of moments, we multiply the Boltzmann equation (2.4) with a Legendre polynomial and then integrate over the solid angle Ω. In our case of the two-term approximation, it is sufficient to do this twice: first equation (2.4) is simply integrated over the solid angle Ω, noting that $P_0(\cos\theta) = 1$, and then (2.4) is multiplied by $P_1(\cos\theta) = \cos\theta$ and integrated over Ω. Upon further manipulation we find [*Raizer*, 1997, p. 83]

$$\frac{\partial f_0}{\partial t} = \frac{eE}{m}\frac{1}{3v^2}\frac{\partial(v^2 f_1)}{\partial v} + Q(f_0) \tag{2.7}$$

$$\frac{\partial f_1}{\partial t} + \nu_m(v) f_1 = \frac{eE}{m}\frac{\partial f_0}{\partial v} \tag{2.8}$$

We note that in (2.7) Q is a function of only the symmetric part of f, since the effect of inelastic collisions is generally independent of the direction of velocity [*Raizer*, 1997, p. 84]. In equation (2.8), $\nu_m(v)$ is the effective collision frequency for momentum transfer which is found to be [*Raizer*, 1997, p. 84] $\nu_m(v) = \nu_c(v)(1 - \overline{\cos\vartheta})$. Here $\overline{\cos\vartheta}$ is the mean cosine of the scattering angle obtained by averaging $\cos\vartheta$ on the basis of the previously introduced scattering probability $q(v,\vartheta)$. Figure 2.1 shows the momentum transfer collision cross sections σ_m, where $\nu_m(\varepsilon) = N\sigma_m(\varepsilon)v$, for Ne and Xe as a function of electron energy. Momentum transfer collision cross sections can be measured experimentally and are related to the total collision cross section through the relation $\sigma_m = \sigma_c(1 - \overline{\cos\vartheta})$. The physical meaning of the collision frequency for momentum transfer will be further discussed in Section 2.4.3.

We observe that equation (2.7) describes the temporal evolution of f_0 associated with the electron energy distribution $n(\varepsilon, t)$. Since the mean fraction of energy that an electron loses in an elastic collision is on the order of $2m/M$, the electron energy distribution will reach its steady-state value in a time on the order of $\nu_c^{-1}/(2m/M)$. Equation (2.8) implies that f_1 reaches its steady-state value in a time on the order of ν_m^{-1}. In other words, f_1 reaches its steady-state value in a time negligible in comparison with the relaxation time of the electron energy distribution. Thus, equation (2.8) can be approximated by its steady-state solution

$$f_1 = \frac{eE}{m\nu_m(v)}\frac{\partial f_0}{\partial v} \tag{2.9}$$

This approximation is violated in exceptionally strong fields where inelastic collisions are as frequent as elastic collisions.

By substituting (2.9) into (2.7) we obtain

$$\frac{\partial f_0}{\partial t} = \frac{1}{v^2}\frac{\partial}{\partial v}\left[\frac{e^2E^2v^2}{3m^2\nu_m(v)}\frac{\partial f_0}{\partial v}\right] + Q(f_0) \tag{2.10}$$

In order to derive the equation for the electron energy distribution $n(\varepsilon, t)$, we change to a new independent variable $\varepsilon = mv^2/2$ in (2.10) and use (2.6) to obtain

$$\frac{\partial n}{\partial t} + \frac{\partial J}{\partial \varepsilon} = Q, \text{ and } J = -D_\varepsilon\frac{\partial n}{\partial \varepsilon} + nU$$

$$D_\varepsilon = A\varepsilon, \quad U = A/2, \text{ and } A = \frac{2e^2E^2}{3m\nu_m(v)} \tag{2.11}$$

Thus, we observe that the electron energy distribution equation has the form of a continuity equation in the one-dimensional energy space. The flux J in energy space includes a diffusion term characterized by an energy dependent diffusion coefficient D_ε and a drift term with a 'velocity' U. The source term Q is related to inelastic processes, and is discussed below in Section 2.3.3.

2.3.2 Inclusion of elastic collision energy losses

The electron energy loss due to elastic collisions, which was initially neglected in the development of elastic collision term $I[f(v, \mathbf{\Omega}, t)]$ in equation (2.5), can now be easily included by adding a term $J_{\text{el}} = nU_{\text{el}}$ in the flux J [*Raizer*, 1997, p. 88]. Electrons slide downward on the energy axis as a result of elastic collisions. The corresponding 'velocity' of downward motion is

$$U_{\text{el}} = -\Delta\varepsilon_{\text{el}}/\tau_c$$

where $\Delta\varepsilon_{\text{el}}$ is the electron energy loss in one collision and $\tau_c = \nu_c^{-1}$ is the average time between collisions. It will be shown in Section 2.4.3 that

$$\Delta\varepsilon_{\text{el}} = (2m/M)(1 - \overline{\cos\vartheta})\varepsilon \tag{2.12}$$

so that

$$J_{\text{el}} = -(2m/M)\nu_m(v)\varepsilon n, \quad \text{and} \quad J = -D_\varepsilon\frac{\partial n}{\partial \varepsilon} + nU + J_{\text{el}} \tag{2.13}$$

Thus, the elastic energy loss which was initially neglected is now taken into account by adding the flux J_{el} of 'downward' motion of electrons on the energy axis to the flux J.

2.3.3 Inelastic collision term

We are finally ready to complete the specification of the collision term in the Boltzmann equation (2.4) by discussing the source term Q which is related to inelastic processes. As mentioned before, inelastic processes include excitation and ionization of atoms and molecules. Recombination processes have to be taken into account only if the recombination frequency is comparable to the ionization and excitation frequencies. Such situations may occur in plasma regions characterized by high charged species densities and weak electric field. Excited and ionized states of atoms and molecules are characterized by excitation and ionization potentials respectively. Atoms and molecules in their ground state can only be excited (ionized) through inelastic collisions with electrons having an initial energy ε higher than the excitation (ionization) potential ε_{exc} (ε_{ion}). The energy loss of an electron in an inelastic collision is approximately equal to the corresponding excitation (ionization) potential. Based on the above, the source term Q can be easily specified [*Raizer*, 1997, p. 89]. The contribution to Q of a specific excitation process with excitation potential ε_{exc} is

$$Q_{\text{exc}}[n(\varepsilon,t)] = n(\varepsilon+\varepsilon_{\text{exc}},t)\nu_{\text{exc}}(\varepsilon+\varepsilon_{\text{exc}}) - n(\varepsilon,t)\nu_{\text{exc}}(\varepsilon) \tag{2.14}$$

where $\nu_{\text{exc}}(\varepsilon) = N\sigma_{\text{exc}}(\varepsilon)v$ is the excitation frequency of the process, $\sigma_{\text{exc}}(\varepsilon)$ is the corresponding excitation cross section, and $\nu_{\text{exc}}(\varepsilon) = 0$ if $\varepsilon < \varepsilon_{\text{exc}}$. The first term in (2.14) represents increase per unit time of the number of electrons with final energy ε (after experiencing an excitation collision), while the second term represents decrease of the number (per unit time) of electrons with initial energy ε which undergo an excitation collision.

In the case of ionization processes, the generation of secondary electrons must also be considered. An electron with initial energy ε' which experiences an ionizing collision, expends an energy equal to the ionization potential ε_{ion} on liberating an electron from an atom. The remaining energy, $\varepsilon' - \varepsilon_{\text{ion}}$, is divided between the primary and secondary electrons. Let $\Phi(\varepsilon',\varepsilon)d\varepsilon$ be the probability of the energy of the secondary electron to be between ε and $\varepsilon + d\varepsilon$ ($\int_0^{\varepsilon'-\varepsilon_{\text{ion}}} \Phi(\varepsilon',\varepsilon)d\varepsilon = 1$). The contribution to Q of the ionization process is then given by

$$Q_{\text{ion}}[n(\varepsilon,t)] = \int_{\varepsilon+\varepsilon_{\text{ion}}}^{\infty} n(\varepsilon',t)\nu_{\text{ion}}(\varepsilon')[\Phi(\varepsilon',\varepsilon)+\Phi(\varepsilon',\varepsilon'-\varepsilon_{\text{ion}}-\varepsilon)]d\varepsilon' - n(\varepsilon,t)\nu_{\text{ion}}(\varepsilon) \tag{2.15}$$

where $\nu_{\text{ion}}(\varepsilon) = N\sigma_{\text{ion}}(\varepsilon)v$ is the ionization frequency of the process, $\sigma_{\text{ion}}(\varepsilon)$ is the corresponding ionization cross section, and $\nu_{\text{ion}}(\varepsilon) = 0$ if $\varepsilon < \varepsilon_{\text{ion}}$. The first term, represents increase in the number (per unit time) of secondary electrons with energy ε created by ionization collisions, and by primary electrons with final energy ε after experiencing an ionization collision. As in the excitation case, the second term represents the decrease in the number (per unit time) of electrons with initial energy ε which undergo an ionization collision.

As we will see in Chapter 3, several excitation and ionization processes have to be considered for inert gas mixtures typically used in plasma display panels. Table 3.1 gives a list of excitation and ionization processes for the case of a Ne-Xe mixture.

2.3.4 Methods of solution - ELENDIF

In conclusion, under conditions of low degree of ionization and small anisotropy in the distribution function, the Boltzmann equation (2.2) for electrons in a constant electric field reduces to

$$\frac{\partial n}{\partial t} + \frac{\partial J}{\partial \varepsilon} = Q, \quad \text{where} \quad J = -D_{\varepsilon}\frac{\partial n}{\partial \varepsilon} + nU + J_{\text{el}} \tag{2.16}$$

Equations (2.11), (2.13), (2.14), and (2.15) suggest that for the solution of (2.16), knowledge of the momentum transfer cross sections σ_m as well as of the excitation σ_{exc} and ionization σ_{ion} cross sections is required. In addition, $\Phi(\varepsilon',\varepsilon)$ has to be specified in order to correctly include the effect on the distribution function of secondary electrons created through ionization. Equation (2.16) can be solved analytically in only very few cases. It can be shown [*Raizer*, 1997, p. 96] that if inelastic collisions are neglected and the momentum transfer collision frequency $\nu_m(\varepsilon)$ is assumed to be energy independent, the distribution function is Maxwellian. If, instead of $\nu_m(\varepsilon)$, the momentum transfer cross section $\sigma_m(\varepsilon)$ is assumed to be energy independent, the so-called Druyvesteyn's distribution is obtained [*Raizer*, 1997, p. 97]. In virtually all other cases of interest, equation (2.16) can only be solved numerically.

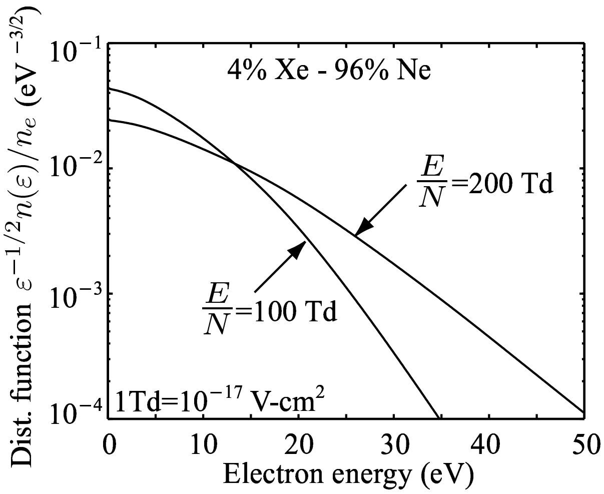

Figure 2.4 Calculated electron energy distribution functions for a 4%Xe-Ne mixture for E/N =100, 200 Td. The vertical axis shows the quantity $\varepsilon^{-1/2}n(\varepsilon)/n_e$, which in the semilogarithmic plot shown here would be a straight line for the case of a Maxwellian distribution function.

ELENDIF [*Morgan and Penetrate*, 1990] is a publicly available computer code which numerically solves the Boltzmann equation (2.16) and calculates the temporal evolution of the electron energy distribution function for a specific gas mixture under the influence of a constant and spatially uniform electric field. The solution is based on the formulation presented in Section 2.3. The cross sections σ_m, σ_{exc}, and σ_{ion} and the function $\Phi(\varepsilon', \varepsilon)$ have to be specified as a function of energy for each gas. In Figure 2.4 we show the calculated electron energy distribution functions for a 4%Xe-Ne mixture for E/N =100, 200 Td, where 1 Townsend (Td) $\equiv 10^{-17}\,\text{V}\cdot\text{cm}^2$. The ratio of the applied electric field to the neutral gas density E/N is usually called the *reduced* electric field. It is easy to note by dividing equation (2.16) by N that $n(\varepsilon, t, E, N) = n(Nt, \varepsilon, E/N)$ and consequently $n(\varepsilon, \infty, E, N) = n(\varepsilon, E/N)$. These relations imply that the steady-state distribution function depends only on the reduced electric field E/N for a specific gas mixture [*Raizer*, 1997, p. 94]. Once the electron energy distribution function is calculated, macroscopic collision frequencies can be found by averaging over the velocity space, as in (2.3). In Figure 2.5 we show calculated macroscopic collision frequencies in a 4%Xe-Ne mixture as a function of the reduced electric field. We note that, since the steady-state distribution function depends only on the reduced

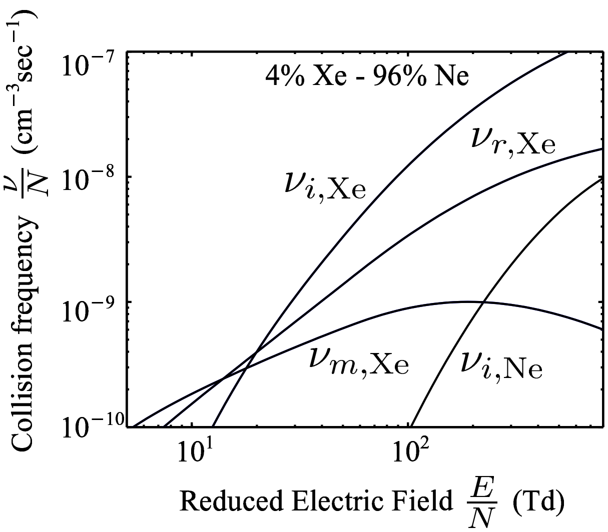

Figure 2.5 Calculated macroscopic collision frequencies for a 4%Xe-Ne mixture. Here $\frac{\nu_{i,\mathrm{Ne}}}{N}$ and $\frac{\nu_{i,\mathrm{Xe}}}{N}$ are the reduced frequencies of electron impact ionization of Ne and Xe atoms respectively, while $\frac{\nu_{m,\mathrm{Xe}}}{N}$ and $\frac{\nu_{r,\mathrm{Xe}}}{N}$ are the reduced frequencies of electron impact excitation of Xe atoms into the metastable and the resonant excited state respectively. The complete list of excited states considered in this dissertation will be given in Chapter 3 (Table 3.1).

electric field E/N, (2.3) implies that

$$\frac{< \nu_c >}{N} =< \sigma_c(\varepsilon) v >= f\left(\frac{E}{N}\right) \tag{2.17}$$

2.4 Solution in time-dependent, non-uniform electric field

In most practical cases of collisional, low temperature, partially ionized plasmas the electric field is neither constant nor uniform. For example, in the case of a plasma display panel cell, the electric field resulting from voltages applied to the sustain electrodes is in fact highly non-uniform. In addition, during the discharge the electric field is further distorted due to space charge effects. The transient nature of the discharge implies that the electric field is also time-dependent. Thus, in most practical cases the Boltzmann equation has to be solved for time-dependent, non-uniform electric fields. Given the baseline fundamental understanding of electron transport based in solutions of the Boltzmann equation in constant and uniform electric fields, two different methodologies have evolved for plasma models.

The so-called kinetic models use temporally and spatially dependent solutions of Boltzmann's equation which produce energy distribution functions either directly or statistically. In the first case [e.g., *Sommerer et al.*, 1991], the solution is based on direct integration of the Boltzmann equation, while in the second case [e.g., *Birdsall*, 1991] (particle-in-cell and Monte Carlo codes) the positions and velocities of a large number of particles are followed and distribution functions are obtained by statistically averaging over the particles. On the other hand, the so-called fluid methods [e.g., *Boeuf*, 1987] are based on solution of the moments of the Boltzmann equation. Kinetic models provide the most detail and are least dependent on a-priori assumptions. However, they are computationally intensive.

In this work, we mainly use the fluid approach. However, the Boltzmann kinetic code ELENDIF [*Morgan and Penetrate*, 1990] is used to determine the electron impact reaction rates and transport coefficients. For each species in the plasma, the spatial and temporal variations of the density are calculated by solving a fluid equation. In other words, the model used in this work is a multifluid kinetic model.

One of the major goals of this work is the investigation of the effect of cell geometry design on the performance of the plasma display panel cell. The effect of cell design parameters, such as electrode shape, can only be studied using two- or three- dimensional models. Purely kinetic models, which solve either directly or statistically the full Boltzmann equation, are extremely expensive computationally, so that extensive two- or three- dimensional studies are practically not feasible with current computers. Fluid models, which only solve moments of the Boltzmann equation, enable extensive studies of geometry effects in two and three dimensions. Although they are less accurate, they have proven to be an important tool in plasma display panel design [e.g., *Yoon et al.*, 2001]. They are usually successful in predicting the effects on the performance of the device of variations in design parameters, such as cell geometry, applied voltage waveforms, and gas mixture. We therefore chose to mainly use the fluid approach which is more appropriate for our purposes.

As mentioned above, a kinetic model (ELENDIF) is used in our multifluid model to determine the electron impact reaction rates and transport coefficients. In this approach, reaction rates and transport coefficients are determined using the local (in space and time) electric field or electron mean energy. The main assumption that enables this approach is that the time required for the establishment of the steady-state distribution function is negligible in comparison with the time scales of variation of the electric field. In addition, as electrons drift in the field, the length required for the establishment of the steady-state distribution is assumed to be negligible in comparison with the length scales of variation of the electric field. The first assumption is well justified, since the energy relaxation times calculated by ELENDIF are much smaller than the time scales of interest. The second assumption is justified in most cases with the exception of the cathode layer region during the discharge [*Raizer*, 1997, p. 92]. Although our approach is therefore expected to be less accurate in the cathode region during the discharge, it is appropriate for our purposes for the reasons detailed in the previous paragragh.

In the remainder of this chapter we will focus on fluid models. Our discussion in this section applies to all particle species which are present in plasmas and is not limited to electrons.

2.4.1 General transport equation

As mentioned above, macroscopic values of physical properties of the plasma, such as momentum and energy, are obtained by averaging over the velocity space of the particle distribution function. In other words, the macroscopic value $X(\mathbf{r},t)$ of a velocity dependent quantity $\chi(\mathbf{v})$ is obtained by multiplying the distribution function $f(\mathbf{r},\mathbf{v},t)$ by $\chi(\mathbf{v})$ and then integrating over the velocity space. In a similar way, the equations governing the temporal and spatial variation of $X(\mathbf{r},t)$ are obtained by multiplying the Boltzmann equation (2.2) by $\chi(\mathbf{v})$ and integrating over velocity space

$$\int \chi \frac{\partial f}{\partial t} d\mathbf{v} + \int \chi \mathbf{v} \cdot \nabla f d\mathbf{v} + \int \chi \frac{q\mathbf{E}}{m} \cdot \nabla_v f d\mathbf{v} = \int \chi \left(\frac{\partial f}{\partial t} \right)_{\text{collisions}} d\mathbf{v} \tag{2.18}$$

It can be shown [*Bittencourt*, 1995, p. 194] that (2.18) reduces to

$$\frac{\partial}{\partial t}(n < \chi >) + \nabla \cdot (n < \chi \mathbf{v} >) - n < \frac{q\mathbf{E}}{m} \cdot \nabla_v \chi >= \int \chi \left(\frac{\partial f}{\partial t} \right)_{\text{collisions}} d\mathbf{v} \tag{2.19}$$

where n is the particle density.

2.4.2 Continuity equation

Since $n(\mathbf{r},t) = \int f(\mathbf{r},\mathbf{v},t) d\mathbf{v}$, the equation governing the spatial and temporal variations of the particle density $n(\mathbf{r},t)$ is obtained for $\chi(\mathbf{v}) = 1$. In other words, the zeroth order moment of the Boltzmann equation is the particle conservation equation, also known as the continuity equation. It is easy to show [*Bittencourt*, 1995, p. 197] that for $\chi(\mathbf{v}) = 1$ (2.19) becomes

$$\frac{\partial n}{\partial t} + \nabla \cdot (n\mathbf{u}) = S \tag{2.20}$$

where $\mathbf{u}$ is the average particle velocity and $S = \int \left(\frac{\partial f}{\partial t}\right)_{\text{collisions}} d\mathbf{v}$ represents the rate of change of the particle density due to collisions. The particle density can only change due to collisions through inelastic processes that result in particle production or loss. In the case of electrons, ionization processes lead to electron production, while recombination and attachment processes lead to electron loss. In general, if we consider the reaction

$$\mathrm{A} + \mathrm{B} \longrightarrow \mathrm{C} + \mathrm{D}$$

then the rate of production of particles C and D and loss of particles A and B is

$$S = k n_{\mathrm{A}} n_{\mathrm{B}}$$

where k is the corresponding reaction rate. Similarly the frequency of loss of particles A (or B) is $\nu = k n_{\mathrm{B}}$ (or $\nu = k n_{\mathrm{A}}$). In the case of heavy particle reactions, reaction rates are usually well approximated by a constant value. On the other hand, as mentioned above, calculation of macroscopic electron impact reaction rates requires averaging over the velocity space using the distribution function. Since the distribution function $f(\mathbf{r}, \mathbf{v}, t)$ is not directly calculated in fluid models, approximate methods have to be employed for the calculation of electron impact reaction rates. The methods most commonly used in fluid models of plasmas will be discussed in Chapter 3 (Section 3.1.1).

2.4.3 Momentum transport equation

The equation governing the spatial and temporal variations of momentum, known as the momentum transport equation or more simply the equation of motion, is obtained for $\chi(\mathbf{v}) = m\mathbf{v}$. Particle velocity $\mathbf{v}$ can be expressed as $\mathbf{v} = \mathbf{u} + \mathbf{w}$, where $\mathbf{u}$ is the average velocity and $\mathbf{w}$ is the random velocity with $<\mathbf{w}>= 0$. It can be shown [*Bittencourt*, 1995, p. 200] that for $\chi(\mathbf{v}) = m\mathbf{v}$ equation (2.19) becomes

$$nm\left[\frac{\partial \mathbf{u}}{\partial t} + (\mathbf{u} \cdot \nabla)\mathbf{u}\right] = nq\mathbf{E} - \nabla \cdot \bar{\mathcal{P}} + \mathbf{A} - m\mathbf{u}S \tag{2.21}$$

where $\bar{\mathcal{P}}$ is the pressure dyad given by $\bar{\mathcal{P}} = nm < \mathbf{w}\,\mathbf{w} >$ and $\mathbf{A} = \int m\mathbf{v} \left(\frac{\partial f}{\partial t}\right)_{\text{collisions}} d\mathbf{v}$ represents the rate of change of momentum density due to collisions.

The pressure dyad is a tensor of rank 2 that is usually denoted as a 3×3 matrix. Nondiagonal terms of the pressure tensor $\bar{\mathcal{P}}$, such as $P_{yx} = nm < w_y w_x >$, are associated with viscosity effects and shear stresses and are relatively unimportant for most plasmas [*Bittencourt*, 1995, p. 202]. Furthermore, the distribution of random velocities is isotropic, so that the diagonal terms of $\bar{\mathcal{P}}$ are all equal to the scalar kinetic pressure defined as $p \equiv \frac{1}{3}nm < w_x^2 + w_y^2 + w_z^2 >$. For isotropic distribution of random velocities $p = nk_BT$, where k_B is the Boltzmann constant and T is the particle temperature defined by the relation $\frac{3}{2}k_BT \equiv \frac{1}{2}m < w^2 >$. (The distribution of random velocities can be anisotropic in magnetized plasmas, which are not considered in this dissertation). Under these conditions, we have

$$\nabla \cdot \bar{\mathcal{P}} = \nabla p = \nabla(nk_BT) \simeq k_BT\nabla n \tag{2.22}$$

where we have neglected the term proportional to ∇T. In collisional plasmas gradients in temperature are usually negligible in comparison with gradients in density. For example, as we shall see in the following chapters, electron density may vary by more than two orders of magnitude over distances of a few microns in typical plasma display panel cells (e.g., Fig. 3.5e), while similar steep variations are never observed in electron temperature due to the high collisional losses at high energies.

As we mentioned above, collisions with neutral species dominate in partially ionized plasmas, so that collisions between charged species (electron-electron, electron-ion, ion-ion) can be neglected. The rate of change of momentum density due to collisions $\mathbf{A}$ is the effective friction force per unit volume acting on particles as a result of collisions with neutrals. The effective friction force for a single particle is

$$\mathbf{F}_{\text{friction}} = m\overline{\Delta\mathbf{v}}/\tau_c$$

where $\overline{\Delta\mathbf{v}}$ is the mean change in velocity due to collisions, and τ_c is the mean time between collisions. If $\mathbf{v}$ is the velocity before the collision, and $\mathbf{v}'$ is the velocity after the collision, we can decompose $\Delta\mathbf{v}$ into components parallel and perpendicular to the initial velocity $\mathbf{v}$ so that

$$\overline{\Delta\mathbf{v}} = \overline{\Delta\mathbf{v}_{||}} + \overline{\Delta\mathbf{v}_{\perp}}$$

Due to symmetry $\overline{\Delta \mathbf{v}_\perp} = 0$. In the case of electrons, we have $m \ll M$ so that the magnitude of the particle velocity v is almost unchanged under elastic collisions so that

$$\overline{\Delta \mathbf{v}} = \overline{\Delta \mathbf{v}_{||}} = \overline{\mathbf{v}'_{||}} - \mathbf{v} = -\mathbf{v}(1 - \overline{\cos\vartheta})$$

where $\overline{\cos\vartheta}$ is the mean cosine of the scattering angle obtained by averaging $\cos\vartheta$ on the basis of the previously introduced scattering probability $q(v, \vartheta)$. Thus, we obtain

$$\mathbf{F}_{\text{friction}} = -m\nu_c \mathbf{v}(1 - \overline{\cos\vartheta}) = -m\nu_m \mathbf{v}, \quad \mathbf{A} = -mn < \nu_m \mathbf{v} > \simeq -mn < \nu_m > \mathbf{u} \tag{2.23}$$

In addition, since the neutrals are assumed to be originally at rest, the energy gain of the neutrals, which is equal to the electron energy loss is given by [*Raizer*, 1997, p. 16]

$$\Delta\varepsilon_{\text{neut}} = \Delta\varepsilon_{\text{el}} = \frac{\overline{(m\Delta v)^2}}{2M} = \frac{m^2}{2M}\overline{(\mathbf{v}' - \mathbf{v})^2} = \frac{m^2}{M}v^2(1 - \overline{\cos\vartheta})$$

and we have thus derived equation (2.12). This elementary analysis of electron collision dynamics further clarifies the physical meaning of the collision frequency for momentum transfer ν_m which was introduced in Section 2.3.1. A similar relation for $\mathbf{A}$ is obtained for other particle species with the difference that the particle mass m has to be substituted by the reduced mass $mM/(m + M)$ [*Raizer*, 1997, p. 24]. In the case of electrons, these two quantities are almost equal.

The last term on the right hand side of equation (2.21) accounts for the additional momentum change due to particle production or loss. Note that $S =< \nu_{\text{inel}} > n$, where ν_{inel} is the net frequency of particle production through inelastic collisions[1] . As mentioned above, inelastic collisions are much less frequent than elastic collisions, so that $<\nu_{\text{inel}}> \ll <\nu_m>$, and the $m\mathbf{u}S$ term can be neglected, since it is too small compared to $\mathbf{A}$.

The second term on the left hand side of (2.21) represents the change in $\mathbf{u}$ which comes about from the fact that a fluid element moves in a region of different $\mathbf{u}$. As mentioned above, our interest in this dissertation is focused on collisional plasmas, in particular the plasma display panel cell, where the collision frequency is relatively high due to the high neutral gas pressure, which is close to the atmospheric pressure. In such plasmas the change in $\mathbf{u}$ due to collisions, represented in equation (2.21) by $\mathbf{A}$, is generally much more significant

---

[1] In the case of electrons, $\nu_{\text{inel}} = \nu_{\text{ion}} - \nu_{\text{rec}}$, where ν_{ion} and ν_{rec} are the total ionization and recombination frequencies respectively.

than the change due to fluid motion in regions of different **u**, so that the second term on the left hand side of (2.21) can be neglected. In other words, the mean free path is much smaller than the length scales of variation of the electric field (and consequently of the mean velocity). In addition, under high gas pressure conditions, the mean time between collisions is much smaller than the time scales of variation of the electric field, so that we can assume that a steady state is established immediately after any variation in the electric field and neglect the first term on the left hand side of (2.21). In other words, the collision frequency is so high that the time required for a fluid element to reach its steady-state **u** is too small compared with the time scales of variation of the electric field and can thus be neglected.

Setting the left hand side of equation (2.21) to zero, neglecting $m\mathbf{u}S$, and using (2.22) and (2.23) we obtain

$$nq\mathbf{E} - k_B T\nabla n - mn < \nu_m > \mathbf{u} = 0 \tag{2.24}$$

or equivalently

$$\mathbf{\Gamma} = n\mathbf{u} = n\frac{q}{m{<}\nu_m{>}}\mathbf{E} - \frac{k_B T}{m{<}\nu_m{>}}\nabla n = \mathrm{sgn}(q)n\mu\mathbf{E} - D\nabla n \tag{2.25}$$

where $\mu \equiv \mid q \mid /(m{<}\nu_m{>})$ is the particle mobility, and $D \equiv k_B T/(m{<}\nu_m{>})$ is the particle diffusion coefficient. Thus, in highly collisional plasmas particle fluxes consist of a drift component due to the electric field and a diffusion component due to density gradients. Equation (2.25) is known as the 'drift-diffusion approximation' to the momentum equation. As mentioned above, the macroscopic value of the collision frequency for momentum transfer in the case of electrons is obtained by averaging over the velocity space of the distribution function. Since the distribution function $f(\mathbf{r}, \mathbf{v}, t)$ is not directly calculated in fluid models, approximate methods have to be employed for the calculation of the electron mobility and the electron diffusion coefficient. These methods are discussed in Chapter 3 (Section 3.1.1). We also note that (2.17) implies that

$$\mu N = f\left(\frac{E}{N}\right) \tag{2.26}$$

2.4.4 Energy transport equation

The equation governing the spatial and temporal variations of energy, known as the energy transport equation or the energy conservation equation, is obtained for $\chi(\mathbf{v}) = mv^2/2$.

We focus our attention on the energy equation for electrons. The temperature of ions and other heavy excited neutral particles is close to the ambient neutral gas temperature. Thus, temperatures of heavy particles are well approximated by a constant value so that their energy equations do not have to be explicitly solved. It can be shown [*Bittencourt*, 1995, p. 204] that for $\chi(\mathbf{v}) = mv^2/2$ equation (2.19) becomes

$$(\frac{\partial}{\partial t} + \mathbf{u} \cdot \nabla)(\frac{3p}{2}) + \frac{3p}{2}\nabla \cdot \mathbf{u} + (\bar{\mathcal{P}} \cdot \nabla) \cdot \mathbf{u} + \nabla \cdot \mathbf{q} = M - \mathbf{u} \cdot \mathbf{A} + \frac{1}{2}mu^2 S \tag{2.27}$$

where $\mathbf{q}$ is the heat flux vector given by $\mathbf{q} = \frac{1}{2}nm < w^2\, \mathbf{w} >$ and $M = \int \frac{1}{2}mv^2 \left(\frac{\partial f}{\partial t}\right)_{\text{collisions}} d\mathbf{v}$ represents the rate of change of energy density due to collisions.

Using the same reasoning as in the momentum equation, the pressure dyad $\bar{\mathcal{P}}$ can be simplified to the scalar kinetic pressure p so that

$$(\bar{\mathcal{P}} \cdot \nabla) \cdot \mathbf{u} = p\nabla \cdot \mathbf{u} \tag{2.28}$$

In addition, since $<\nu_{\text{inel}}> \ll <\nu_m>$, the $\frac{1}{2}mu^2 S$ term is small compared to $\mathbf{u} \cdot \mathbf{A}$ and can be neglected.

As mentioned above, the electron energy loss due to elastic collisions is small compared to inelastic losses and can be neglected to first order[2] . We also note that the energy loss of an electron in an inelastic collision is approximately equal to the corresponding excitation or ionization potential (Section 2.3.3). Thus, the rate of change of electron energy density due to collisions will be

$$M = -n_e \sum_i <\nu_i> \varepsilon_i \tag{2.29}$$

where n_e is the electron density and the summation is over all of the electron impact reactions with occurrence frequency $<\nu_i>$, with ε_i being the corresponding excitation or ionization potential.

We note here that derivation of higher moments of the Boltzmann equation always results in more unknown variables than independent equations [*Bittencourt*, 1995, p. 194]. In other words, any finite set of moment equations is insufficient to constitute a closed system

---

[2] For example the ionization potential of Xenon is $\varepsilon_{\text{ion,Xe}} \simeq$12.1eV. Thus, electrons with energy $\varepsilon >$12.1eV lose ~12.1eV in ionizing collisions with Xe atoms, while they lose only $\Delta\varepsilon_{\text{el}} \sim (2m/M_{\text{Xe}})\varepsilon \sim 8 \times 10^{-6}\varepsilon$ in elastic collisions.

of equations. For example, the unknown mean velocity $\mathbf{u}$ is introduced in deriving the particle conservation equation. In addition, the unknown pressure dyad $\bar{\mathcal{P}}$ (or more simply the unknown scalar pressure $p = nk_BT$ in the case of non viscous plasmas with isotropic velocity distributions) is introduced upon deriving the momentum conservation equation. Similarly, the unknown heat flux vector $\mathbf{q}$ is introduced in deriving the energy equation, and it would be required to solve a higher order moment of the Boltzmann equation in order to determine $\mathbf{q}$. Thus, it is obvious that separate physical assumptions have to be used in order to 'close' a system of finite set of moment equations. As mentioned above, for the case of heavy particle species, the kinetic temperature is approximated by the ambient gas temperature, so that the system of the first two moments of the Boltzmann equation is 'closed'. In the case of electrons, it is obvious that a different approximation has to be used for the heat flux vector $\mathbf{q}$. The approximation most commonly used [*Bittencourt*, 1995, p. 208], which is derived from thermodynamics, is

$$\mathbf{q} = -\lambda \nabla T \tag{2.30}$$

where λ is the thermal conductivity, in units of W/(m · K), related to the diffusion coefficient D through the relation $\lambda = \frac{5}{2}k_BnD$ [*Raizer*, 1997, p. 34]. Using this approximation, the system of the first three moments of the Boltzmann equation (particle, momentum, and energy equation) is 'closed' for electrons.

Neglecting the last term on the right hand side of (2.27), and using equations (2.28), (2.29), and (2.30) as well as the drift-diffusion approximation (2.24) we obtain

$$\frac{\partial n_\varepsilon}{\partial t} + \boldsymbol{\nabla} \cdot \boldsymbol{\Gamma}_\varepsilon = S_\varepsilon \tag{2.31}$$

where $n_\varepsilon = n_e\overline{\varepsilon}$ is the electron energy density, $\overline{\varepsilon} = \frac{3}{2}k_BT$ is the electron mean energy, and

$$\boldsymbol{\Gamma}_\varepsilon = -\frac{5}{3}n_\varepsilon\mu_e\mathbf{E} - \frac{5}{3}D_e\nabla n_\varepsilon$$

$$S_\varepsilon = -e\boldsymbol{\Gamma}_e \cdot \mathbf{E} - n_e\sum_i <\nu_i> \varepsilon_i \tag{2.32}$$

where $\boldsymbol{\Gamma}_\varepsilon$ is the electron energy flux, and S_ε is the electron energy source term. In (2.32) the first term on the right-hand side represents electron heating by the electric field, while the second term accounts for the electron energy losses due to inelastic collisions.

In the remainder of this dissertation macroscopic values of collision frequencies, obtained by averaging over the velocity space, are simply denoted as ν_c (instead of $< \nu_c >$).

Chapter 3

Multifluid model of plasma display panel cell

In this chapter, we describe the multifluid model of the plasma display panel cell used in this work. We also provide a definition of the luminous efficiency and other related quantities. Finally, we briefly describe the one- and two- dimensional discharge dynamics, calculated using the multifluid PDP cell model.

3.1 Description of the model

The dynamics of the PDP plasma are described using a two-dimensional multifluid model. For each species s, the spatial and temporal variations of the density are calculated by solving the continuity equation (2.20)

$$\frac{\partial n_s}{\partial t} + \boldsymbol{\nabla} \cdot \boldsymbol{\Gamma}_s = S_s \tag{3.1}$$

where n_s is the number density, $\boldsymbol{\Gamma}_s$ is the particle flux, and S_s is the source term determined by the particle production and loss processes for species s. We consider electrons, atomic ($\mathrm{Ne}^+, \mathrm{Xe}^+$) and molecular ($\mathrm{Ne}_2^+, \mathrm{Xe}_2^+, \mathrm{NeXe}^+$) ions, and atomic ($\mathrm{Ne}_\mathrm{m}^*$, (sum of the $\mathrm{Ne}^*(^3\mathrm{P}_0)$, $\mathrm{Ne}^*(^3\mathrm{P}_2)$ states), $\mathrm{Xe}^*(^3\mathrm{P}_1)$, $\mathrm{Xe}^*(^3\mathrm{P}_2)$, Xe^{**} (sum of the $6s', 6p, 5d, 7s$ states)) and molecular ($\mathrm{Xe}_2^*(\mathrm{O}_\mathrm{u}^+), \mathrm{Xe}_2^*(^3\Sigma_\mathrm{u}^+), \mathrm{Xe}_2^*(^1\Sigma_\mathrm{u}^+)$) excited species for a Ne-Xe mixture. For each one of the above charged and neutral species the corresponding continuity equation (3.1) is solved. In the case of other inert gas mixtures, such as He-Xe and Ne-Xe-Ar, the corresponding species are considered. Since the gas pressure in typical PDP conditions is high (~500 Torr), we use the drift-diffusion equation (2.25) as an approximation to the momentum equation (2.21), i.e.,

$$\mathbf{\Gamma}_s = \mathrm{sgn}(q_s) n_s \mu_s \mathbf{E} - D_s \nabla n_s \tag{3.2}$$

where q_s is the particle charge, μ_s is the particle mobility, $\mathbf{E}$ is the electric field, and D_s is the particle diffusion coefficient[1].

The electric field within the cell is self-consistently calculated by solving Poisson's equation

$$\nabla \cdot (\varepsilon \mathbf{E}) = \sum_s q_s n_s \tag{3.3}$$

where ε is the dielectric permittivity, equal to ε_0 within the plasma. We note that, given the dimensions of the PDP cell (~150μm), delay times due to electromagnetic propagation ($<$ 1 ps) are negligible compared to the time scales of interest in discharge dynamics ($>$ 1 ns). Thus, a quasi-static solution suffices and there is no need to solve the full set of Maxwell's equations.

3.1.1 Reaction rates and transport coefficients

As mentioned in Sections 2.4.2 and 2.4.3, the distribution function $f(\mathbf{r}, \mathbf{v}, t)$ is not directly calculated in fluid models, and approximate methods have to be employed for the calculation of electron impact reaction rates, and transport coefficients (mobility and diffusion). In our model, electron impact reaction rates and transport coefficients are assumed to be functions of the electron mean energy, which is determined by solving the electron energy equation (2.31).

Several recent PDP models [*Meunier et al.*, 1995; *Punset et al.*, 1998; *Veerasingam et al.*, 1995; *Veerasingam et al.*, 1996] have used the so-called local field approximation to calculate electron impact reaction rates and transport coefficients instead of (2.31). In these models, rates and transport coefficients are presumed to be functions of the local reduced electric field E/N. The local field approximation does not take into account the electron energy redistribution due to thermal conduction and convection as described by the

---

[1] $\mathrm{sgn}(x) = x/|x|$ if $x \neq 0$, 0 otherwise

electron energy flux $\mathbf{\Gamma}_\varepsilon$ in (2.31). In addition, local field approximation models often use an effective electric field, calculated with additional approximations, instead of the exact local electric field [*Punset et al.*, 1998]. Additional approximations are not required when the electron energy equation (2.31) is used. A more detailed comparison of the two methods presented at the end of Section 5.2.2 shows that the local field approximation introduces substantial error in the results when used instead of the electron energy equation. For these reasons it is more appropriate to use the electron energy equation instead of the local field approximation for calculation of electron impact reaction rates and transport coefficients.

As in *Rauf and Kushner* [1999a], constant values at a given pressure are used for the transport coefficients of ions and neutral species, so that their energy equations do not have to be solved.

3.1.2 Kinetic scheme

The electron impact ionization and excitation frequencies as well as the electron mobility are determined using the Boltzmann code ELENDIF [*Morgan and Penetrate*, 1990], which calculates the electron energy distribution function under uniform electric fields (Section 2.3.4). Once the electron mean energy is calculated using (2.31), the solution of the Boltzmann equation obtained by ELENDIF is used to determine ionization and excitation frequencies as well as electron mobility. Electron-atom elastic and inelastic collision cross sections for Ne, He, Xe and Ar are taken from the *SIGLO Series* [1998]. Ion mobilities were obtained from *Ellis et al.* [1976; 1978; 1984] and Blanc's law [*Blanc*, 1908] was used to calculate ion mobilities in gas mixtures. Rate coefficients for Penning ionization, dimer ions formation, charge exchange, recombination, and neutral kinetics reactions as well as excited species lifetimes are taken from *Meunier et al.*, [1995]. Table 3.1 shows the electron impact reaction processes included in the multifluid PDP cell model for a Ne-Xe mixture, while Tables 3.2 and 3.3 show all other processes included as well as their corresponding rate coefficients. As in *Meunier et al.* [1995], a Holstein escape factor g_{H} [*Holstein*, 1947; 1951] is used to describe the lengthening of the apparent lifetime of the resonant state Xe*(^{3}P$_1$) due to radiation trapping, and the resonance radiation (at 147nm) is assumed to be optically thin [*Straaten and Kushner*, 2000]. The escape factor is given by [*Meunier et al.*, 1995]

$$g_{\mathrm{H}} = \frac{1.15}{(\pi \frac{3\pi}{\lambda_0} D)^{1/2}} \tag{3.4}$$

Electron impact reaction process
Neon excitation
$e + \mathrm{Ne} \longrightarrow e + \mathrm{Ne}^*(1\mathrm{s}_5 + 1\mathrm{s}_3)$
$e + \mathrm{Ne} \longrightarrow e + \mathrm{Ne}^*(1\mathrm{s}_4)$
$e + \mathrm{Ne} \longrightarrow e + \mathrm{Ne}^*(1\mathrm{s}_2)$
$e + \mathrm{Ne} \longrightarrow e + \mathrm{Ne}^*(2\mathrm{p})$
$e + \mathrm{Ne} \longrightarrow e + \mathrm{Ne}^*(2\mathrm{s} + 3\mathrm{d})$
$e + \mathrm{Ne} \longrightarrow e + \mathrm{Ne}^*(3\mathrm{p})$
Neon ionization
$e + \mathrm{Ne} \longrightarrow 2e + \mathrm{Ne}^+$
Xenon excitation
$e + \mathrm{Xe} \longrightarrow e + \mathrm{Xe}^*(1\mathrm{s}_5)$
$e + \mathrm{Xe} \longrightarrow e + \mathrm{Xe}^*(1\mathrm{s}_4)$
$e + \mathrm{Xe} \longrightarrow e + \mathrm{Xe}^*(1\mathrm{s}_3 + 1\mathrm{s}_2 + 2\mathrm{p})$
$e + \mathrm{Xe} \longrightarrow e + \mathrm{Xe}^*(2\mathrm{s} + 3\mathrm{d})$
$e + \mathrm{Xe} \longrightarrow e + \mathrm{Xe}^*(2\mathrm{p}')$
$e + \mathrm{Xe} \longrightarrow e + \mathrm{Xe}^*(3 < \mathrm{n} < 9)$
Xenon ionization
$e + \mathrm{Xe} \longrightarrow 2e + \mathrm{Xe}^+$

Table 3.1 Processes included in the multifluid PDP cell model: Electron impact reactions. The rate coefficients for electron impact reactions are calculated by the Boltzmann code [*Morgan and Penetrate*, 1990] (Section 2.3.4). Note that the Ne composite excited state $\mathrm{Ne}^*(1\mathrm{s}_5 + 1\mathrm{s}_3)$ or equivalently $\mathrm{Ne}^*(^3\mathrm{P}_0 + {}^3\mathrm{P}_2)$ is denoted as Ne^*_m in this dissertation. Also the Xe excited states $\mathrm{Xe}^*(1\mathrm{s}_5)$ (metastable state) and $\mathrm{Xe}^*(1\mathrm{s}_4)$ (resonant state) are denoted as $\mathrm{Xe}^*(^3\mathrm{P}_2)$ and $\mathrm{Xe}^*(^3\mathrm{P}_1)$ respectively. Finally, the Xe excited states $\mathrm{Xe}^*(1\mathrm{s}_3 + 1\mathrm{s}_2 + 2\mathrm{p})$, $\mathrm{Xe}^*(2\mathrm{s} + 3\mathrm{d})$, and $\mathrm{Xe}^*(2\mathrm{p}')$ are denoted as a single composite excited state Xe^{**}. In the model, continuity equations are solved for the Ne^*_m, $\mathrm{Xe}^*(^3\mathrm{P}_2)$, $\mathrm{Xe}^*(^3\mathrm{P}_1)$, and Xe^{**} atomic excited states (Section 3.1). Continuity equations are not solved for the rest of the Xe and Ne atomic excited states shown above (e.g., $\mathrm{Xe}^*(3 < \mathrm{n} < 9)$) either because they are not of direct interest or because of lack of data concerning their reaction rates. However, the effect of the corresponding excitation mechanisms shown above on the electron energy distribution function is taken into account.

Process	Rate coefficient
Penning ionization	
$\mathrm{Ne}^*_\mathrm{m} + \mathrm{Xe} \longrightarrow \mathrm{Ne} + \mathrm{Xe}^+ + e$	$7.5 \times 10^{-11}\mathrm{cm}^3\mathrm{s}^{-1}$
$\mathrm{Ne}^*_\mathrm{m} + \mathrm{Xe} \longrightarrow \mathrm{NeXe}^+ + e$	$2.3 \times 10^{-11}\mathrm{cm}^3\mathrm{s}^{-1}$
Dimer ions formation	
$\mathrm{Ne}^+ + 2\mathrm{Ne} \longrightarrow \mathrm{Ne}_2^+ + \mathrm{Ne}$	$4.4 \times 10^{-32}\mathrm{cm}^6\mathrm{s}^{-1}$
$\mathrm{Ne}^+ + \mathrm{Xe} + \mathrm{Ne} \longrightarrow \mathrm{NeXe}^+ + \mathrm{Ne}$	$1.0 \times 10^{-31}\mathrm{cm}^6\mathrm{s}^{-1}$
$\mathrm{Xe}^+ + 2\mathrm{Ne} \longrightarrow \mathrm{NeXe}^+ + \mathrm{Ne}$	$1.0 \times 10^{-31}\mathrm{cm}^6\mathrm{s}^{-1}$
$\mathrm{Xe}^+ + 2\mathrm{Xe} \longrightarrow \mathrm{Xe}_2^+ + \mathrm{Xe}$	$2.5 \times 10^{-31}\mathrm{cm}^6\mathrm{s}^{-1}$
$\mathrm{Xe}^+ + \mathrm{Xe} + \mathrm{Ne} \longrightarrow \mathrm{Xe}_2^+ + \mathrm{Ne}$	$1.5 \times 10^{-31}\mathrm{cm}^6\mathrm{s}^{-1}$
Charge exchange	
$\mathrm{Ne}_2^+ + \mathrm{Xe} + \mathrm{Ne} \longrightarrow \mathrm{Xe}^+ + 3\mathrm{Ne}$	$4.0 \times 10^{-30}\mathrm{cm}^6\mathrm{s}^{-1}$
$\mathrm{NeXe}^+ + \mathrm{Xe} \longrightarrow \mathrm{Xe}_2^+ + \mathrm{Ne}$	$5.0 \times 10^{-12}\mathrm{cm}^3\mathrm{s}^{-1}$
$\mathrm{NeXe}^+ + \mathrm{Xe} \longrightarrow \mathrm{Xe}^+ + \mathrm{Ne} + \mathrm{Xe}$	$5.0 \times 10^{-10}\mathrm{cm}^3\mathrm{s}^{-1}$
Recombination	
$\mathrm{Ne}_2^+ + e \longrightarrow \mathrm{Ne}^* + \mathrm{Ne}$	$3.7 \times 10^{-8}T_e^{-0.43}\mathrm{cm}^3\mathrm{s}^{-1}$
$\mathrm{Xe}_2^+ + e \longrightarrow \mathrm{Xe}^{**} + \mathrm{Xe}$	$2.0 \times 10^{-7}T_e^{-0.5}\mathrm{cm}^3\mathrm{s}^{-1}$
$\mathrm{NeXe}^+ + e \longrightarrow \mathrm{Xe}^{**} + \mathrm{Ne}$	$8.0 \times 10^{-8}T_e^{-0.5}\mathrm{cm}^3\mathrm{s}^{-1}$

Table 3.2 Processes included in the multifluid PDP cell model: Penning ionization, dimer ions formation, charge exchange, recombination. T_e is the self-consistently calculated electron temperature in eV.

where λ_0 =147nm is the emission wavelength and D is the distance between the dielectric layers. Electron and ion diffusion coefficients are determined using the Einstein relation

$$\frac{D_s}{\mu_s} = \frac{k_B T_s}{e}$$

where k_B is the Boltzmann constant, T_s is the particle temperature and e is the elementary charge. The ion temperature is assumed to be equal to the gas temperature.

3.1.3 Photon transport

In order to calculate the visible light output of the PDP cell, we implement a radiation transport model, similar to the one described in *Rauf and Kushner* [1999a]. The source functions for UV photons are computed by the plasma dynamics fluid model, since UV

Process	Rate coefficient
Neutral kinetics	
$\mathrm{Xe^{**} + Ne \longrightarrow Xe^{*}(^3P_2,^3P_1) + Ne}$	$2.0 \times 10^{-12}\mathrm{cm^3s^{-1}}$
$\mathrm{Xe^{**} + Xe \longrightarrow Xe^{*}(^3P_2,^3P_1) + Xe}$	$1.0 \times 10^{-10}\mathrm{cm^3s^{-1}}$
$\mathrm{Xe^{*}(^3P_1) + Ne \longrightarrow Xe^{*}(^3P_2) + Ne}$	$3.11 \times 10^{-14}\mathrm{cm^3s^{-1}}$
$\mathrm{Xe^{*}(^3P_2) + Ne \longrightarrow Xe^{*}(^3P_1) + Ne}$	$1.62 \times 10^{-16}\mathrm{cm^3s^{-1}}$
$\mathrm{Xe^{*}(^3P_1) + Xe \longrightarrow Xe^{*}(^3P_2) + Xe}$	$2.18 \times 10^{-14}\mathrm{cm^3s^{-1}}$
$\mathrm{Xe^{*}(^3P_2) + Xe \longrightarrow Xe^{*}(^3P_1) + Xe}$	$1.26 \times 10^{-16}\mathrm{cm^3s^{-1}}$
$\mathrm{Xe^{*}(^3P_1) + 2Xe \longrightarrow Xe_2^{*}(O_u^+) + Xe}$	$1.55 \times 10^{-31}\mathrm{cm^6s^{-1}}$
$\mathrm{Xe^{*}(^3P_2) + 2Xe \longrightarrow Xe_2^{*}(^3\Sigma_u^+) + Xe}$	$8.53 \times 10^{-32}\mathrm{cm^6s^{-1}}$
$\mathrm{Xe^{*}(^3P_1) + Xe + Ne \longrightarrow Xe_2^{*}(O_u^+) + Ne}$	$4.07 \times 10^{-32}\mathrm{cm^6s^{-1}}$
$\mathrm{Xe^{*}(^3P_2) + Xe + Ne \longrightarrow Xe_2^{*}(^3\Sigma_u^+) + Ne}$	$1.35 \times 10^{-32}\mathrm{cm^6s^{-1}}$
$\mathrm{Xe_2^{*}(O_u^+) + Xe \longrightarrow Xe_2^{*}(^1\Sigma_u^+) + Xe}$	$2.6 \times 10^{-10}\mathrm{cm^3s^{-1}}$
Spontaneous emission	
$\mathrm{Xe^{**} \longrightarrow Xe^{*}(^3P_2,^3P_1)} + h\nu$	$3.0 \times 10^{7}\mathrm{s^{-1}}$
$\mathrm{Xe^{*}(^3P_1) \longrightarrow Xe} + h\nu\ \mathrm{(147nm)}$	$3.33 g_\mathrm{H} \times 10^{8}\mathrm{s^{-1}}$
$\mathrm{Xe_2^{*}(^1\Sigma_u^+) \longrightarrow 2Xe} + h\nu\ \mathrm{(173nm)}$	$1.66 \times 10^{8}\mathrm{s^{-1}}$
$\mathrm{Xe_2^{*}(^3\Sigma_u^+) \longrightarrow 2Xe} + h\nu\ \mathrm{(173nm)}$	$1.0 \times 10^{7}\mathrm{s^{-1}}$
$\mathrm{Xe_2^{*}(O_u^+) \longrightarrow 2Xe} + h\nu\ \mathrm{(150nm)}$	$5.0 \times 10^{8}\mathrm{s^{-1}}$

Table 3.3 Processes included in the multifluid PDP cell model: Neutral kinetics, spontaneous emission. In the second spontaneous emission reaction, g_H is a Holstein escape factor given by equation (3.4).

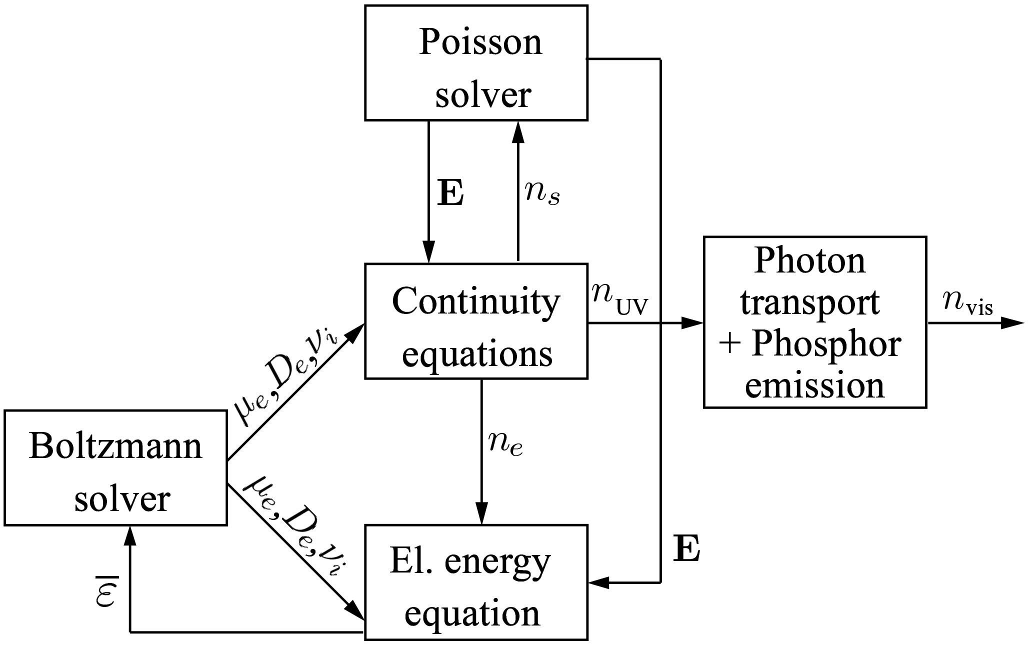

Figure 3.1 Schematic of the PDP cell model. The various modules of the model are shown as well as the interactions between them.

production occurs as a result of the spontaneous emission processes listed in Table 3.3, which are included among the inelastic processes accounted for in our model. We assume that UV photons are emitted isotropically, and calculate their fluxes on the phosphor surface using ray-tracing techniques. A unity UV-to-visible conversion efficiency is assumed for the phosphor. The fluxes of visible photons on the output window are also calculated using ray-tracing techniques, assuming Lambertian emission from the phosphor surface.

A schematic of the model is shown in Figure 3.1. The various modules of the model, which have been described above, are shown as well as the interactions between them. The spatial and temporal variations of particle densities are calculated by solving the continuity equations (3.1). A Poisson solver (3.3) is coupled to the continuity equations, so that the electric field **E** is self-consistently calculated. The solution of continuity equations (3.1) also requires knowledge of the various reaction rates and transport coefficients involved. For heavy charged and neutral particles, reaction rates and transport coefficients are usually approximated by constants at a given pressure (Section 3.1.1). In the case of electrons, once the mean energy is calculated by the electron energy equation (2.31), reaction rates

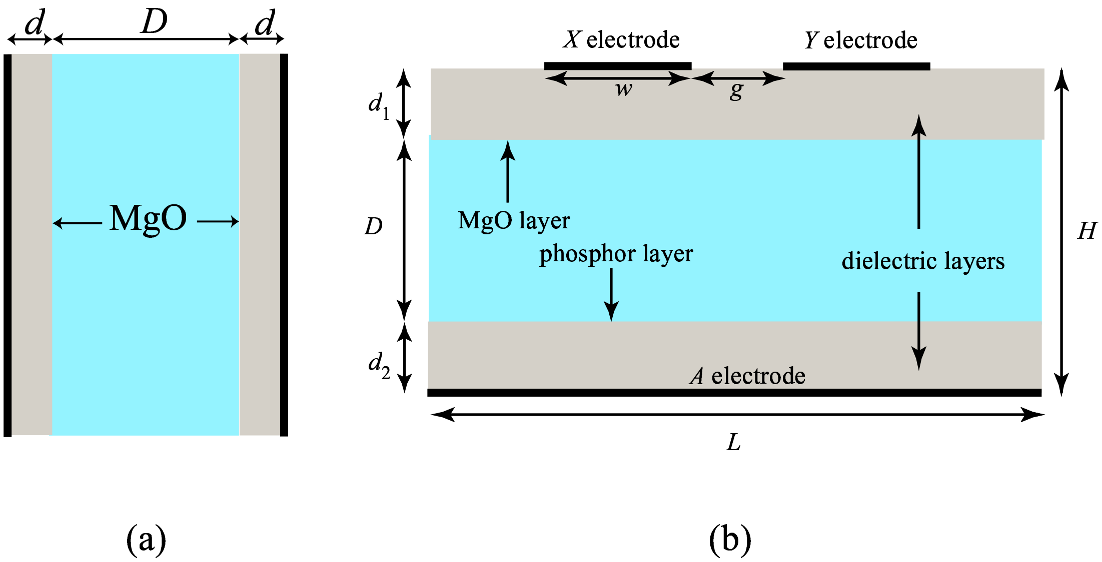

(a) (b)

Figure 3.2 Model geometries of a PDP cell used in the simulations. (a) One-dimensional model (b) Two-dimensional model of a standard coplanar-electrode PDP cell.

and transport coefficients are calculated using the Boltzmann solver ELENDIF [*Morgan and Penetrate*, 1990]. Finally, once the sources of UV emission are calculated, the photon transport and phosphor emission module is used to calculate the visible output.

3.1.4 Cell geometries and boundary conditions

The one-dimensional model geometry of the PDP cell is shown in Figure 3.2a. It consists of two electrodes, separated from the gas by dielectric layers. MgO layers are deposited on the dielectric films. The two-dimensional geometry of the PDP cell is shown in Figure 3.2b. In our studies we focus on the coplanar-electrode PDP design. The cell consists of two sustain electrodes, X and Y, separated from the gas by a dielectric layer. An MgO layer is deposited on the dielectric film. The bottom of the cell consists of the address electrode A separated from the gas by a dielectric layer with a phosphor layer on top. The output window of the device is taken to be the top side of the upper dielectric layer, noting that the sustain electrodes are transparent.

Particle fluxes at the dielectric wall boundaries include a drift term and a thermal flux term [*Meunier et al.*, 1995]

$$\Gamma_s = \alpha_s \mathrm{sgn}(q_s) n_s \mu_s E + \frac{n_s v_{th,s}}{4} \tag{3.5}$$

where α_s is equal to 1 if the particle drift flux is directed towards the wall, and to 0 otherwise. The inclusion of α_s in the first term of (3.5) physically expresses the fact that the electric field cannot pull particles out of the dielectric. The second term in (3.5) is the particle thermal flux in a specific direction in the case of a Maxwellian distribution function [*Bittencourt*, 1995, p. 180]. Although the true particle distribution is not a Maxwellian in an electric field driven plasma, the use of this expression often constitutes a satisfactory first order approximation to the net particle thermal flux onto the dielectric.

When an ion hits a surface, there is a finite probability of emission of an electron from the surface. This phenomenon is taken into account in the model by including a secondary electron flux term in the electron boundary flux

$$\Gamma_e = -\alpha_e n_e \mu_e E + \frac{n_e v_{th,e}}{4} - \sum_i \gamma_i \Gamma_i$$

where γ_i is the secondary electron emission coefficient of ion i on the surface. The probability of secondary electron emission depends on many factors such as incident particle energy, ambient gas pressure, and surface cleanliness. Thus, experimental measurement of γ_i is extremely difficult and usually the result is valid only for the specific experimental surface conditions [*Phelps and Petrovic*, 1999]. In our model, the secondary electron emission coefficients for Ne and Xe ions on MgO are taken to be $\gamma_{\mathrm{Ne}} = 0.5$ and $\gamma_{\mathrm{Xe}} = 0.01$ respectively [*Punset et al.*, 1999], while for the molecular ions we assume $\gamma_{\mathrm{Ne}_2} = 0.5\gamma_{\mathrm{Ne}}$ and $\gamma_{\mathrm{NeXe}} = \gamma_{\mathrm{Xe}_2} = 0.5\gamma_{\mathrm{Xe}}$. Few data exist for secondary electron emission coefficients on phosphors, which are smaller than the corresponding coefficients on the MgO layer [*Elsbergen et al.*, 2000]. The secondary electron emission coefficient for Ne ions on the phosphor layer is taken to be $\gamma_{\mathrm{Ne}} = 0.1$ [*Elsbergen et al.*, 2000]. For all other ions we assume the ratio of the secondary electron emission coefficients on the MgO and phosphor layers to be the same as the corresponding ratio for Ne ions

$$\gamma_{i,\mathrm{phosphor}} = 0.2\gamma_{i,\mathrm{MgO}}$$

It should be noted that in many cases there is a lack of data concerning secondary electron emission coefficients and best guess values are often used in PDP models [*Meunier et al.*, 1995]. The results of the models are thus sensitive to the uncertainties in these coefficients [*Boeuf et al.*, 1997].

Reflective boundary conditions are used at the lateral ends of the cell for the continuity equations, i.e.,

$$\mathbf{\Gamma}_s \cdot \hat{\mathbf{n}} = 0$$

For the electric field we use mixed boundary conditions. The potential is set to the electrode voltages where electrodes are present

$$\phi = V_i$$

where V_i is the voltage applied to electrode i. The perpendicular electric field is set to zero at the lateral ends of the cell and at the portions of the upper boundary which are not covered by metal [*Punset et al.*, 1999], i.e.,

$$\mathbf{E} \cdot \hat{\mathbf{n}} = 0$$

Surface charge density distributions are calculated on the gap-dielectric interface and on the floating electrodes which are included in some of the simulations discussed in Chapter 5.

3.1.5 Numerical method

We use a finite difference method to solve the system of partial differential equations (3.1), (3.3), and (2.31). The Scharfetter-Gummel scheme [*Scharfetter and Gummel*, 1969] is used for the discretization of (3.2), as in *Meunier et al.*, [1995]. The continuity equations (3.1) and the electron energy equation (2.31) are solved implicitly in time to avoid the Courant-Friedrich-Levy constraint on the timestep ($\Delta t < \Delta x / v_{s,\max}$, where Δt is the timestep, Δx is the grid spacing, and $v_{s,\max}$ is the maximum particle velocity). The discretized version of (3.1) and (2.31) used in our model is

$$\frac{n_s^{k+1} - n_s^k}{\Delta t} + \mathbf{\nabla} \cdot {\mathbf{\Gamma}_s}^{k+1} = S_s^k \tag{3.6}$$

In implicit methods, fluxes $\mathbf{\Gamma}_s$ are expressed at $t = (k+1)\Delta t$, as is shown in (3.6) (in explicit methods fluxes are expressed at $t = k\Delta t$).

During the discharge pulse, the presence of high charged species densities severely limits the dielectric relaxation time. As a result, when an explicit method of integration is used for the continuity and field equations, the maximum allowable timestep can be as low as ~0.1 ps ($\Delta t < \varepsilon_0/\sigma_{\max}$, where $\sigma_{\max}$ is the maximum conductivity which can be as high as ~100 S/m). However, several pulses have to be simulated before the PDP device reaches periodic steady state resulting in a required total simulation time of several μs. We therefore chose to integrate the continuity and field equations using the semi-implicit method introduced in *Ventzek et al.*, [1994]:

$$\nabla \cdot (\varepsilon \mathbf{E}^{k+1}) = \sum_s q_s[n_s^k - \Delta t \boldsymbol{\nabla} \cdot \mathbf{\Gamma}_s(\mathbf{E}^{k+1})] \tag{3.7}$$

This method requires the solution of a modified Poisson equation with allowable timesteps orders of magnitude larger than the dielectric relaxation time. As is shown in (3.7), the continuity equations are used to give a prediction of the source term in Poisson's equation at $t = (k+1)\Delta t$.

In addition, when the electron energy equation is used, it becomes limiting for the timestep if an explicit expression for the source term S_ε is used in (2.31). Small timesteps are required to avoid numerical oscillations in the solution of (2.31). We therefore chose to also treat this term implicitly, using the method introduced in *Hagelaar et al.*, [2000]:

$$S_\varepsilon^{k+1} = S_\varepsilon^k + \left(\frac{dS_\varepsilon}{d\bar{\varepsilon}}\right)^k (\bar{\varepsilon}^{k+1} - \bar{\varepsilon}^k) \tag{3.8}$$

As is shown in (3.8), a first-order Taylor approximation is used to give a prediction of the source term at $t = (k+1)\Delta t$.

Sparse linear systems resulting from the discretization of (3.1), (3.3), and (2.31) are solved using an implementation of the biconjugate gradient sparse matrix solution method with incomplete LU factorization for preconditioning [*Seager*, 1988]. In summary, the continuity equations and the electron energy equation are solved implicitly, and semi-implicit methods are used for the integration of the coupled continuity and field equations, and for the source term in the electron energy equation.

As we show in Chapter 5, floating electrodes are included in some of the simulations. For the numerical treatment of floating electrodes we used the capacity matrix method [*Hockney and Eastwood*, 1981, p. 215]. In this method Poisson's equation is solved twice per timestep. First, the total charge, which is assumed to be zero in the case of floating electrodes inserted in the dielectric layer, is distributed uniformly in the surface of the floating electrodes. Poisson's equation is then solved and the distribution of electric potential (not necessarily constant) on the surface of floating electrodes is obtained. It can be shown [*Hockney and Eastwood*, 1981, p. 215] that the surface charge density on the floating electrodes can be calculated using the non-constant potential distribution obtained by Poisson's equation, and the capacity matrix precalculated at the beginning of the simulation, by imposing the condition of charge conservation and of constant potential on each floating electrode. After calculating the surface charge density, Poisson's equation is solved again and a constant potential is obtained on the surface of each floating electrode.

3.2 Definition of efficiency

As mentioned in Chapter 1, one of the most critical issues in ongoing PDP research is the need to improve the luminous efficiency of the display. In this section, we provide a definition of the luminous efficiency and other related quantities.

The dissipated power per unit volume due to electronic current within the PDP cell is

$$p_{\mathrm{e}} = \mathbf{J}_{\mathrm{e}} \cdot \mathbf{E} \tag{3.9}$$

where $\mathbf{J}_{\mathrm{e}}$ is the electronic current. Similarly, the dissipated power per unit volume due to ionic current is

$$p_{\mathrm{i}} = \sum_{i=1}^{N_{\mathrm{ion}}} \mathbf{J}_{\mathrm{ion},i} \cdot \mathbf{E} \tag{3.10}$$

where $\mathbf{J}_{\mathrm{ion},i}$ is the ionic current of ion i.

The luminous efficiency of a PDP cell is a measure of the number of visible photons emitted per unit energy dissipated in the discharge. In color PDPs the purpose of the discharge is to produce UV photons which are then converted to visible light by means of phosphors. UV photons which excite the phosphors and produce visible light are emitted by certain excited states of Xe ($\mathrm{Xe}^*(^3\mathrm{P}_1)$ (resonant state) at 147 nm, $\mathrm{Xe}_2^*(\mathrm{O}_\mathrm{u}^+)$ at 150 nm,

$\mathrm{Xe}_2^*(^3\Sigma_\mathrm{u}^+)$ and $\mathrm{Xe}_2^*(^1\Sigma_\mathrm{u}^+)$ at 173 nm (excimer states)) [*Meunier et al.*, 1995], as listed in Table 3.3. The UV emission energy per unit volume and per unit time is therefore defined as

$$p_{\mathrm{UV}} = \sum_{i=1}^{N_{\mathrm{UV}}} n_i \nu_{\mathrm{UV},i} \varepsilon_{\mathrm{UV},i} \tag{3.11}$$

where n_i is the number density of UV emitting excited state of Xe i, $\nu_{\mathrm{UV},i}$ and $\varepsilon_{\mathrm{UV},i}$ are the corresponding emission frequency and emitted photon energy respectively, and the summation is taken over the UV emitting exciting states $\mathrm{Xe}^*(^3\mathrm{P}_1)$, $\mathrm{Xe}_2^*(\mathrm{O}_\mathrm{u}^+)$, $\mathrm{Xe}_2^*(^3\Sigma_\mathrm{u}^+)$, and $\mathrm{Xe}_2^*(^1\Sigma_\mathrm{u}^+)$. Although the duration of the discharge current pulse is on the order of 10-100 ns, emission of UV photons lasts for about 5 μs due to the lifetimes of some of the excited species [*Meunier et al.*, 1995]. Some excited states of Ne also radiate photons [*Sahni et al.*, 1978] ($\mathrm{Ne}^*(^1\mathrm{P}_1)$ at 736 Å, $\mathrm{Ne}^*(^3\mathrm{P}_1)$ at 743 Å) but these are not in the UV range and the visible orange glow actually deteriorates color purity [*Noborio et al.*, 1994].

Shown in Fig. 3.3 is a block diagram of reaction channels (Tables 3.1, 3.2, 3.3) related to the excited states of Xe which produce UV photons [*Meunier et al.*, 1995]. Atoms in the $\mathrm{Xe}^*(^3\mathrm{P}_1)$ (resonant), $\mathrm{Xe}^*(^3\mathrm{P}_2)$ (metastable), and Xe^{**} (sum of the $6s', 6p, 5d, 7s$ states) excited states are mainly produced due to electron impact excitation reactions[2] (Table 3.1). Since stepwise ionization is negligible and no other important loss mechanisms exist, all the atoms in these excited states lead to the production of UV photons, unless they are lost through diffusion to the walls [*Meunier et al.*, 1995]. As a result, for a given gas mixture, the number of UV photons emitted by excited Xe atoms and molecules in the discharge is directly related to the excitation frequencies of the $\mathrm{Xe}^*(^3\mathrm{P}_1), \mathrm{Xe}^*(^3\mathrm{P}_2)$ and Xe^{**} excited states. The energy spent by electrons on excitation of UV emitting states of Xe per unit volume and per unit time is therefore defined as

$$p_{\mathrm{exc}} = \sum_{i=1}^{N_{\mathrm{exc}}} n_e \nu_{\mathrm{exc},i} \varepsilon_{\mathrm{exc},i} \tag{3.12}$$

where n_e is the electron number density, $\nu_{\mathrm{exc},i}$ is the excitation frequency of excited state of Xe i, $\varepsilon_{\mathrm{exc},i}$ is the corresponding electron loss energy, and the summation is taken over the $\mathrm{Xe}^*(^3\mathrm{P}_1), \mathrm{Xe}^*(^3\mathrm{P}_2)$ and Xe^{**} excited states.

---

[2] They are also produced through electron-ion recombination reactions (Table 3.2).

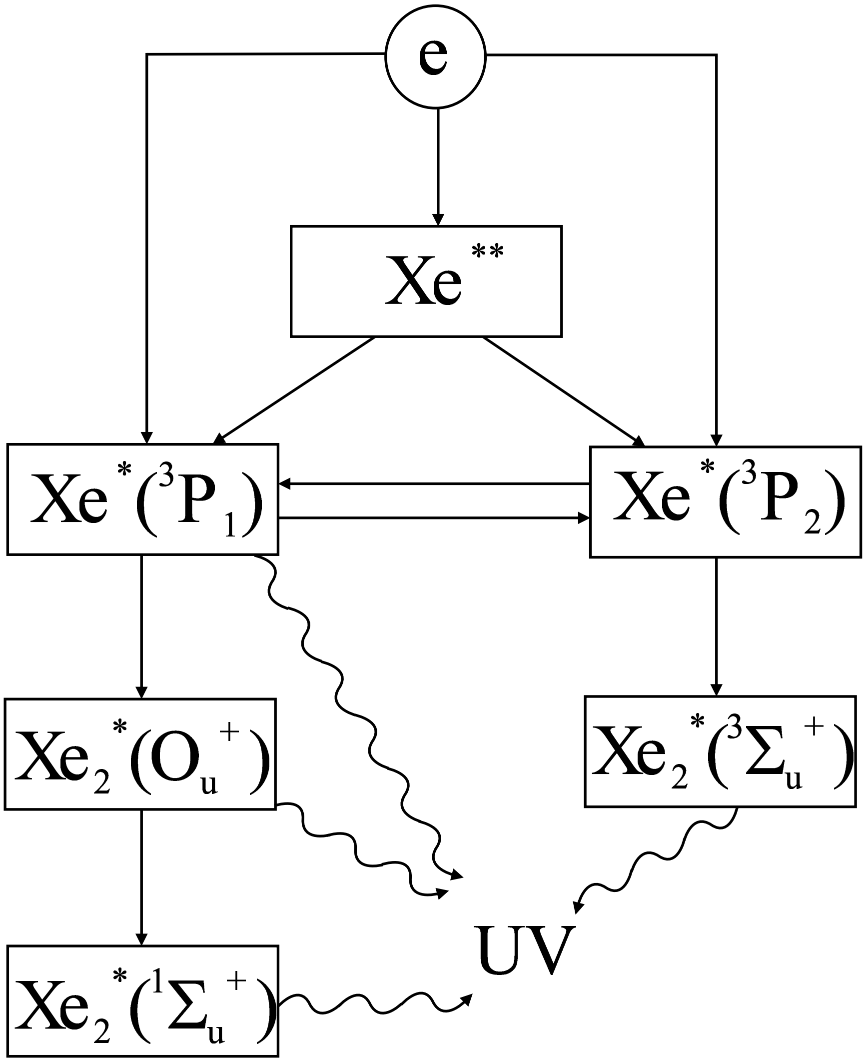

Figure 3.3 Block diagram of reaction channels related to UV emitting excited states of Xe.

We can now define efficiency in both bounded and unbounded systems, based on the definitions of power densities given in (3.9), (3.10), (3.11), (3.12).

3.2.1 Bounded systems

The total energies per sustaining period T in a PDP cell volume V corresponding to the power densities defined in equations (3.9), (3.10), (3.11), (3.12) are obtained by integration over space and time[3]

$$\varepsilon_j = \int_T dt \int_V dv p_j \quad j = \mathrm{e}, \mathrm{i}, \mathrm{exc}, \mathrm{UV} \tag{3.13}$$

The total visible photon energy per sustaining period T which reaches the output window of the PDP cell is given by

$$\varepsilon_{\mathrm{vis}} = \int_T dt \int_{S_{\mathrm{out}}} ds \Gamma_{\mathrm{ph}} \varepsilon_{\mathrm{ph}} \tag{3.14}$$

where Γ_{ph} is the number of visible photons reaching the output window per unit area and per unit time, $\varepsilon_{\mathrm{ph}}$ is the visible photon energy, and S_{out} is the area of the output window. We assume that the visible photon wavelength is 550nm.

We define the luminous efficiency of the cell η as the ratio of total visible photon energy which reaches the output window to the total energy dissipated during a sustaining period T

$$\eta = \varepsilon_{\mathrm{vis}}/(\varepsilon_{\mathrm{e}} + \varepsilon_{\mathrm{i}}) = \frac{\int_T dt \int_{S_{\mathrm{out}}} ds \Gamma_{\mathrm{ph}} \varepsilon_{\mathrm{ph}}}{\int_T dt \int_V dv (\mathbf{J}_{\mathrm{e}} + \sum_{i=1}^{N_{\mathrm{ion}}} \mathbf{J}_{\mathrm{ion},i}) \cdot \mathbf{E}} \tag{3.15}$$

The luminous efficiency defined in (3.15) can also be written as

$$\eta = \eta_1 \eta_2 \eta_3 \eta_4 \tag{3.16}$$

where

$$\eta_1 = \varepsilon_{\mathrm{e}}/(\varepsilon_{\mathrm{e}} + \varepsilon_{\mathrm{i}})$$

$$\eta_2 = \varepsilon_{\mathrm{exc}}/\varepsilon_{\mathrm{e}}$$

---

[3] Note that in one-dimensional (two-dimensional) models spatial integration is over only one (two) spatial dimension(s), so that the calculated quantity is energy per unit area (per unit length) in units of J/m^2 (J/m).

$$\eta_3 = \varepsilon_{\mathrm{UV}}/\varepsilon_{\mathrm{exc}}$$

$$\eta_4 = \varepsilon_{\mathrm{vis}}/\varepsilon_{\mathrm{UV}}$$

Physically, η_1 is the efficiency of the discharge in heating the electrons, η_2 is the efficiency of electrons in producing UV emitting excited states of Xenon through electron impact excitation reactions, and η_3 is the efficiency of emission of UV photons by Xenon excited atoms and molecules. Finally, η_4 is an additional factor in the overall luminous efficiency η, related to the efficiency of transport of UV photons to the phosphor layer and of the visible photons to the output window, and to the UV-to-visible conversion efficiency of the phosphor.

In some cases it is important to explicitly consider the excitation efficiency and UV efficiency of the discharges. For these purposes, we define the excitation efficiency of the discharge η_{exc} as

$$\eta_{\mathrm{exc}} = \eta_1\eta_2 = \frac{\int_T dt \int_V dv \sum_{i=1}^{N_{\mathrm{exc}}} n_e \nu_{\mathrm{exc},i}\varepsilon_{\mathrm{exc},i}}{\int_T dt \int_V dv (\mathbf{J}_{\mathrm{e}} + \sum_{i=1}^{N_{\mathrm{ion}}} \mathbf{J}_{\mathrm{ion},i}) \cdot \mathbf{E}} \tag{3.17}$$

and the UV efficiency of the discharge η_{UV} as

$$\eta_{\mathrm{UV}} = \eta_1\eta_2\eta_3 = \frac{\int_T dt \int_V dv \sum_{i=1}^{N_{\mathrm{UV}}} n_i \nu_{\mathrm{UV},i}\varepsilon_{\mathrm{UV},i}}{\int_T dt \int_V dv (\mathbf{J}_{\mathrm{e}} + \sum_{i=1}^{N_{\mathrm{ion}}} \mathbf{J}_{\mathrm{ion},i}) \cdot \mathbf{E}} \tag{3.18}$$

Physically, η_{exc} is the efficiency of the discharge in producing UV emitting excited states of Xenon through electron impact excitation reactions[4] , and η_{UV} is the efficiency of the discharge in producing UV photons.

Finally, the power in a PDP cell volume V corresponding to the power densities defined in equations (3.9), (3.10), (3.11), (3.12) is obtained by integration over space[5]

$$P_j = \int_V dv p_j \qquad j = \mathrm{e}, \mathrm{i}, \mathrm{exc}, \mathrm{UV} \tag{3.19}$$

---

[4] Note that η_{exc} is slightly smaller than the total efficiency of the discharge in producing UV emitting excited states of Xenon, since a small though non-negligible number of UV emitting excited atoms is produced through electron-ion recombination reactions (Table 3.2).

[5] Note that in one-dimensional (two-dimensional) models integration is over only one (two) spatial dimension(s), so that the calculated quantity is power per unit area (per unit length) in units of $\mathrm{W/m^2}$ (W/m).

3.2.2 Unbounded systems

In the case of unbounded spatially uniform systems, we focus our attention on the efficiency of electrons in producing UV emitting excited states of Xenon through electron impact excitation reactions.

In a spatially uniform system the electronic current $\mathbf{J}_\mathrm{e}$ is given by

$$\mathbf{J}_\mathrm{e} = q_e\mathbf{\Gamma}_e = -q_e n_e \mu_e \mathbf{E} - q_e D_e \nabla n_e = -q_e n_e \mu_e \mathbf{E}$$

so that

$$p_\mathrm{e} = -q_e n_e \mu_e E^2 = e n_e \mu_e E^2 \tag{3.20}$$

Using (3.12) and (3.20), we define the electron excitation efficiency as

$$\eta_{\mathrm{exc},e} = \frac{\sum_{i=1}^{N_\mathrm{exc}} \nu_{\mathrm{exc},i}\varepsilon_{\mathrm{exc},i}}{e\mu_e E^2} \tag{3.21}$$

We can rewrite (3.21) as

$$\eta_{\mathrm{exc},e} = \frac{\displaystyle\sum_{i=1}^{N_\mathrm{exc}} \left(\frac{\nu_{\mathrm{exc},i}}{N}\right)\varepsilon_{\mathrm{exc},i}}{e(\mu_e N)\left(\dfrac{E}{N}\right)^2} \tag{3.22}$$

Equations (2.17), (2.26), and (3.22) imply that the electron excitation efficiency $\eta_{\mathrm{exc},e}$ is a fundamental inherent property of a given gas mixture depending only on its composition and on the reduced electric field E/N.

3.3 One-dimensional discharge dynamics

In this section, we briefly describe the one-dimensional discharge dynamics, calculated using the multifluid PDP cell model. In the results presented in this section, we use the local field approximation instead of the electron energy equation[6] and also use $\gamma_\mathrm{Xe} = 0.05$ instead of

---

[6] As described in Section 3.1.1, the local field approximation introduces error in the results when used instead of the electron energy equation. However, for our purposes here the local field approximation is sufficient to describe the major characteristics of discharge dynamics.

the value reported in Section 3.1.4.

The model cell geometry is as shown in Fig. 3.2a. The gas mixture filling the region between the dielectrics is a 4% Xe-Ne mixture at a pressure of 500 Torr. The length of the dielectric layers is d=25μm and their dielectric constant is ε_r=13, while the gap length is D=100μm.

At the start of the simulation, surface charge is assumed to be deposited on the dielectric walls from the previous sustain pulses (Section 1.2). We note that in the one-dimensional case, the surface charge deposited by the previous sustain pulses can be calculated analytically by considering the fact that the induced electric field exactly cancels the electric field of the applied voltage. As we discuss in Section 3.4, analytical calculation is not possible in the two-dimensional case, so that multiple sustain pulses have to be simulated before the cell reaches its steady state condition. The rise and fall times of the applied sustain pulse are 300ns and its total duration is 5μs. The voltage pulse magnitude V_S is 121 V.

Fig. 3.4a shows the applied voltage and total voltage in the gap during the discharge. Initially the applied voltage adds to the voltage induced by the surface charge (Section 1.2). The total gap voltage is enough to cause breakdown in the gap. Charged particles are produced through ionization and are eventually deposited to the dielectric walls, so that the voltage induced by the surface charge opposes the applied voltage and the total gap voltage decreases to zero. Fig. 3.4b shows the power dissipated by ions, electrons, and power spent on Xe excitation, as defined in (3.19), during the discharge. We observe that the duration of the discharge current pulse is in the order of ~10ns.

Figs. 3.5a, 3.5b show snapshots of the electric field in the gap, while Figs. 3.5c, 3.5d, 3.5e, 3.5f show snapshots of electron and ion densities in the gap during the discharge. At t_1 =350ns the electric field is almost uniform since the ion density in the anode is too small to substantially distort the applied field. Electrons emitted from the cathode via secondary electron emission are multiplied exponentially as they travel through the gap, since the electric field and consequently the ionization frequency are constant. The electron density profile is therefore exponential (Fig. 3.5c). A quasineutral plasma is formed near the anode when the ion-induced distortion results in a field close to zero. At t_2 =410ns the plasma region expands towards the cathode, as electrons reach the zero-field region (Fig. 3.5d). At t_3 =413.6ns the current density is maximum. The sheath length near the cathode region is ~15μm (Fig. 3.5e). The gap voltage is significantly reduced due to charge deposition by the ionic and electronic currents in the cathode and anode regions respectively. After $t = t_3$

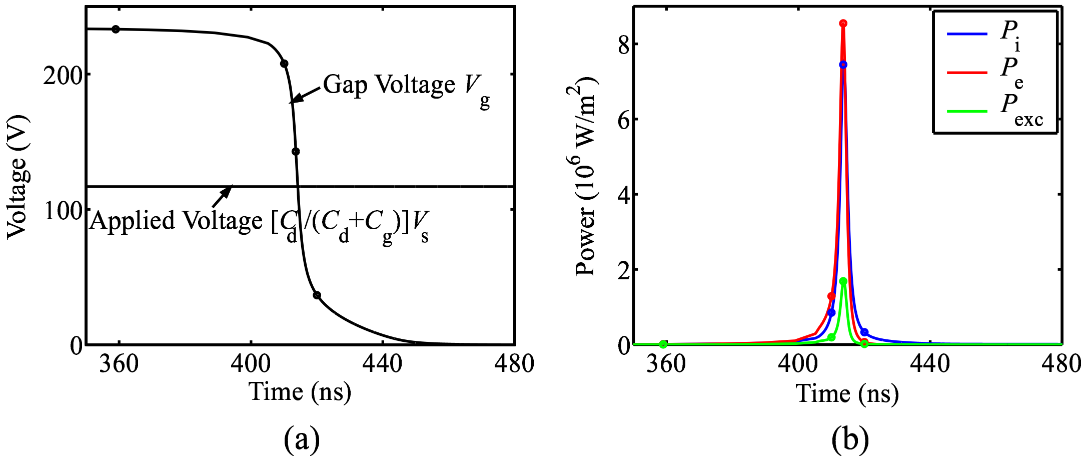

Figure 3.4 (a) Applied voltage and total voltage in the gap during the discharge. The total gap voltage is the superposition of the applied gap voltage and of the equivalent voltage of the deposited surface charge. V_S is the voltage applied to the electrodes of the PDP cell, and C_d, C_g are the equivalent capacitances of the dielectric layers and of the gap respectively. (b) Dissipated ion power P_i, dissipated electron power P_e, and power spent on Xe excitation P_{exc} during the discharge.

the sheath electric field and plasma density decrease. At t_4 =420ns we see that the plasma has decayed through ambipolar diffusion and recombination (Fig. 3.5f).

3.4 Two-dimensional discharge dynamics

In this section, we briefly describe the two-dimensional discharge dynamics, calculated using the multifluid PDP cell model introduced in Section 3.1. The 2-D discharge dynamics are discussed in much greater detail in Chapters 5 and 6.

The model cell geometry is as shown in Fig. 3.2b. The gas mixture filling the region between the dielectrics is a 4% Xe-Ne mixture at a pressure of 500 Torr. The height and width of the cell are H=210μm and L=1260μm respectively. The lengths of the upper and lower dielectric layers are d_1= d_2=30μm, the electrode gap length is g=100μm, the sustain electrode width is w=300μm, and the dielectric constant of the dielectric layers is ε_r=10.

The voltages applied to the three electrodes during the simulation are shown in Figure 3.6. Initially, a data pulse V_D and a base-write pulse $-V_{SW}$ are applied simultaneously to the A and Y electrodes respectively. These are followed by a sequence of alternating sustaining voltage pulses V_S between the two sustain electrodes X and Y. During the

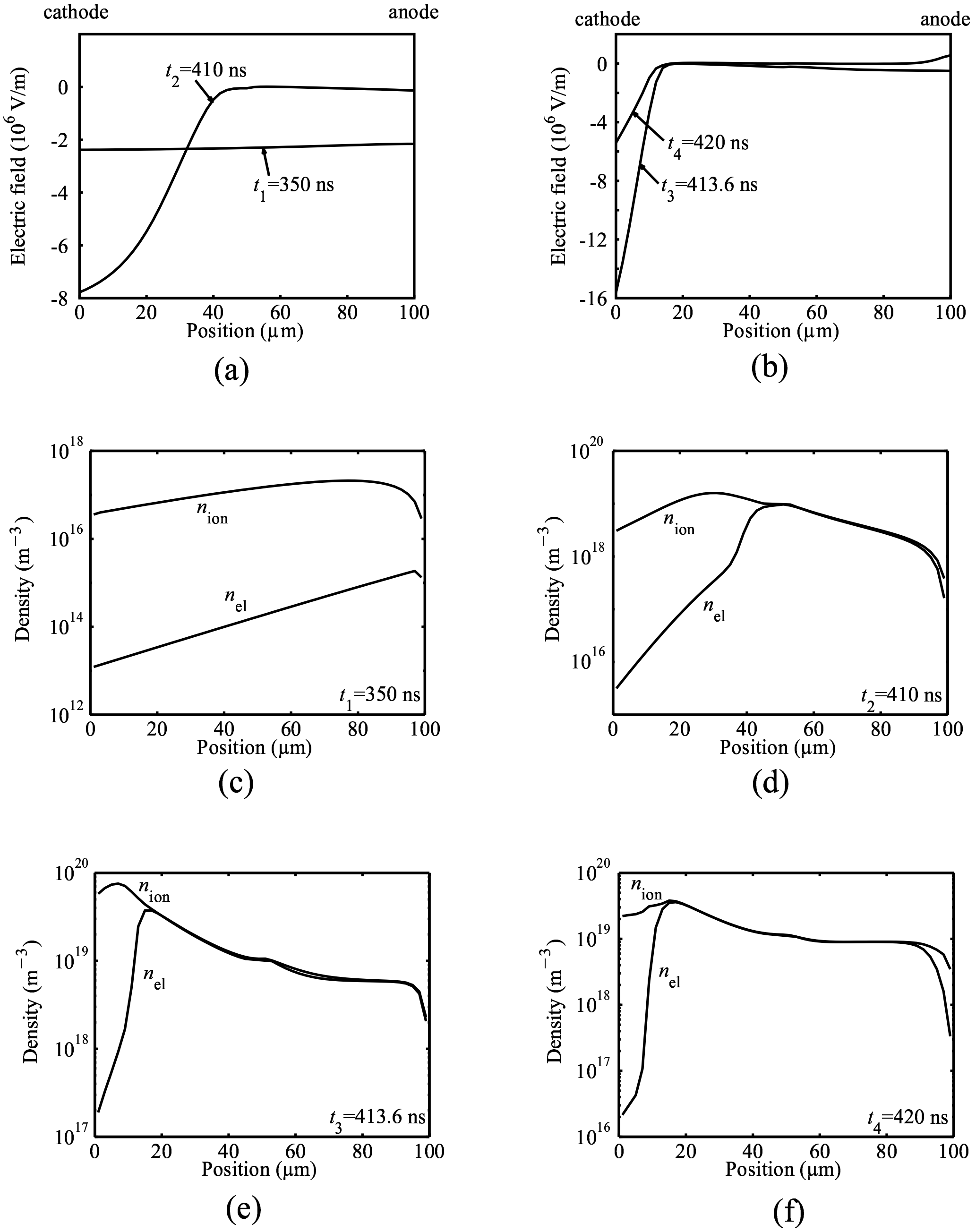

Figure 3.5 (a), (b) Snapshots of the electric field in the gap at various times during the discharge. (c), (d), (e), (f) Snapshots of the electron and ion densities in the gap at various times during the discharge. The times corresponding to the snapshots are also shown in Figures 3.4a and 3.4b for comparison.

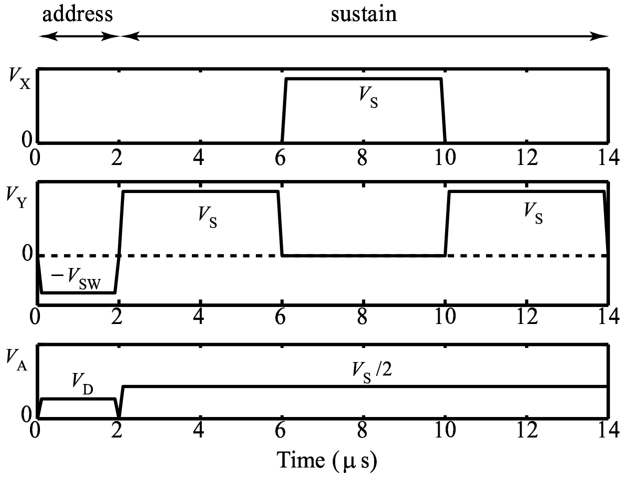

Figure 3.6 Driving scheme used in the 2-D simulations showing the voltage applied to the X, Y, and A electrodes (Fig. 3.2b). Initially, a 2μs address pulse is applied, followed by a sequence of alternating polarity sustain pulses. The sustaining frequency is 125 kHz. The address electrode is biased to a voltage of $V_S/2$ during the sustaining phase.

sustain phase the address electrode A is biased to a voltage of $\frac{V_S}{2}$ to prevent undesired discharges between the address electrode and the sustain electrodes. The frequency of the sustaining waveform is 125 kHz and the rise and fall times of all pulses are 100ns. The duration of the address pulses is 2μs. The magnitudes of the voltage pulses are V_D=80V, V_{SW}=150V, and V_S=265.75V.

Multiple sustain pulses have to be simulated before the cell reaches its steady state condition. In Figure 3.7a, we show the dissipated ion power, dissipated electron power, and power spent on Xe excitation in the PDP cell, as defined in (3.19). Results are shown as a function of time, during the discharge caused by the 5^{th} sustain pulse applied to the Y electrode starting at t=18μs. The duration of the discharge current pulse is ~50ns. We observe that the discharge duration predicted by the 2-D model is much longer than the one predicted by the 1-D model (Section 3.3). In 2-D, there are multiple discharge paths between the anode and the cathode. (During the discharge caused by the 5^{th} pulse, the Y electrode acts as the anode, while the X electrode acts as the cathode.) The discharge initiates at paths with higher electric field. As the discharge is quenched in those paths due to charge deposition on the dielectric walls, the discharge path moves towards the areas below the electrodes that have not yet been covered with charge. The discharge dynamics

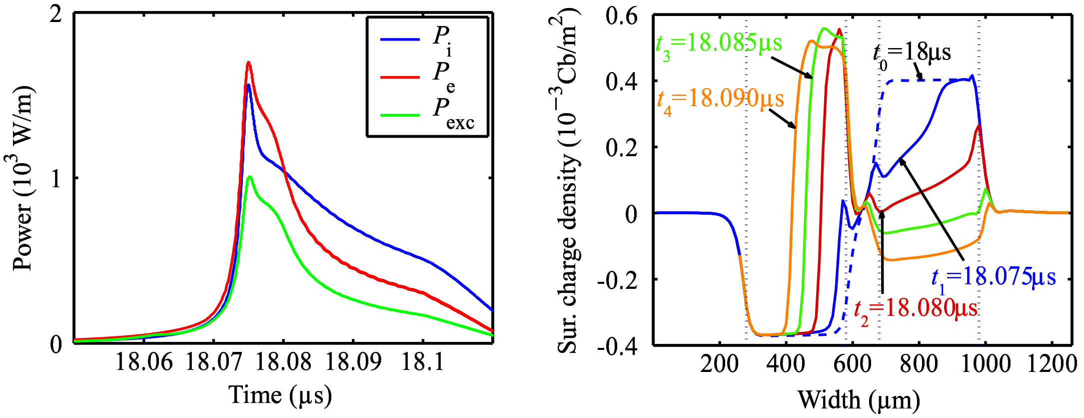

(a) (b)

Figure 3.7 (a) Dissipated ion power P_i, dissipated electron power P_e, and power spent on Xe excitation P_exc during the discharge. (b) Snapshots of the surface charge density on the upper dielectric at various times during the discharge.

can be inferred from the surface charge density on the upper dielectric (Fig. 3.7b): The breakdown initially occurs in the region between the two electrodes where the electric field is higher. As the dielectric is covered with charge, the discharge path moves towards the outer ends of the electrodes.

Chapter 4

Fundamental Properties of Inert Gas Mixtures for Plasma Display Panels

4.1 Introduction

In this chapter, we focus our attention on the effects of gas mixture composition on electron excitation efficiency and on the breakdown voltage.

We study different Xenon gas mixtures and theoretically investigate their efficiency in generating UV photons. In particular, we examine three different cases, i.e. Ne-Xe, He-Xe, and Ne-Xe-Ar. In each case, we investigate the effect of the variation of the percentage of the constituent gases on the electron excitation efficiency of the mixture and on the breakdown voltage. In Section 4.2, we describe our approach, based on the fundamental processes which determine the gas mixture electron excitation efficiency. In Section 4.3, we present the results of our model. In Section 4.4, a one-dimensional self-consistent simulation is used to assess the validity of the conclusions derived from the homogeneous and unbounded kinetic model.

4.2 Formulation

In this chapter, we investigate the effect of the gas mixture on PDP performance from the point of view of the fundamental inherent properties of the constituent gases. For this purpose, we rely on exact numerical solutions of the kinetic Boltzmann equation in an homogeneous, unbounded system while accurately accounting for all the known processes of excitation as well as ionization and other losses. Our chosen measure of comparison of different mixtures is the electron excitation efficiency $\eta_{\mathrm{exc},e}$, as defined in (3.21).

The quantities $\nu_{\mathrm{exc},i}$ and μ_e in (3.21) exhibit highly nonlinear dependence on the electric field E, so that the luminous efficiency can only be evaluated numerically. In this chapter, we determine $\eta_{\mathrm{exc},e}$ by numerically solving the full electron Boltzmann equation to compare the electron excitation efficiency of different gas mixtures by calculating the breakdown voltage and excitation of Xe states which lead to the production of UV photons. It should be noted that $\eta_{\mathrm{exc},e}$, as defined in (3.21), represents the efficiency of the electrons in exciting UV emitting states of Xe. In an actual PDP cell, a fraction of the input energy is dissipated by the ions. However, one-dimensional self-consistent calculations (Section 4.4) indicate that the dependence of the actual discharge excitation efficiency η_{exc}, as defined in (3.17), on gas mixture composition is nevertheless well represented by $\eta_{\mathrm{exc},e}$.

4.2.1 Ne-Xe Mixtures

For our homogeneous and unbounded system, we use a breakdown voltage equivalent to that which would result in a self-sustaining condition in a one-dimensional parallel plate geometry, with plate separation D =100 μm, corresponding to the gap length of a typical PDP cell. This assumption is appropriate since the actual voltage which must be applied to the electrodes of the PDP cell to cause breakdown in the gas is directly proportional to the voltage obtained from the self-sustaining condition. In the Ne-Xe mixture case, this condition can be written [*Penning*, 1957, p. 29; *Boeuf et al.*, 1997]

$$\frac{\alpha_{\mathrm{Ne}}\gamma_{\mathrm{Ne}} + (\alpha_{\mathrm{Xe}} + \alpha_{\mathrm{P}})\gamma_{\mathrm{Xe}}}{\alpha_{\mathrm{Ne}} + \alpha_{\mathrm{Xe}} + \alpha_{\mathrm{P}}} \left[e^{(\alpha_{\mathrm{Ne}}+\alpha_{\mathrm{Xe}}+\alpha_{\mathrm{P}})D} - 1 \right] = 1 \tag{4.1}$$

where $\alpha_{\mathrm{Ne}} = \nu_{\mathrm{Ne}}/v_d$ and $\alpha_{\mathrm{Xe}} = \nu_{\mathrm{Xe}}/v_d$ are the partial first Townsend ionization coefficients for Ne and Xe respectively, ν_{Ne} and ν_{Xe} are the corresponding partial ionization frequencies due to direct ionization of neutral atoms by electrons, v_d is the electron drift velocity, and γ_{Ne} and γ_{Xe} are respectively the secondary electron emission coefficients for Ne and Xe ions impingent on MgO. The quantity α_{P} is the effective partial first Townsend ionization coefficient per electron due to ionization by metastable neon atoms $\mathrm{Ne}^*_{\mathrm{m}}$ (Penning ionization). Neon metastable atoms have a much longer lifetime than the other excited states of Ne and have an energy of $\varepsilon_{\mathrm{m}} \simeq$16.6 eV. Thus, they are capable of ionizing the atoms of other gases having an ionization energy less than 16.6 eV [*Penning*, 1957, p. 15]. The process is highly efficient, if the energy difference between the levels concerned is small [*Meek and Craggs*, 1978, p. 68]. We note that in the determination of the breakdown voltage by (4.1) we do not take into account dimer ions formation, charge exchange, and recombination processes (Table 3.2). These processes are not important in the pre-breakdown phase. The role of recombination in PDP conditions is only important in the afterglow of the discharge [*Punset et al.*, 1999].

The pressure p and the gas temperature T are assumed respectively to be 500 Torr and 300 K, consistent with the usual operation conditions of PDPs [*Meunier et al.*, 1995]. The ionization frequencies ν_{Ne} and ν_{Xe}, as well as the electron drift velocity v_d are calculated as a function of the reduced electric field E/N by numerically solving the full electron Boltzmann equation, using the Boltzmann code ELENDIF [*Morgan and Penetrate*, 1990]. Electron-atom collision cross sections for Ne and Xe are taken from the *Siglo Series* [1998], while $\gamma_{\mathrm{Ne}} = 0.5$ and $\gamma_{\mathrm{Xe}} = 0.05$ [1] are taken from *Meunier et al.* [1995] .

In the Ne-Xe case, the energy of the metastable atom $\mathrm{Ne}^*_{\mathrm{m}}$ is $\varepsilon_{\mathrm{m}} \simeq$16.6 eV, while the ionization energy of Xe is $\varepsilon_{\mathrm{ion,Xe}} \simeq$12.1 eV, so that the energy difference is approximately 4.5 eV. Penning ionization is represented by the reaction (Table 3.2)[*Levin et al.*, 1981]

$$\mathrm{Ne}^*_{\mathrm{m}} + \mathrm{Xe} \longrightarrow \mathrm{Ne} + \mathrm{Xe}^+ + e$$

where Ne and $\mathrm{Ne}^*_{\mathrm{m}}$ represent a ground state and metastable Ne atom respectively, Xe and Xe^+ a ground state Xe atom and its positive ion respectively, and e an electron.

The steady-state Townsend condition [*Sakai et al.*, 1991; *Penning*, 1934] does not hold in typical PDP operation conditions, due to the fact that the discharge is quickly quenched as a result of the accumulation of charge on the dielectric walls covering the electrodes, inducing a potential opposing the applied voltage. The duration of the discharge current pulse is on the order of $t_0 \simeq$10 ns [*Meunier et al.*, 1995]. During this short time, the concentration of Ne metastable atoms $n_{\mathrm{Ne^m}}$ increases due to electron impact excitation and is determined by

$$\frac{dn_{\mathrm{Ne^m}}}{dt} = \nu_{\mathrm{Ne^m}} n_e - \nu^{\mathrm{P}}_{\mathrm{Ne^m}} n_{\mathrm{Ne^m}}$$

---

[1] Note that the numerical value of γ_{Xe} used in this Chapter is different from the one used in all other Chapters of this dissertation (Section 3.1.4).

where $\nu^{\rm P}_{\rm Ne^m}$ is the Penning ionization frequency per Ne metastable atom, and $\nu_{\rm Ne^m}$ is the excitation frequency of the Ne metastable state. The average metastable atom concentration is therefore given as

$$< n_{\rm Ne^m} >= \frac{1}{t_0}\int_0^{t_0} n_{\rm Ne^m}(t)dt = \frac{\nu_{\rm Ne^m}}{\nu^{\rm P}_{\rm Ne^m}}\left(1+\frac{e^{-\nu^{\rm P}_{\rm Ne^m}t_0}-1}{\nu^{\rm P}_{\rm Ne^m}t_0}\right)n_e$$

where n_e is assumed to be constant during the discharge current pulse. Although this approximation is quite rough, it allows us to make a first order estimate of $n_{\rm Ne^m}$, and provides a good estimate of the effect of Penning ionization. Our kinetic model results, as well as the 1D simulations (section 4.4), show that the Penning effect is not very significant in all three cases considered and thus results in relatively small changes in the breakdown field. Thus, possible inaccuracies in the calculation of Penning ionization do not have a significant effect on our results. The effective Penning ionization frequency per electron is then given as

$$[\nu^{\rm P}_{\rm Ne^m}]_{\rm eff} = \frac{\nu^{\rm P}_{\rm Ne^m} < n_{\rm Ne^m} >}{n_e} = \left(1+\frac{e^{-\nu^{\rm P}_{\rm Ne^m}t_0}-1}{\nu^{\rm P}_{\rm Ne^m}t_0}\right)\nu_{\rm Ne^m} \tag{4.2}$$

where we note that $\nu^{\rm P}_{\rm Ne^m}$ is proportional to the concentration of Xe atoms. The corresponding effective partial first Townsend ionization coefficient is $\alpha_{\rm P} = [\nu^{\rm P}_{\rm Ne^m}]_{\rm eff}/v_d$. The frequency $\nu_{\rm Ne^m}$ as a function of the reduced electric field E/N is calculated using the Boltzmann code [*Morgan and Penetrate*, 1990], while $\nu^{\rm P}_{\rm Ne^m}$ (Table 3.2) is taken from *Meunier et al.* [1995]. Stepwise ionization, as well as Penning ionization by collisions between two Xe excited atoms are not taken into account in our modeling, since their effect in typical operational conditions for PDPs is negligible [*Meunier et al.*, 1995].

In the Ne-Xe case, no important excitation mechanisms of UV emitting states of Xenon exist other than electron impact collisions with Xe atoms [*Levin et al.*, 1981]. The excitation frequencies $\nu_{{\rm exc},i}$ in (3.12) are calculated as a function of E/N using the Boltzmann code [*Morgan and Penetrate*, 1990].

4.2.2 He-Xe Mixtures

In the He-Xe case, the self sustaining condition for the calculation of the breakdown field is similar to the corresponding in the Ne-Xe case

$$\frac{\alpha_{\mathrm{He}}\gamma_{\mathrm{He}} + (\alpha_{\mathrm{Xe}} + \alpha_{\mathrm{P}})\gamma_{\mathrm{Xe}}}{\alpha_{\mathrm{He}} + \alpha_{\mathrm{Xe}} + \alpha_{\mathrm{P}}}\left[e^{(\alpha_{\mathrm{He}}+\alpha_{\mathrm{Xe}}+\alpha_{\mathrm{P}})D} - 1\right] = 1 \tag{4.3}$$

where $\alpha_{\mathrm{He}} = \nu_{\mathrm{He}}/v_d$ is the partial first Townsend ionization coefficient for He, ν_{He} is the corresponding partial ionization frequency due to direct ionization of neutral atoms by electrons, γ_{He} is the secondary electron emission coefficient for He ions on MgO, and ν_{He} is calculated as a function of E/N using the Boltzmann code [*Morgan and Penetrate*, 1990]. Cross sections for He are taken from the *Siglo Series* [1998], while $\gamma_{\mathrm{He}} = 0.3$ is taken from *Veerasingam et al.* [1996].

In the case of a He-Xe mixture, Penning ionization is represented by the reaction

$$\mathrm{He}_{\mathrm{m}}^{*} + \mathrm{Xe} \longrightarrow \mathrm{He} + \mathrm{Xe}^{+} + e$$

where He and $\mathrm{He}_{\mathrm{m}}^{*}$ represent a ground state and metastable He atom respectively. In this case, the energy of the He metastable level is $\varepsilon_{\mathrm{m}} \simeq 20$ eV, so the energy difference with the Xe ionization level is approximately 7.9 eV. The effective Penning ionization frequency per electron is calculated in the same way as in the Ne-Xe case and we obtain

$$[\nu_{\mathrm{He^m}}^{\mathrm{P}}]_{\mathrm{eff}} = \left(1 + \frac{e^{-\nu_{\mathrm{He^m}}^{\mathrm{P}} t_0} - 1}{\nu_{\mathrm{He^m}}^{\mathrm{P}} t_0}\right)\nu_{\mathrm{He^m}} \tag{4.4}$$

where $\nu_{\mathrm{He^m}}$ is the excitation frequency of the He metastable state, $\nu_{\mathrm{He^m}}^{\mathrm{P}}$ is the Penning ionization frequency per He metastable atom taken from *Rauf and Kushner* [1999a], and $\nu_{\mathrm{He^m}}$ is calculated as a function of E/N using the Boltzmann code [*Morgan and Penetrate*, 1990]. As in the Ne-Xe case, no important excitation mechanisms of UV emitting states of Xenon exist other than electron impact collisions with Xe atoms [*Rauf and Kushner*, 1999a].

4.2.3 Ne-Xe-Ar Mixtures

In the case of Ne-Xe-Ar mixture the breakdown field is calculated using the condition

$$\left[\frac{\alpha_{\rm Ne}\gamma_{\rm Ne} + (\alpha_{\rm Xe} + \alpha_{\rm P1})\gamma_{\rm Xe} + (\alpha_{\rm Ar} + \alpha_{\rm P2})\gamma_{\rm Ar}}{\alpha_{\rm Ne} + \alpha_{\rm Xe} + \alpha_{\rm P1} + \alpha_{\rm Ar} + \alpha_{\rm P2}}\right]\left[e^{(\alpha_{\rm Ne}+\alpha_{\rm Xe}+\alpha_{\rm P1}+\alpha_{\rm Ar}+\alpha_{\rm P2})D} - 1\right] = 1 \quad (4.5)$$

where $\alpha_{\rm Ar} = \nu_{\rm Ar}/v_d$ is the partial first Townsend ionization coefficient for Ar, $\nu_{\rm Ar}$ is the corresponding partial ionization frequency due to direct ionization of argon atoms by electrons, $\gamma_{\rm Ar}$ is the secondary electron emission coefficient for Ar ions on MgO, and $\nu_{\rm Ar}$ is calculated as a function of E/N using the Boltzmann code [*Morgan and Penetrate*, 1990]. Cross sections for Ar are taken from the *Siglo Series* [1998], while $\gamma_{\rm Ar} = 0.05$ is taken from *Sahni et al.* [1978].

In this case, there are two Penning ionization reactions

$$\text{Ne}^*_{\rm m} + \text{Xe} \longrightarrow \text{Ne} + \text{Xe}^+ + e \quad (4.6)$$

$$\text{Ne}^*_{\rm m} + \text{Ar} \longrightarrow \text{Ne} + \text{Ar}^+ + e \quad (4.7)$$

where Ar and Ar^+ represent a ground state Ar atom and its positive ion respectively. In the second reaction, the argon ionization energy is $\varepsilon_{\rm ion,Ar} \simeq$15.8 eV, so the energy difference with the Ne metastable state is ~0.8 eV. Since the energy difference is small, this process is highly efficient [*Meek and Craggs*, 1978, p. 68]. The effective Penning ionization frequencies per electron are calculated in the same way as in the Ne-Xe and He-Xe cases and we obtain

$$\nu_{\rm P1} = \frac{\nu_{i1}}{\nu_{i1} + \nu_{i2}}\left[1 + \frac{e^{-(\nu_{i1}+\nu_{i2})t_0} - 1}{(\nu_{i1} + \nu_{i2})t_0}\right]\nu_{\rm Ne^m} \quad (4.8)$$

$$\nu_{\rm P2} = \frac{\nu_{i2}}{\nu_{i1} + \nu_{i2}}\left[1 + \frac{e^{-(\nu_{i1}+\nu_{i2})t_0} - 1}{(\nu_{i1} + \nu_{i2})t_0}\right]\nu_{\rm Ne^m} \quad (4.9)$$

where ν_{i1} and ν_{i2} are the Penning ionization frequencies per Ne metastable atom, corresponding to reactions (4.6) and (4.7). Note that ν_{i1} is the same quantity that was denoted as $\nu^{\rm P}_{\rm Ne^m}$ in Section 4.2.1, and is taken from *Meunier et al.* [1995], while ν_{i2} has been taken from *Sahni et al.* [1978]. The excited states of Xe which emit UV photons are mainly produced by electron impact reactions with Xe atoms, as in the case of Ne-Xe and He-Xe mixtures. However, in this case, a particular excitation mechanism due to collisions of Ar excited atoms with Xe atoms does exist :

$$\mathrm{Ar}^* + \mathrm{Xe} \longrightarrow \mathrm{Ar} + \mathrm{Xe}^* \tag{4.10}$$

where Ar and Ar* represent a ground state and excited Ar atom respectively, and Xe and Xe* a ground state and excited Xe atom respectively [*Kannari et al.*, 1983]. In the Ne-Xe-Ar mixtures under consideration, this reaction is the dominant loss mechanism of Ar excited atoms. Thus, in the Ne-Xe-Ar case, the summation in (3.12) includes Argon excitation, since it eventually results in Xenon excitation through the reaction path (4.10).

4.3 Results

Our stated goal in this chapter is to compare the different gas mixtures in terms of their breakdown voltage and electron excitation efficiency, as defined in (3.21). However, the electric field $\mathbf{E}$ in the PDP cell during the discharge is spatially non-uniform due to space charges, with its spatial distribution being time dependent. In addition, Xe excitation, which has a highly nonlinear dependence on the electric field, occurs both in the high and low field regions. Accordingly, we evaluate the electron excitation efficiency $\eta_{\mathrm{exc},e}$ for $E = 0.2E_k, E_k, 5E_k$, where E_k is the breakdown field for our conditions ($p = 500$ Torr, $T = 300$ K, $D = 100\ \mu$m) calculated using (4.1), (4.3), (4.5) in the case of Ne-Xe, He-Xe, Ne-Xe-Ar mixtures respectively. This range of electric field values, defined with respect to E_k, encompasses electric fields typically encountered in PDP cells, according to previous 1D or 2D models [*Meunier et al.*, 1995].

In the following subsections, we separately examine each of the three gas mixtures.

4.3.1 Ne-Xe Mixtures

Fig. 4.1a shows the variation of the breakdown gap voltage $V_g \equiv E_k D$ as a function of the Xe concentration N_{Xe} in the mixture, calculated using (4.1). We observe that for $N_{\mathrm{Xe}} \geq 0.02N$, E_k is an increasing function of N_{Xe}. Penning effect is found to not be significant for this mixture, since $[\nu^{\mathrm{P}}_{\mathrm{Ne^m}}]_{\mathrm{eff}}$ is found to be less than ~12% of the total ionization

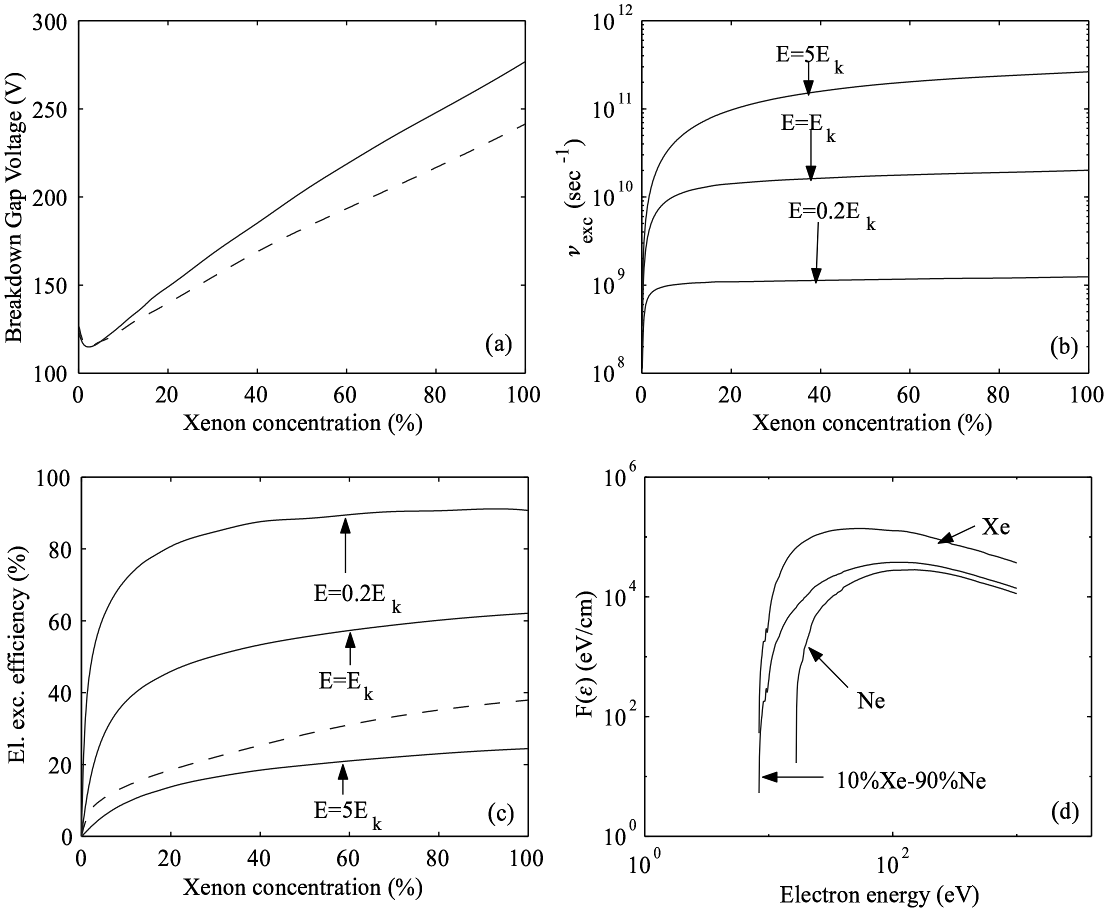

Figure 4.1 (a) Breakdown gap voltage as a function of Xe concentration N_{Xe} in Ne-Xe mixtures, calculated using (4.1). The dashed line shows the mid-margin gap voltage, calculated using the 1D model. (b) Excitation frequency ν_{exc} as a function of N_{Xe}. (c) Electron excitation efficiency (%) $\eta_{\mathrm{exc},e}$ as a function of N_{Xe}. The dashed line shows the excitation efficiency of the discharge, calculated using the 1D model. (d) The loss function as a function of electron energy in a pure Ne gas, a pure Xe gas and a 10% Xe - 90% Ne gas mixture.

frequency $\nu_{\rm ion}^{\rm tot}$ for the full range of parameter values. Fig. 4.1b shows the excitation frequency $\nu_{\rm exc}$ [2] as a function of $N_{\rm Xe}$ for $E = 0.2E_k, E_k, 5E_k$, keeping in mind that E_k is also a function of the concentrations of the constituent gases. We observe that for small values of $N_{\rm Xe}$, $\nu_{\rm exc}$ increases dramatically with small percentage increases in Xe concentration, while $\nu_{\rm exc}$ increases at a much smaller rate for high Xe concentrations. We also observe that $\nu_{\rm exc}(0.2E_k) \ll \nu_{\rm exc}(E_k) \ll \nu_{\rm exc}(5E_k)$ independent of $N_{\rm Xe}$. Fig. 4.1c shows the electron excitation efficiency $\eta_{{\rm exc},e}$ as a function of $N_{\rm Xe}$, calculated by (3.21). We observe that the discharge is more efficient at low electric field values, although the number of Xe atoms excited is higher at high electric field values (Fig. 4.1b). Electron excitation efficiency is also an increasing function of $N_{\rm Xe}$.

The numerical results given in Figure 4.1 can be interpreted in terms of the inherent kinetic behavior of Ne and Xe under applied electric fields. Fig. 4.1d shows the dynamic friction force of electrons, also known as the *electron energy loss function*, as a function of electron energy in a pure Ne gas, a pure Xe gas and a 10% Xe - 90% Ne gas mixture. In any given mixture, the loss function is defined as

$$F(\varepsilon) = \sum_i N_i \sigma_i(\varepsilon) \delta\varepsilon_i \tag{4.11}$$

where the summation is over all the collision cross sections of inelastic processes σ_i with corresponding energy loss $\delta\varepsilon_i$ [3], and N_i is the number density of the corresponding target atoms.

The dynamic friction force has units eV/m (energy loss per unit length), and can be thought of as an effective force acting on electrons against the accelerating action of the electric field. When electrons reach high energies ($\varepsilon >$10eV), inelastic collisions are more frequent than elastic ones, and the electrons are mostly scattered forward [*Raizer*, 1997, p. 102]. Under the assumption of forward scattering, the effective force acting on electrons due to inelastic process i with energy loss $\delta\varepsilon_i$ and collision mean free path λ_i will be (Section 2.2)

$$F_i(\varepsilon) = \frac{\delta\varepsilon_i}{\lambda_i(\varepsilon)} = N_i \sigma_i(\varepsilon) \delta\varepsilon_i$$

The total friction force $F(\varepsilon)$ is obtained by summing over all the inelastic processes. Under

---

[2] $\nu_{\rm exc} = \sum_{i=1}^{N_{\rm exc}} \nu_{{\rm exc},i}$, where the summation is taken over the ${\rm Xe}^*(^3{\rm P}_1), {\rm Xe}^*(^3{\rm P}_2)$ and ${\rm Xe}^{**}$ excited states.

[3] As mentioned in Section 2.3.3 the energy loss of electrons $\delta\varepsilon_i$ in excitation (ionization) collisions is equal to the corresponding excitation (ionization) potential $\varepsilon_{\rm exc}$ ($\varepsilon_{\rm ion}$).

these assumptions, the resulting momentum equation for an electron is

$$m_e \frac{dv_e}{dt} = -eE - F(\varepsilon) \tag{4.12}$$

Equation (4.12) illustrates that the loss function $F(\varepsilon)$ can be directly compared to the applied electric field E to provide intuitively simple insight into the expected dynamics of electrons at different energies.

The breakdown field is much higher for Xe as compared to Ne as is evident from Fig. 4.1a. That this is the case can be understood in terms of the corresponding loss functions. The ionization energy of Xe is $\varepsilon_{\text{ion,Xe}} \simeq$12.1 eV, while $\varepsilon_{\text{ion,Ne}} \simeq$21.6 eV. However, the dynamic friction for Xe is much higher than that for Ne, due to the fact that the excitation and ionization cross sections of Xe are almost one order of magnitude higher [*Siglo Series*, 1998] than those of Ne. Thus, if the same electric field is applied at a pure Xe versus a pure Ne gas, the number of electrons above the corresponding ionization threshold is much higher in Ne, accounting for the fact that E_k is an increasing function of N_{Xe} (Figure 4.1a) in Ne-Xe mixtures. This is also due to the fact that the secondary electron emission coefficient γ_{Ne} for neon ions on MgO is an order of magnitude higher than the corresponding coefficient γ_{Xe} for xenon ions. The loss function (or dynamic friction) also determines the electron energy distribution function that is attained in a gas for a given applied electric field. For small values of N_{Xe}, the loss function (and thus the electron energy distribution) does not vary significantly with increasing N_{Xe}, so that the dynamic friction at the excitation energy of Xe is relatively low, and many electrons have energies above this threshold, leading to the dramatic increase of Xe excitation frequency ν_{exc}. The corresponding partial ionization frequency of Xe (i.e., ν_{Xe}) increases dramatically for the same reason, while the corresponding partial ionization frequency ν_{Ne} of Ne slightly decreases, since the electron distribution function is only slightly perturbed by the addition of a small amount of Xe in Ne. Thus, E_k is a decreasing function of N_{Xe} for small N_{Xe} ($N_{\text{Xe}} \leq 0.02N$).

The results presented in Fig. 4.1a and 4.1c should allow quantitative evaluation of the effects of Xe percentage in Ne-Xe mixtures in practice. In this context, it is desirable to have high electron excitation efficiency and low breakdown field (i.e., lower voltage operation). From Fig. 4.1c, we note that while $\eta_{\text{exc},e}$ increases rapidly with Xe percentage for low values of N_{Xe}, the rate of increase in $\eta_{\text{exc},e}$ decreases with increasing N_{Xe}. Specifically, we note that while $\eta_{\text{exc},e} \simeq$70% for $N_{\text{Xe}} \simeq 0.1N$, it is only ~10% higher for $N_{\text{Xe}} \simeq 0.2N$, while the breakdown voltage is ~25% higher. In Sec. 4.4 we show that the dependence of the actual discharge excitation efficiency η_{exc} on N_{Xe} is very similar.

4.3.2 He-Xe Mixtures

Fig. 4.2a shows the breakdown gap voltage $V_g \equiv E_k D$ as a function of Xe concentration N_{Xe} in a He-Xe mixture, calculated using (4.3). The functional dependence of E_k on N_{Xe} is similar to the Ne-Xe case. However, E_k is slightly higher in a He-Xe mixture compared with a Ne-Xe mixture with the same Xe concentration. The contribution of the Penning effect is also not significant for this case, since $[\nu^{\mathrm{P}}_{\mathrm{He^m}}]_{\mathrm{eff}}$ is found to be less than ~7% of $\nu^{\mathrm{tot}}_{\mathrm{ion}}$ for the full range of parameter values considered. Fig. 4.2b shows the excitation frequency ν_{exc} [4] of Xe as a function of N_{Xe} for $E = 0.2E_k, E_k, 5E_k$. The results are similar to the Ne-Xe case, although ν_{exc} values are smaller. Due to the higher breakdown field and the smaller Xe excitation frequency, the electron excitation efficiency is smaller, as shown in Fig. 4.2c. However, it should be noted that He-Xe mixtures achieve better color purity, since the discharge does not produce visible light as in the Ne-Xe case [*Noborio et al.*, 1994].

In Fig. 4.2d, we plot the loss function as a function of electron energy in a pure He gas, a pure Xe gas and a 10% Xe - 90% He gas mixture. For comparison we also plot the loss function for pure Ne. We observe that the loss function for pure Ne has slightly higher values than that for pure He. Based on the discussion in section 4.3.1, we would expect slightly lower ionization and excitation frequencies in Ne-Xe mixtures in comparison with He-Xe mixtures. However, the ionization and excitation frequencies in He-Xe mixtures are actually lower compared with Ne-Xe mixtures with the same Xe concentration, resulting in higher breakdown field and lower electron excitation efficiency. It was found that this result is mainly due to the higher electron momentum transfer cross section of He as compared to that of Ne [*Siglo Series*, 1998]. Since the loss functions are almost equal, this effect dominates, resulting in lower ionization and excitation coefficients in He-Xe mixtures in comparison with Ne-Xe mixtures with the same Xe concentration [*Rauf and Kushner*, 1999b]. The higher breakdown field in He-Xe mixtures is also due to the lower secondary electron emission coefficient γ_{He} of helium ions on MgO, as compared to the coefficient γ_{Ne} of neon ions.

From a practical point of view, we note from Fig. 4.2a and 4.2c that the tradeoff between electron excitation efficiency and breakdown voltage level is similar for He-Xe mixtures as

---

[4] $\nu_{\mathrm{exc}} = \sum_{i=1}^{N_{\mathrm{exc}}} \nu_{\mathrm{exc},i}$, where the summation is taken over the $\mathrm{Xe}^*(^3\mathrm{P}_1), \mathrm{Xe}^*(^3\mathrm{P}_2)$ and Xe^{**} excited states.

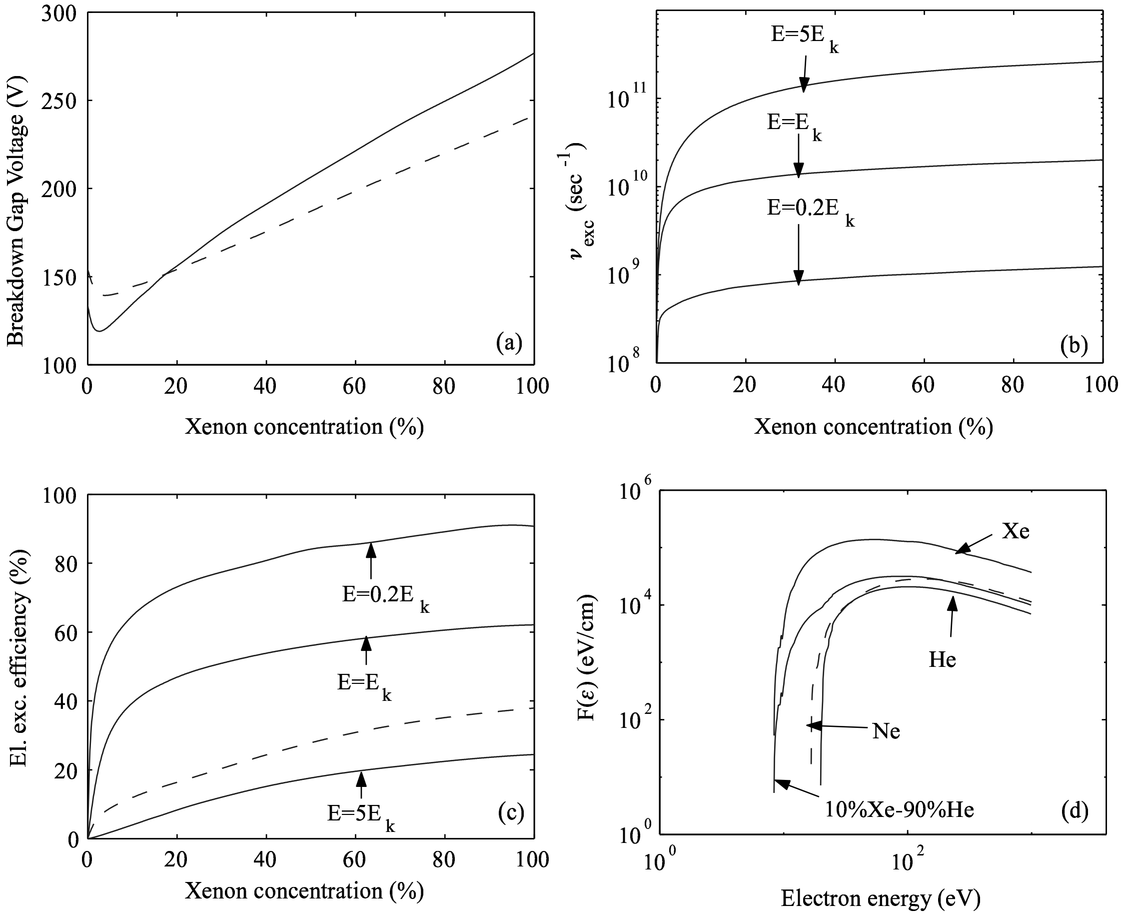

Figure 4.2 (a) Breakdown gap voltage as a function of N_{Xe} in He-Xe mixtures, calculated using (4.3). The dashed line shows the mid-margin gap voltage, calculated using the 1D model. (b) Excitation frequency ν_{exc} as a function of N_{Xe}. (c) Electron excitation efficiency (%) $\eta_{\text{exc},e}$ as a function of N_{Xe}. The dashed line shows the excitation efficiency of the discharge, calculated using the 1D model. (d) The loss function as a function of electron energy in a pure He gas, a pure Ne gas (dashed line), a pure Xe gas and a 10% Xe - 90% He gas mixture.

for Ne-Xe mixtures.

4.3.3 Ne-Xe-Ar Mixtures

In Section 4.3.1, we saw that, for Ne-Xe mixtures, the electron excitation efficiency $\eta_{\mathrm{exc},e}$ is an increasing function of N_{Xe}. However, the breakdown field E_k is also an increasing function of N_{Xe}. In addition, in Section 4.3.2 we saw that Ne-Xe mixtures are more efficient than He-Xe mixtures. In this section we investigate the effect of adding a small amount of Ar in Ne-Xe mixtures, as is done in some PDP designs.

Fig. 4.3a shows $V_g \equiv E_k D$ as a function of Ar concentration N_{Ar} in a mixture with $N_{\mathrm{Xe}}/N_{\mathrm{Ne}} = 5/95$. We observe that E_k decreases when small amounts of Ar are added, due primarily to the Penning ionization reaction of Ar atoms with Ne metastable atoms, as described in equation (4.7). By examination of the loss functions of Ne, Ar and Xe, plotted in Fig. 4.3d we observe that the friction losses are higher in Ar than in Ne. Thus, when Ar is added to the mixture, the dynamic friction force on electrons increases, and we would ordinarily expect to see a corresponding increase in E_k. However, E_k actually decreases due to Penning ionization of Ar atoms by Ne metastables which is very efficient, as mentioned above. We note from Fig. 4.3a that E_k is minimized at $N_{\mathrm{Ar}} \simeq 0.01N$. For $N_{\mathrm{Ar}} > 0.01N$ the increased losses dominate over the Penning ionization effect and E_k increases. Fig. 4.3b shows the electron excitation efficiency of the gas mixture as a function of N_{Ar}. The efficiency slightly increases when small amounts of Ar are added. Thus, adding a small amount of Ar to a Ne-Xe mixture, both decreases E_k and increases $\eta_{\mathrm{exc},e}$. However, both of these improvements are relatively small, being less than $\sim$1%.

Fig. 4.3c shows $V_g \equiv E_k D$ as a function of N_{Ar} in a mixture with $N_{\mathrm{Xe}}/N_{\mathrm{Ne}} = 10/90$. The Penning effect is less important in comparison with the previous case because of the higher Xe concentration. As a result, the effect of the increased losses dominates and E_k increases when small quantities of Ar are added to the mixture.

Based on the results shown in Fig. 4.3, there does not seem to be any significant advantage in using small amounts of Ar in Ne-Xe mixtures, at least from the point of view of fundamental properties of the gases.

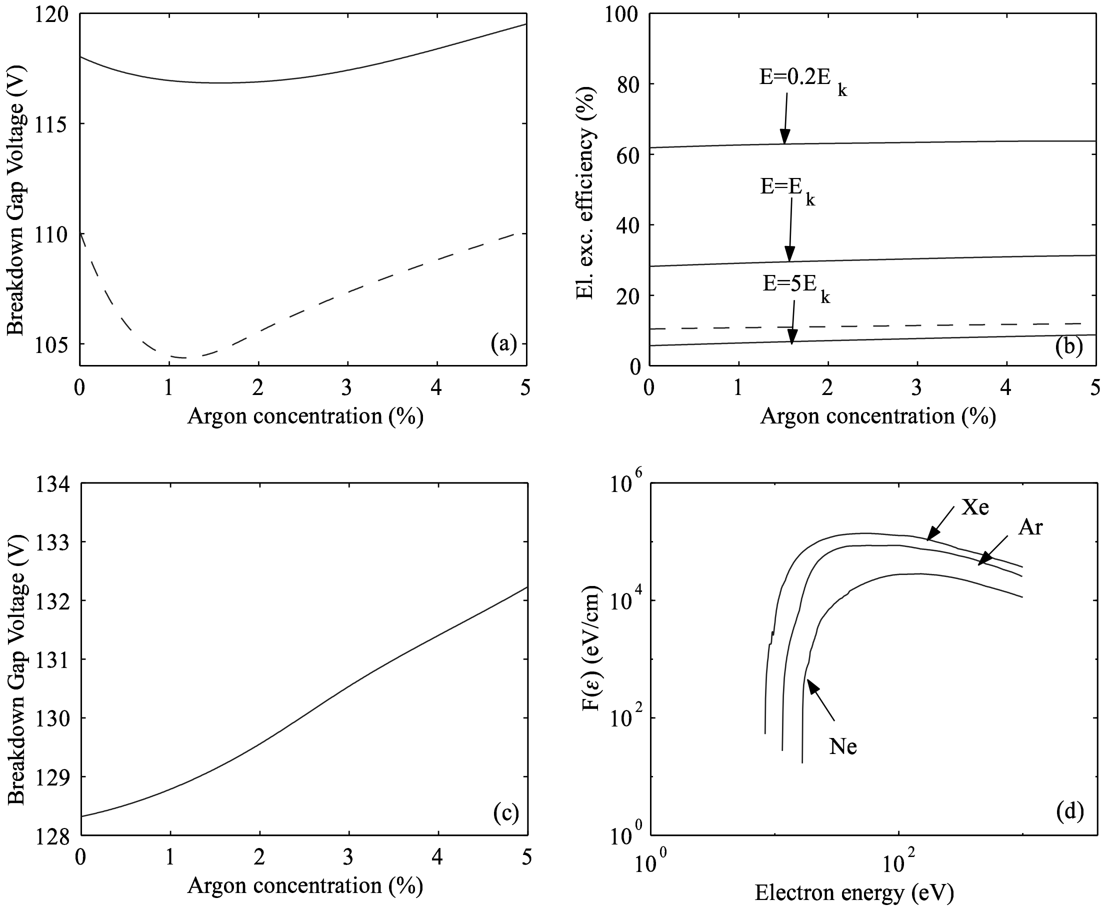

Figure 4.3 (a) Breakdown gap voltage as a function of Ar concentration N_{Ar} in a mixture with $N_{\mathrm{Xe}}/N_{\mathrm{Ne}} = 5/95$, calculated using (4.5). The dashed line shows the mid-margin gap voltage, calculated using the 1D model. (b) Electron excitation efficiency (%) $\eta_{\mathrm{exc},e}$ as a function of N_{Ar} in a mixture with $N_{\mathrm{Xe}}/N_{\mathrm{Ne}} = 5/95$. The dashed line shows the excitation efficiency of the discharge, calculated using the 1D model. (c) Breakdown gap voltage as a function of N_{Ar} in a mixture with $N_{\mathrm{Xe}}/N_{\mathrm{Ne}} = 10/90$, calculated using (4.5). (d) The loss function as a function of electron energy in a pure Ne gas, a pure Xe gas and a pure Ar gas.

4.4 Comparison with 1D simulation results

In order to assess the validity of conclusions derived from our fundamental kinetic analysis of unbounded and homogeneous gas mixtures, we use a one-dimensional self-consistent simulation of an AC PDP cell (Section 3.3), similar to those previously developed by *Meunier et al.* [1995] and *Punset et al.* [1998]. The data used in the 1D model, such as electron-atom collision cross sections, secondary electron emission coefficients, and reaction rates are identical to those used in the homogeneous and unbounded kinetic model. The gap length D, the pressure p, and the gas temperature T are also chosen to be the same as in the unbounded model. Other model parameters such as length and relative permittivity of dielectrics are identical to those used in *Meunier et al.* [1995]. We also note that in the results presented in this section, the local field approximation is used instead of the electron energy equation (Section 3.1.1).

We use the 1D model to calculate the voltage margin of stable operation of the cell (Section 1.2) by the voltage transfer curve method, introduced by *Slottow and Petty* [1971] and also described in *Meunier et al.* [1995]. In each case, we use an applied voltage corresponding to operation in the middle of the calculated voltage margin, to determine the excitation efficiency of the discharge η_{exc}, calculated using (3.17).

The dashed line curve in Fig. 4.1a shows the variation of the mid-margin sustaining voltage in the gap V_{sg} as a function of the Xe concentration N_{Xe} in a Ne-Xe mixture. V_{sg} is given by

$$V_{sg} = \left[\frac{C_d}{C_d + C_g}\right] \frac{V_{\text{Smin}} + V_{\text{f}}}{2}$$

where C_d is the equivalent capacitance of the dielectric layers, C_g is the gas gap capacitance (Fig. 3.2a), and V_{Smin}, V_{f} are the calculated values of the minimum sustaining voltage and the firing voltage respectively. The dashed curve in Fig. 4.1c shows the variation of the discharge excitation efficiency η_{exc} as a function of N_{Xe} in Ne-Xe mixtures for a middle-margin applied sustaining voltage. These 1D results show that the sustaining voltage and the discharge excitation efficiency of the PDP cell exhibit very similar dependence on N_{Xe} with the corresponding quantities of the unbounded homogeneous kinetic model. This similarity is further illustrated in Fig. 4.4a, where we show the normalized derivative of the electron excitation efficiency ($\eta_{\text{exc},e}^{-1} d\eta_{\text{exc},e}/d[N_{\text{Xe}}/N]$) as a function of N_{Xe}. The dashed line curve shows the normalized derivative of the discharge excitation efficiency, ($\eta_{\text{exc}}^{-1} d\eta_{\text{exc}}/d[N_{\text{Xe}}/N]$) calculated with the 1D simulation. This plot illustrates that the

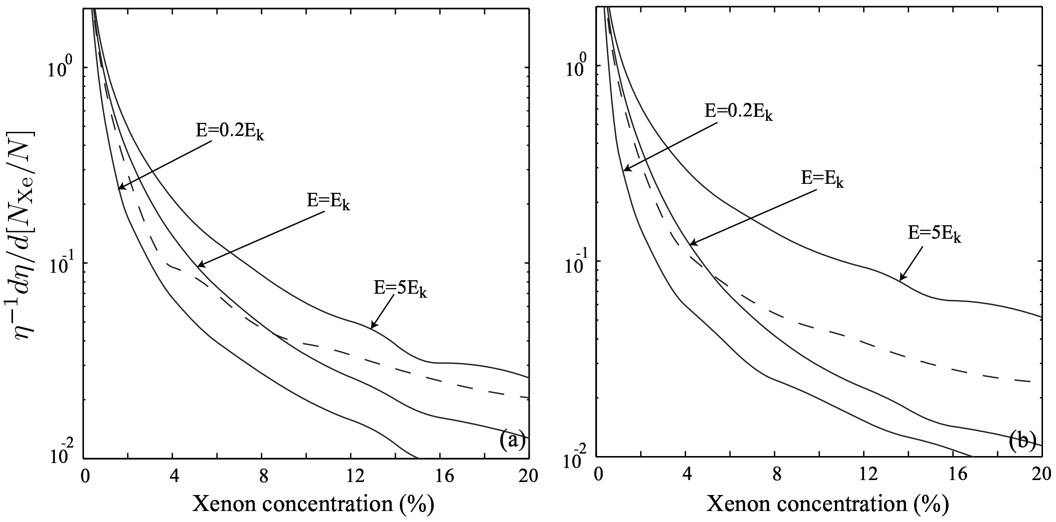

Figure 4.4 (a) Normalized derivative of the electron excitation efficiency $\eta_{\mathrm{exc},e}$ as a function of N_{Xe} in Ne-Xe mixtures. The dashed line shows the normalized derivative of the excitation efficiency of the discharge, calculated using the 1D model. (b) Normalized derivative of the electron excitation efficiency $\eta_{\mathrm{exc},e}$ as a function of N_{Xe} in He-Xe mixtures. The dashed line shows the normalized derivative of the excitation efficiency of the discharge, calculated using the 1D model.

fractional increase in excitation efficiency is very small for $N_{\mathrm{Xe}} > 0.1N$. It also illustrates that the dependence of the discharge excitation efficiency η_{exc}, as defined in (3.17), on N_{Xe} is determined by the fundamental property $\eta_{\mathrm{exc},e}$ of the gas mixture, defined in (3.21).

The dashed lines in Figures 4.2a, 4.2c, and 4.4b show similar results for He-Xe mixtures. In agreement with the unbounded and homogeneous kinetic model, it is found that V_{sg} is higher in a He-Xe mixture compared with a Ne-Xe mixture with the same Xe concentration and that the discharge excitation efficiency is lower. It should be noted that He exhibits a very gradual rise in the slope of the voltage transfer curve [*Veerasingam et al.*, 1996]. We found that this is mainly due to the high electron momentum transfer cross section of He. In agreement with *Veeresingam et al.* [1996], we found that this effect results in disagreement between the actual V_{Smin}, V_{f} and those calculated using the voltage transfer curve method for He-Xe mixtures with high He concentrations. However, in the discharge excitation efficiency calculation we used an applied sustaining voltage which results in a stable discharge.

The dashed curves in Figures 4.3a, and 4.3b show V_{sg} and discharge excitation efficiency as a function of Ar concentration N_{Ar} in a mixture with $N_{\mathrm{Xe}}/N_{\mathrm{Ne}} = 5/95$. In agreement with the results of the unbounded homogeneous model, V_{sg} is minimized at $N_{\mathrm{Ar}} \simeq 0.01N$ due to Penning ionization, and the excitation efficiency slightly increases when small amounts of Ar are added. Although these improvements of ~5% seem to have been underestimated by the unbounded homogeneous model, the fact that they are still small confirms that there is no significant advantage in using small amounts of Ar in Ne-Xe mixtures.

Chapter 5

Studies of the coplanar-electrode and other previously proposed PDP cell designs

5.1 Introduction

In this chapter, we use the two-dimensional (2-D) self-consistent model described in Section 3.1 to simulate the microdischarges in a standard coplanar-electrode PDP cell. We investigate the effect of the variation of the cell design parameters on the operating voltages and UV efficiency of the device. In addition, we use the model to study two alternative designs which have been proposed to improve the performance of the standard coplanar-electrode PDP [*Kim et al.*, 2000; *Hashimoto and Iwata*, 1999]. First, we investigate the effect of the insertion of floating conducting materials in the dielectric layer covering the sustain electrodes. Secondly, we investigate the effect of applying a non-standard voltage waveform including assistant voltage pulses between the sustain electrodes. In the remainder of the chapter, we present the results of our model for the standard coplanar-electrode PDP (Section 5.2) and the two alternative designs (Sections 5.3, 5.4).

5.2 Standard coplanar-electrode geometry

In this section, we study the effect of the variation of the cell geometry parameters on the performance of the device. In all cases, the gas mixture filling the region between the dielectrics is a 4% Xe-Ne mixture at a pressure of 500 Torr. The basic cell geometry is as shown in Figure 3.2b. The height and width of the cell are H=210μm and L=1260μm respectively. The length of the lower dielectric layer is d_2=30μm. We investigate the effect of the variation of the electrode gap length g, the sustain electrode width w, the length of the upper dielectric layer d_1 and the dielectric constant ε_r of the dielectric layers on the operating voltages and the efficiency of the PDP cell. Our reference case is characterized by the parameter values g=100μm, w=300μm, d_1=30μm, and ε_r=10. The voltages applied to the three electrodes during the simulation are shown in Figure 3.6.

5.2.1 Voltage margin

We first study the effect of geometric parameters on the operating voltages of the device.

We investigate the effect of the design parameters g, w, d_1, ε_r (Fig. 3.2b) on the minimum sustaining voltage V_{Smin} and the firing voltage V_{f} (Section 1.2). For the calculation of V_{f} a sustain pulse V_{S} is applied to one of the sustain electrodes and A is biased to $\frac{V_{\mathrm{S}}}{2}$ (Fig. 3.6). We use the 2-D model to iteratively calculate (to within an accuracy of a volt) the minimum voltage V_{f} which leads to breakdown. In all cases the breakdown occurs between the two sustain electrodes.

For the calculation of V_{Smin} we first apply the address pulses V_{D} and $-V_{\mathrm{SW}}$ described in Section 3.4. In all cases, we use V_{SW}=150V, and for the reference case V_{D}=80V. In all other cases, V_{D} is chosen so that the breakdown parameter [*Raizer*, 1997, p. 131]

$$\mu = (\alpha_{\mathrm{Ne}}\gamma_{\mathrm{Ne}} + \alpha_{\mathrm{Xe}}\gamma_{\mathrm{Xe}}) \left[e^{(\alpha_{\mathrm{Ne}}+\alpha_{\mathrm{Xe}})D} - 1\right] / (\alpha_{\mathrm{Ne}} + \alpha_{\mathrm{Xe}}) \tag{5.1}$$

is constant, where α_{Ne} and α_{Xe} are the partial first Townsend ionization coefficients for Ne and Xe respectively, and D is the discharge gap (Fig. 3.2b). A sequence of sustaining pulses V_{S} is then applied between the sustain electrodes (Fig. 3.6). We use the 2-D model (in an iterative fashion) to calculate (to within an accuracy of a volt) the minimum voltage V_{Smin} which leads to a steady sequence of sustain discharges. We note that the voltage transfer curve method [*Slottow and Petty*, 1971], which was used in Section 4.4 for the calculation of V_{Smin} and V_{f}, applies only to the simpler PDP geometry of Fig. 3.2a and thus cannot be used for the coplanar-electrode geometry (Fig. 3.2b).

The results are shown in Figure 5.1. V_{f} is an increasing function of g, as expected. Larger g results in longer discharge paths between the two sustain electrodes, requiring

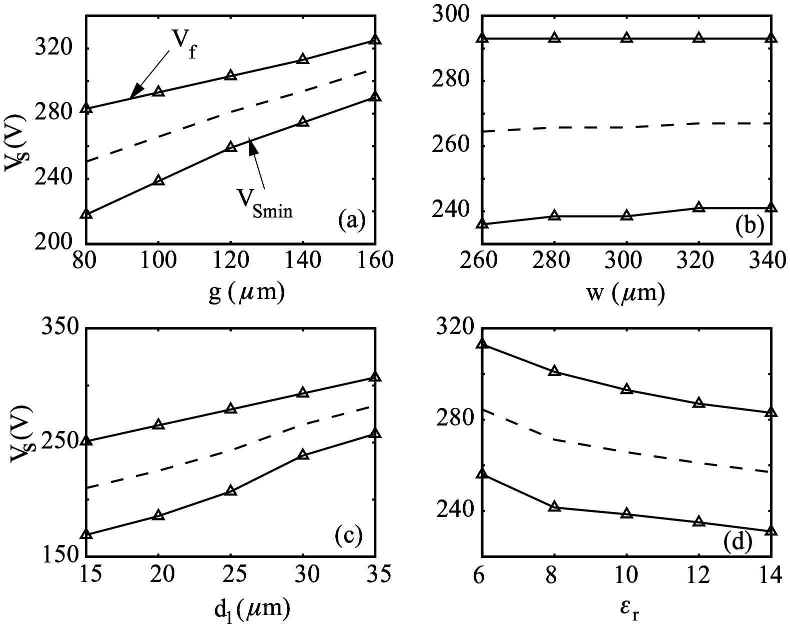

Figure 5.1 (a) The firing voltage V_{f} and the minimum sustaining voltage V_{Smin} as a function of the sustain electrode gap g. The dashed line shows the mid-margin sustaining voltage V_{Sm} used for the calculation of UV efficiency. (b) V_{f}, V_{Smin}, and V_{Sm} as a function of the sustain electrode width w. (c) V_{f}, V_{Smin}, and V_{Sm} as a function of the upper dielectric layer length d_1. (d) V_{f}, V_{Smin}, and V_{Sm} as a function of the dielectric constant ε_r.

larger voltages for breakdown. The voltage margin (Section 1.2), defined as $V_{\mathrm{f}} - V_{\mathrm{Smin}}$, decreases with g, due to the fact that if g is increased while D is kept constant, the breakdown voltage between the two sustain electrodes increases while the breakdown voltage between the sustain and address electrodes remains constant. The address-sustain discharge path then becomes increasingly favorable over the sustain-sustain path, thus limiting the window of stable operation of the device. Variation of the sustain electrode width w has no significant effect on V_{f} or V_{Smin}. The electric field distribution in the region between the two sustain electrodes is not significantly perturbed as w is varied, so that V_{f} and V_{Smin} remain almost constant with w. We see that V_{f} is an increasing function of d_1. As d_1 is increased, the voltage drop in the gap decreases if the applied voltage is kept constant. Thus, higher voltages are required to cause breakdown. The voltage margin is a decreasing function of d_1. We note that the cell height H is kept constant in our calculations, so that as d_1 decreases, the gap D increases. Thus, the sustain-sustain discharge path becomes increasingly favorable over the address-sustain path and the window of stable sustain operation becomes wider. Finally, V_{f} is a decreasing function of the dielectric constant ε_r. As ε_r is increased, the voltage drop in the gap increases for constant applied voltage. Thus, lower voltages are required to cause breakdown. The variation of ε_r has no significant effect on the voltage margin of the cell, since in both the sustain-sustain and address-sustain paths the voltage drop is increased as ε_r is increased.

5.2.2 Total UV energy and UV efficiency

We next study the effect of geometric parameters of the PDP cell on UV emission.

A similar study has been previously done by *Rauf and Kushner* [1999b] . In their work, the applied sustaining voltage used for the calculation of efficiency was kept constant as the geometric parameters were varied. In addition, the efficiency calculation was based on the first sustaining pulse following an initial address pulse. In our work, the voltage waveform shown in Fig. 3.6 is applied in all cases to the cell electrodes. The sustaining voltage is chosen to be the mid-margin voltage, shown in Fig. 5.1 with a dashed line, defined as $V_{\mathrm{Sm}} = (V_{\mathrm{Smin}} + V_{\mathrm{f}})/2$ rather than a constant reference voltage. The mid-margin voltage is usually chosen as the point of operation of the PDP to ensure reliability. If a constant reference voltage were used for the calculation of efficiency, the value used might be outside the operating window in some cases, as it can be seen in Fig. 5.1. In addition, we calculate the UV efficiency of the PDP cell in the periodic steady state. We found that during the first

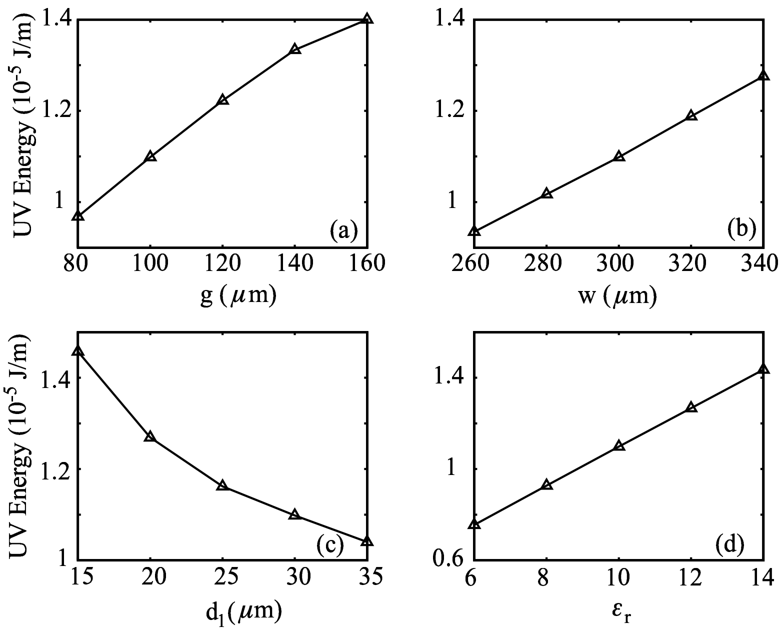

Figure 5.2 (a) Total UV energy emitted per sustain pulse as a function of the sustain electrode gap g. (b) Total UV energy emitted per sustain pulse as a function of the sustain electrode width w. (c) Total UV energy emitted per sustain pulse as a function of the upper dielectric layer length d_1. (d) Total UV energy emitted per sustain pulse as a function of the dielectric constant ε_r.

few sustaining pulses the device is in a transient state. The efficiency during this transition time may be quite different (by as much as a factor of 3) from the steady state efficiency.

In Figure 5.2 we show the total UV energy emitted per sustain pulse (T_{pulse} =4μs) as a function of the geometric parameters of the cell, calculated using (3.11) and (3.13). The UV energy is an increasing function of the gap length g. As the gap length g increases, the discharge path length also increases. As a result, the total energy dissipated by electrons, the energy spent in Xe excitation and consequently the UV emission energy increase. The UV energy is also an increasing function of the sustain electrode width w. As mentioned above, the breakdown initially occurs in the region between the two sustain electrodes where the electric field is higher. As the dielectric surface above the electrodes is covered with charge, the discharge path moves towards the outer ends of the electrodes. This process continues until all the dielectric surface above the electrodes is covered with charge. The total duration of the current pulse is therefore proportional to the electrode width, and the total dissipated energy by electrons, the energy spent in Xe excitation and the UV emission energy increase as the electrode width is increased. Finally, we observe that the UV energy per sustain pulse increases as d_1 is decreased or ε_r is increased. Both decreasing d_1 or increasing ε_r result in increasing the capacitance of the upper dielectric layer [*Rauf and Kushner*, 1999b]. As the capacitance of the dielectric layer is increased more energy has to be dissipated during the discharge before it is quenched by surfaces charges. We note that as d_1 is decreased or ε_r is increased the operating voltages decrease (see Fig. 5.1). However, the effect of increased capacitance dominates, since the rate of change of the capacitance with respect to d_1 or ε_r is much higher than the rate of change of the mid-margin operating voltage with respect to the same parameters.

In Figure 5.3 we show the UV efficiency η_{UV}, as defined in (3.18), as a function of the geometric parameters of the cell. We observe that by increasing the gap from 80μm to 160μm the UV efficiency increases by ~25%. Variation of the electrode width w results in insignificant change in the efficiency. Increasing the upper dielectric layer length from 15μm to 35μm results in a ~15% increase in efficiency. Finally, decreasing the dielectric constant ε_r from 14 to 6 results in a ~8% increase in efficiency.

In order to interpret these results, we focus our attention on the excitation efficiency η_{exc}, as defined in (3.17). The UV efficiency η_{UV} is always lower than the excitation efficiency η_{exc} because in the series of reactions that lead to UV photon production part of the energy of the Xe excited states is lost through cascading to lower states, and because some excited atoms are lost through diffusion to the walls. In all cases considered, we found that η_{UV} and η_{exc} are directly related and the effect of the variation of any geometric parameter is the same on both. This is expected since in all cases the gas mixture composition and consequently the rate coefficients of reactions involving excited species are the same. Due to the long lifetimes of some of the excited states of Xe which lead to UV emission (Table 3.3), some UV photons are emitted several μs after the corresponding electron impact excitation reaction. In addition, due to particle diffusion and to reabsorption of resonance radiation at 147nm (Section 3.1.2), the physical location of UV photon emission can be different from that of the corresponding electron impact excitation reaction. As a result, UV emission does not coincide with the corresponding energy dissipation neither temporally nor spatially. On the other hand, if the local equilibrium approximation is assumed, the energy gain from the electric field is locally (in space and in time) balanced by the loss due to collisions. In other words, in the case of excitation efficiency a spatially and temporally local quantity defined

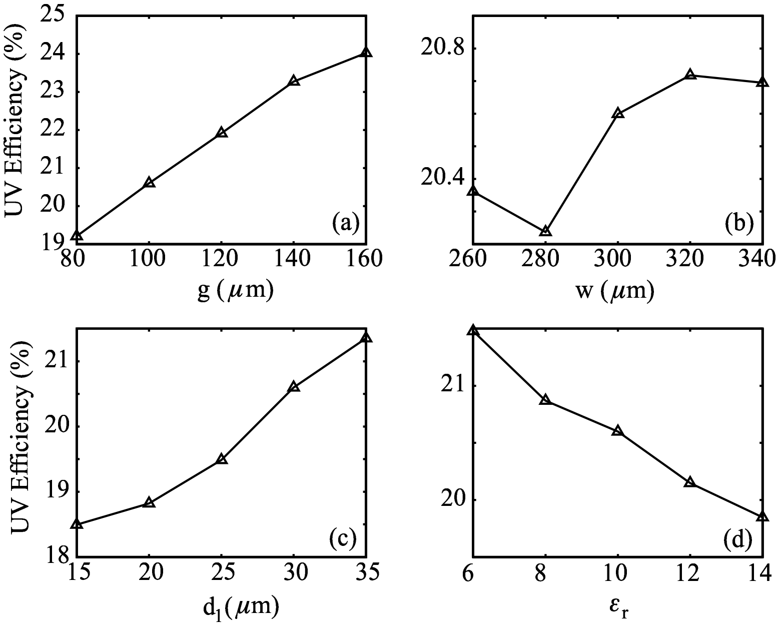

Figure 5.3 (a) UV efficiency as a function of the sustain electrode gap g. (b) UV efficiency as a function of the sustain electrode width w. (c) UV efficiency as a function of the upper dielectric layer length d_1. (d) UV efficiency as a function of the dielectric constant ε_r.

as

$$\tilde{\eta}_{\text{exc}}(x,y,t) = \frac{\sum_{i=1}^{N_{\text{exc}}} n_e \nu_{\text{exc},i} \varepsilon_{\text{exc},i}}{(\mathbf{J}_\text{e} + \sum_{i=1}^{N_{\text{ion}}} \mathbf{J}_{\text{ion},i}) \cdot \mathbf{E}}$$

is meaningful (compare with (3.17)), while a similar quantity cannot be defined in the case of UV efficiency for the reasons given above. Nevertheless, careful examination of the local excitation efficiency $\tilde{\eta}_{\text{exc}}(x,y,t)$ can give useful insight into the factors that govern UV efficiency.

The excitation efficiency can also be written as

$$\eta_{\text{exc}} = \int_V dv \left[\int_T dt \frac{p_{\text{exc}}}{\varepsilon_{\text{tot}}} \right] = \int_V dv \left[\frac{\int_T dt p_{\text{exc}}}{\int_T dt p_{\text{tot}}} \frac{\int_T dt p_{\text{tot}}}{\varepsilon_{\text{tot}}} \right] \tag{5.2}$$

where p_{exc}, $p_{\text{tot}} = p_\text{e} + p_\text{i}$, and $\varepsilon_{\text{tot}} = \varepsilon_\text{e} + \varepsilon_\text{i}$ have been defined in Section 3.2. In Figure 5.4 we show the quantities $f_1(x,y) = \int_T dt p_{\text{exc}} / \int_T dt p_{\text{tot}}$, $f_2(x,y) = \int_T dt p_{\text{tot}} / \varepsilon_{\text{tot}}$ and $f(x,y) = f_1(x,y) f_2(x,y)$ for the g=80μm and the g=160μm cases (the rest of the parameters are those of the reference case). It can be seen from (5.2) that f_1 is the spatially local

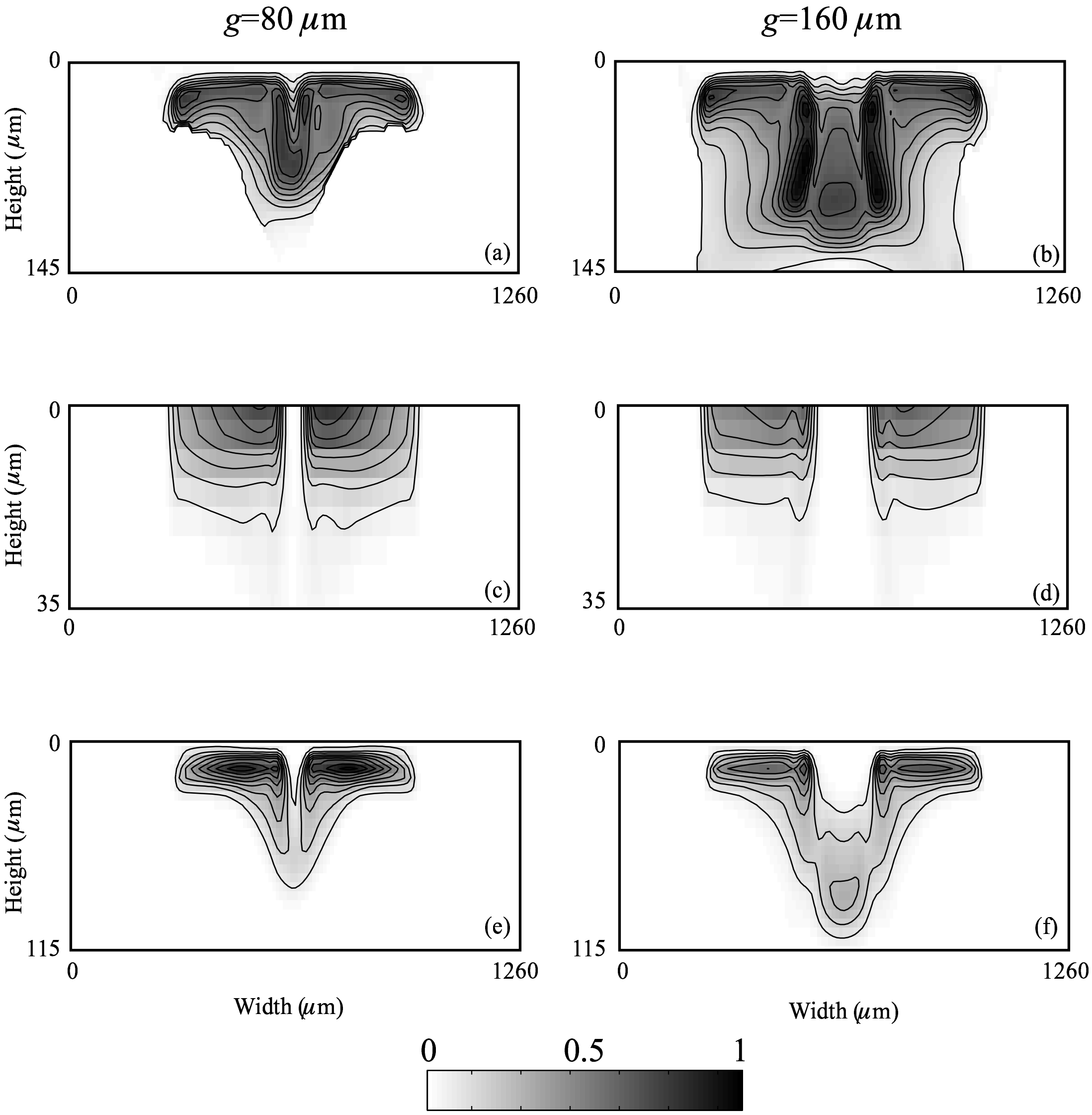

Figure 5.4 (a), (b) Local excitation efficiency for the g=80μm and the g=160μm cases. The increment between the contours is 0.1. The maximum in the gray scale corresponds to 1. (c), (d) Normalized dissipated energy density for the g=80μm and the g=160μm cases. The increment between the contours is $2.10\times10^7\,\mathrm{m}^{-2}$. The maximum in the gray scale corresponds to $2.10\times10^8\,\mathrm{m}^{-2}$. (e), (f) Normalized density of energy spent in Xe excitation for the g=80μm and the g=160μm cases. The increment between the contours is $2.83\times10^6\,\mathrm{m}^{-2}$. The maximum in the gray scale corresponds to $2.83\times10^7\,\mathrm{m}^{-2}$. Note the different vertical scale in each plot. In all cases height is measured from the MgO layer surface.

excitation efficiency, f_2 is normalized dissipated energy, and $f = f_1 f_2$ is a quantity which, if spatially integrated, gives the excitation efficiency, i.e. $\eta_{\rm exc} = \int_V dv f(x,y)$. We observe that f is wider in the g =160μm case, while the maximum value of f is higher in the g=80μm case. The discharge path between the two sustain electrodes is wider for wider g, as explained above. The overall excitation efficiency is higher in the g=160μm case. In both cases we observe that the dissipated energy, i.e. f_2, is high in the region directly below the dielectric layer covering the sustain electrodes, where the sheath is formed during the discharge. There is also some energy dissipation in the area between the two electrodes. We also observe that the local excitation efficiency is high in the region between the two electrodes in both cases. It is also high a few μm away from the dielectric layer. A similar picture is observed in Figure 5.5 when comparing the d_1=15μm and d_1=35μm cases. We observe that f is wider in the d_1 =35μm case, while the maximum value of f is higher in the d_1=15μm case with the overall excitation efficiency being higher in the d_1 =35μm case. In this case, as d_1 is decreased, D increases (because H is kept constant) so that the sustain-sustain path becomes increasingly favorable over the sustain-address path, as explained above, and the sustain discharge becomes more confined in the region directly below the upper dielectric layer. The dissipated energy is high in the region directly below the dielectric layer covering the sustain electrodes, and the local excitation efficiency is higher in the region between the two electrodes. A similar picture is observed in all cases examined.

Our conclusion from the study of the excitation efficiency is that the wider the discharge area the higher the overall efficiency. In all cases, the discharge area can be divided into two regions: The first is the sheath region where most of the energy dissipation takes place. The efficiency is not very high in this region, since most of the energy is dissipated by the ions. The second is the region between the two electrodes where the initial discharge path is formed. Energy in this region is mostly dissipated by electrons and the efficiency is high. The local excitation efficiency can also be written as

$$\tilde{\eta}_{\rm exc}(x,y,t) = \frac{\mathbf{J}_{\rm e}\cdot\mathbf{E}}{(\mathbf{J}_{\rm e}+\sum_{i=1}^{N_{\rm ion}}\mathbf{J}_{{\rm ion},i})\cdot\mathbf{E}} \frac{\sum_{i=1}^{N_{\rm exc}} n_e \nu_{{\rm exc},i}\varepsilon_{{\rm exc},i}}{\mathbf{J}_{\rm e}\cdot\mathbf{E}} = \tilde{\eta}_1(x,y,t)\tilde{\eta}_2(x,y,t) \qquad (5.3)$$

where $\tilde{\eta}_1$ is a measure of how efficiently the electrons are heated by the electric field, while $\tilde{\eta}_2$ is a measure of how efficiently the electrons excite Xe atoms (Section 3.2.1). It is interesting to note that both $\tilde{\eta}_1$ and $\tilde{\eta}_2$ are higher in the region between the two electrodes. The electric

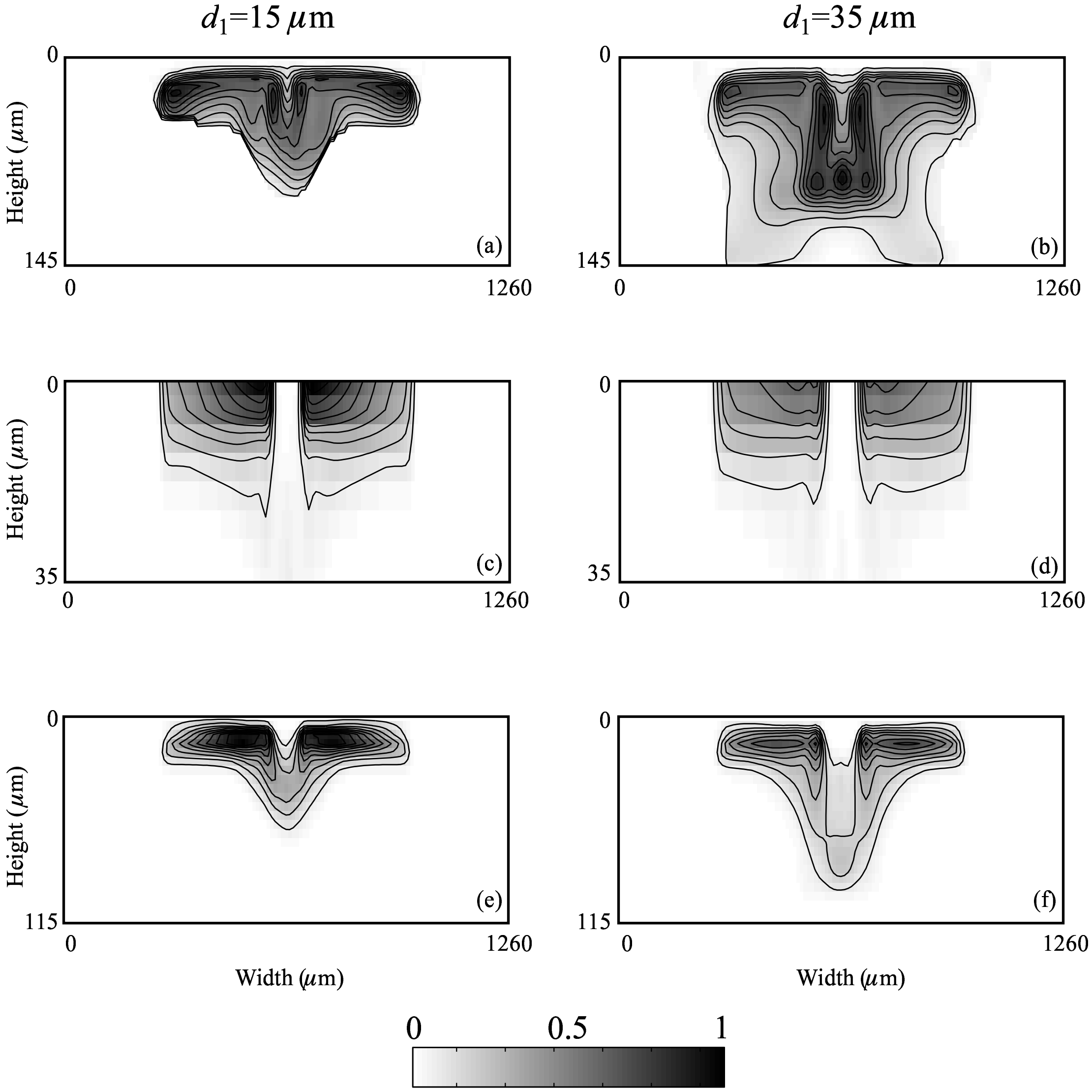

Figure 5.5 (a), (b) Local excitation efficiency for the d_1=15μm and the d_1=35μm cases. The increment between the contours and maximum in gray scale are the same as in Figures 5.4a and 5.4b. (c), (d) Normalized dissipated energy density for the d_1=15μm and the d_1=35μm cases. The increment between the contours and maximum in gray scale are the same as in Figures 5.4c and 5.4d. (e), (f) Normalized density of energy spent in Xe excitation for the d_1=15μm and the d_1=35μm cases. The increment between the contours and maximum in gray scale are the same as in Figures 5.4e and 5.4f. Note the different vertical scale in each plot. In all cases height is measured from the MgO layer surface.

field is lower during the discharge in the region between the two electrodes compared to the high electric field of the sheath region directly below the dielectric layer. The quantity $\tilde{\eta}_2$ is higher for lower electric fields (Section 4.3.1) [*Veronis et al.*, 2000] (this is true for $E \simeq E_k$, where E_k is the breakdown electric field)[1] , while $\tilde{\eta}_1$ is also higher in the region between the electrodes, since the sheath region is dominated by the ionic current.

The overall efficiency increases as the highly efficient discharge region between the two electrodes becomes wider. It is for this reason that the UV efficiency of the discharge increases as g or d_1 is increased or as ε_r is decreased. From a practical point of view, we note that in all three cases the increase in efficiency is accompanied by an increase in the operating voltages. We can conclude that in the standard coplanar-electrode geometry there is a trade-off between high UV efficiency and low operating voltages. If the electrode width w is varied, there is no significant change in the efficiency, as mentioned above, since the spatial extent of the discharge region between the two electrodes does not change. We finally note that the dependence of efficiency on the geometric parameters of the cell is directly related to the spatial extent of the discharge, so that uncertainties in model data such as cross sections and rate coefficients do not have a significant effect on this result.

In Figures 5.6a and 5.6b we show the normalized density of energy spent in Xe excitation calculated using the electron energy equation and the local field approximation respectively (Section 3.1.1). Results are presented for the reference case. In the case of the local field approximation we use the effective electric field expression introduced in *Punset et al.* [1998]. In agreement with *Rauf and Kushner* [1999a], we observe that use of the local field approximation substantially modifies the discharge characteristics. The more detailed treatment of electron impact reaction rates and transport coefficients with the electron energy equation results in a wider discharge region. We found that the local field approximation underestimates the electron ionization and excitation coefficients in the bulk plasma region because it does not take into account energy transport from the cathode region to the colder bulk plasma region through thermal conduction and drift of warm electrons from the cathode region [*Rauf and Kushner*, 1999a]. As a result, a more confined

---

[1] Note that $\tilde{\eta}_2$ is exactly the same as the fundamental inherent property of the gas mixture $\eta_{\mathrm{exc},e}$, defined by (3.21), only if the local field approximation holds (Section 3.1.1). Thus, in our model, these quantities are not exactly equal, since we take into account the electron energy redistribution due to thermal conduction and convection, by using the electron energy equation. However, in typical high pressure PDP conditions, the electron temperature is almost in equilibrium with the applied electric field, so that the conclusions derived in Chapter 4 for $\eta_{\mathrm{exc},e}$ safely apply also to $\tilde{\eta}_2$.

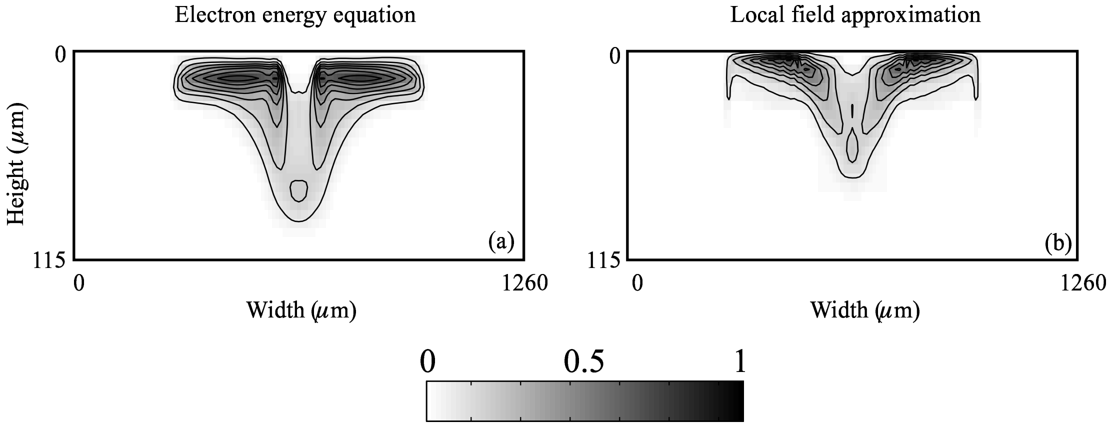

Figure 5.6 (a) Normalized density of energy spent in Xe excitation calculated using the electron energy equation. (b) Normalized density of energy spent in Xe excitation calculated using the local field approximation. Results are presented for the reference case. The increment between the contours and maximum in gray scale are the same as in Figures 5.4e and 5.4f. Height is measured from the MgO layer surface.

discharge region is predicted, which, in agreement with our previous discussions, results in substantially lower discharge efficiency. We found that when the local field approximation is used instead of the electron energy equation the excitation efficiency is ~32% lower for the reference case. Similarly large errors in the calculation of discharge efficiency when the local field approximation is used instead of the electron energy equation are reported in *Hagelaar et al.* [2001].

5.3 Effect of floating electrodes

In this section, we investigate the effect of the insertion of floating electrodes in the upper dielectric layer. The geometry of the PDP cell with floating electrodes is as shown in Figure 5.7. The use of floating electrodes has been proposed as a way to improve the performance of the PDP cell [*Kim et al.*, 2000].

In our studies, we choose the width of the floating electrodes to be w_f=150μm, and the distance from the sustain electrodes to be d_f=20μm (Fig. 5.7). All other parameters were chosen to be the same as in the reference case. In addition, the same driving scheme was used (Fig. 3.6). Since the floating electrodes are inserted in the region below the outer ends of the sustaining electrodes, no significant change in the breakdown voltage of the cell

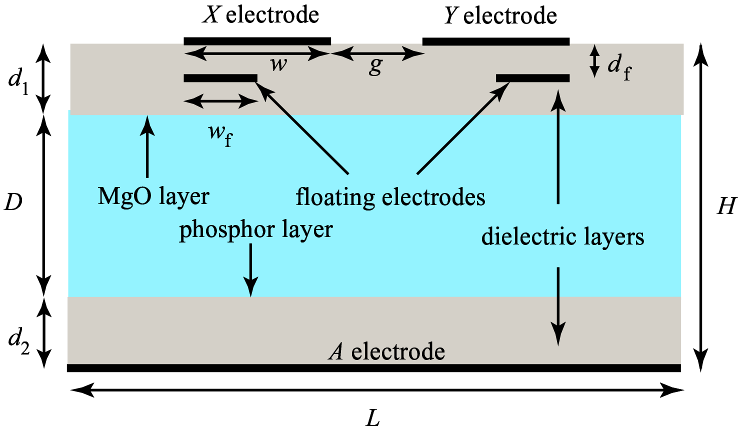

Figure 5.7 Geometry of a coplanar-electrode PDP cell with floating electrodes inserted in the upper dielectric layer.

is expected. We found that for $w_f \leq 200\mu$m the breakdown voltage is the same as in the reference case to within an accuracy of a volt. We therefore applied the same sustaining voltage to compare the floating-electrode PDP cell (Fig. 5.7) with the reference coplanar-electrode PDP cell (Fig. 3.2b), which for brevity will heretofore be referred as the new and standard structures respectively.

In Figures 5.8a and 5.8b, we show the dissipated energy density during one sustaining period (Fig. 3.6) for the standard and new structure cases respectively. In both cases, high dissipated energy density is observed in the regions directly below the dielectric layer covering the sustaining electrodes. We also observe that the high dissipated energy density region is more localized in the new structure case. In Figures 5.8c and 5.8d, we show the total UV emission energy density integrated over all wavelengths considered (147 nm, 150 nm, and 173 nm) during one sustaining period for the standard and new structure cases respectively. We observe that UV emission is confined to the regions below the dielectric surface covering the sustaining electrodes. However, in both cases the region of high UV emission is wider (note the different vertical scales for Figs. 5.8a,b versus Figs. 5.8c,d) when compared to the region of high dissipated energy density (shown in Figs. 5.8a and 5.8b), extending towards the lower dielectric layer. This result is due to diffusion of some of the excited states of Xe which have long lifetimes. In addition, UV emission is more localized in the new structure case, since the region where power is spent by electrons in Xe excitation

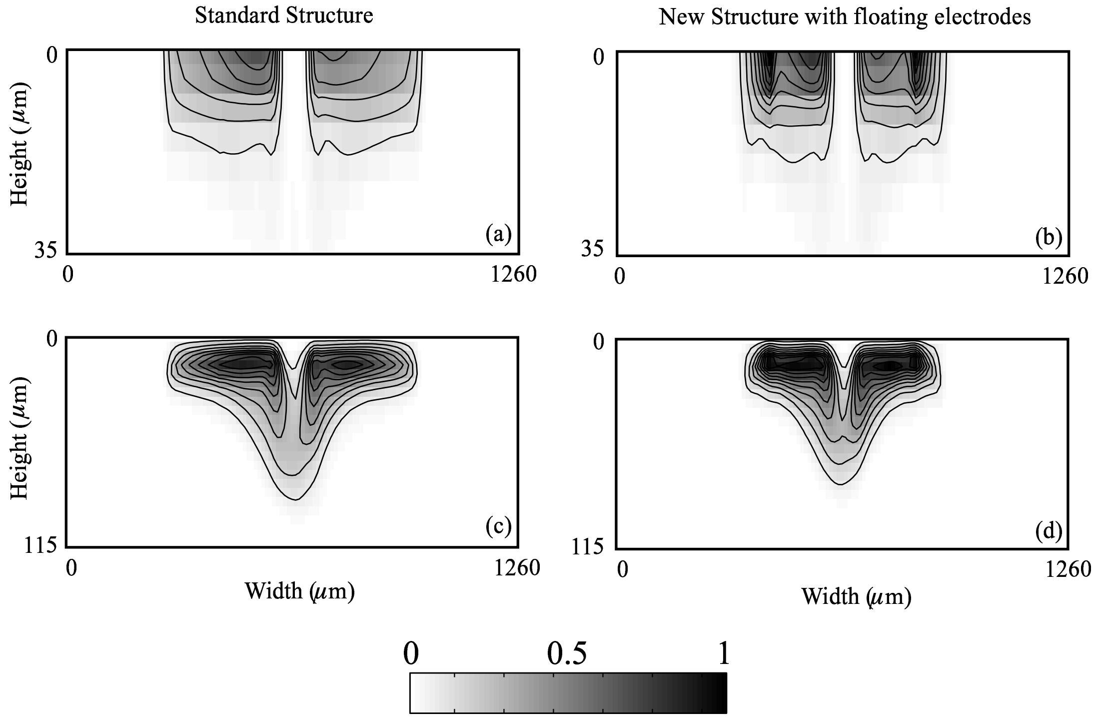

Figure 5.8 (a), (b) Dissipated energy density for the standard and new structures respectively. The increment between the contours is $2.94 \times 10^3\,\mathrm{J\,m^{-3}}$. The maximum in the gray scale corresponds to $2.94 \times 10^4\,\mathrm{J\,m^{-3}}$. (c), (d) UV emission energy density for the standard and new structures respectively. The increment between the contours is $174\,\mathrm{J\,m^{-3}}$. The maximum in the gray scale corresponds to $1.74 \times 10^3\,\mathrm{J\,m^{-3}}$. Note the different vertical scale in each plot. In all cases height is measured from the MgO layer surface.

is more localized, as explained above (Figs. 5.8a and 5.8b). The discharge current and UV emission confinement of the discharge by the new structure is expected to reduce cross talk between adjacent cells in agreement with the experimental findings reported in *Kim et al.* [2000]. The total UV energy emitted per sustain pulse in the new structure case was found to be approximately equal to the UV energy emitted in a coplanar-electrode PDP cell with electrode width w=260μm (Fig. 5.2). However, the emitted UV energy is more confined in the new structure case. The confinement of the discharge in the new structure case results in a ~8% decrease in UV efficiency. Overall, the advantage of the new structure over the standard structure is that the same total amount of UV light can be emitted in a more confined area, thus limiting cross talk with adjacent cells, at the expense of some reduction in efficiency.

In Figures 5.9a and 5.9b, we show the dissipated total power, dissipated electron power, and power spent on Xe excitation in the PDP cell, as defined in (3.19), for the standard and new structure cases respectively. Results are shown as a function of time, during the discharge caused by the 4^{th} sustain pulse applied to the X electrode starting at t=14μs. We observe that the shape of the discharge power pulses are quite different, in agreement with the experimental results for the discharge current waveform [*Kim et al.*, 2000]. For the case of the new cell structure, the voltage waveform has a double-pulse shape. Figures 5.9c and 5.9d show snapshots of the surface charge density deposited on the upper dielectric layer for the standard and new structure cases respectively. Figure 5.9d also shows snapshots of the induced surface charge density on the floating electrodes. The times corresponding to the snapshots are also shown in Figures 5.9a and 5.9b with dots for comparison. It should be noted that during the discharge caused by the 4^{th} pulse, the X electrode acts as the anode, while the Y electrode acts as the cathode. In the standard case, we observe that initially the surface charge distribution is symmetric with respect to the center of the sustain electrode gap. As the dielectric layer below the cathode is covered with positive charge, the discharge path moves towards the outer ends of the electrodes. This process continues until all the dielectric layer below the cathode is covered with positive charge, as previously discussed. In the new structure case, a quite different behavior is observed. The floating electrode below the cathode initially has a small charge density. The initial phase of the discharge does not differ substantially from the standard case (Figs. 5.9a, 5.9b and snapshots 1, 2 of Figs. 5.9c, 5.9d). However, in the new structure case as the discharge path moves towards the inner end of the floating electrode below the cathode, the surface

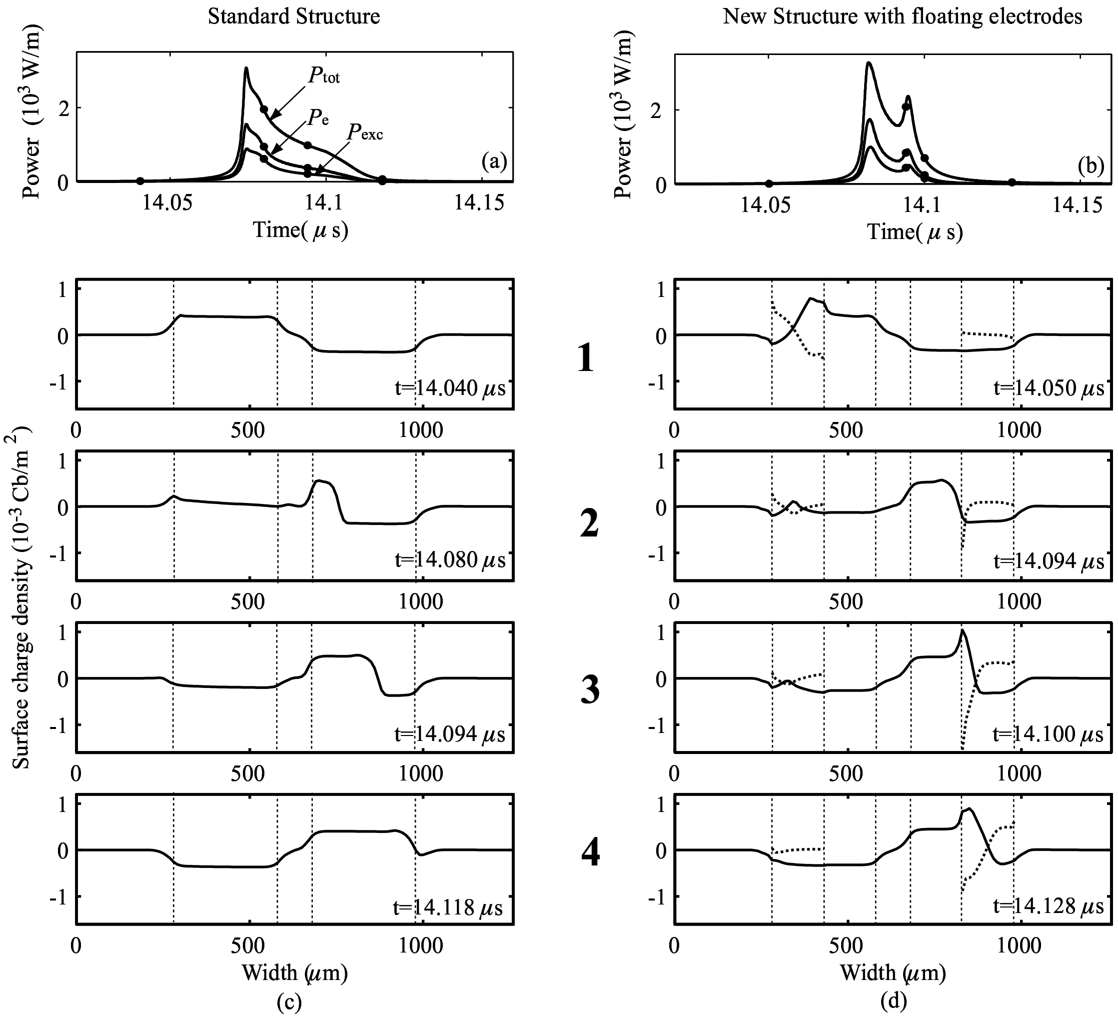

Figure 5.9 (a), (b) Dissipated total power $P_{\mathrm{tot}} = P_{\mathrm{e}} + P_{\mathrm{i}}$, dissipated electron power P_{e}, and power spent on Xe excitation P_{exc} for the standard and new structures respectively. (c) Snapshots of the surface charge density on the upper dielectric layer for the standard structure. (d) Snapshots of the surface charge density on the upper dielectric layer and on the floating electrodes (with dashed lines) for the new structure. The positions of electrodes are shown with dashed lines.

charge on the floating electrode is redistributed. Negative charge is attracted on the inner end of the floating electrode by the positive surface charge deposited on the dielectric layer and the positive space charge in the sheath region (snapshot 2 of Fig. 5.9d). As negative charge is accumulated in the inner end of the floating electrode, the electric field in the discharge path is enhanced, more positive charge has to be deposited on the dielectric layer before the discharge is quenched, and the discharge current consequently increases (Fig. 5.9b). In addition, since the total charge of the floating electrode is zero, positive charge is accumulated on the outer end of the floating electrode. The electric field of the sustain electrodes is screened by the positive charge, so that the discharge continues only until the dielectric layer below approximately the inner half of the floating electrode is covered with positive charge. This phenomenology explains the spatial confinement of the discharge in the new structure case, which was apparent in Figs. 5.8a,b.

5.4 Effect of self-erase discharge waveform

In this section, we investigate the effect of using an alternative sustaining waveform. Figure 5.10 shows the self-erase discharge waveform used for the simulations discussed in this section. The frequency of the waveform is 167 kHz and the rise and fall times of all pulses are 100ns. The duration of the sustain pulse is 2μs. Each sustain pulse is followed by an assistant pulse of opposite polarity and 1μs duration. The use of the self-erase discharge waveform has been proposed as a way to improve the efficiency of the PDP cell [*Hashimoto and Iwata*, 1999]. In the self-erase discharge waveform there is an idle period, between the application of the sustain pulses. Under certain conditions, surface charges on the upper dielectric layer deposited by the previous sustain discharge and space charges may cause a self-erase discharge during the idle period. Part of the charge deposited by the previous sustain discharge is erased. An assistant pulse may be applied during the idle period to promote the self-erase discharge [*Hashimoto and Iwata*, 1999].

We compared the waveform shown in Figure 3.6 with the self-erase discharge waveform shown in Figure 5.10, which will heretofore be referred as the standard and new waveforms respectively. When the new waveform is used, the address electrode is floating during the application of the sustaining waveform to prevent discharges between the address and sustain electrodes. The reference coplanar-electrode PDP cell was used. The amplitude of the sustaining voltage pulse is the same in both cases. We also investigate the effect of the

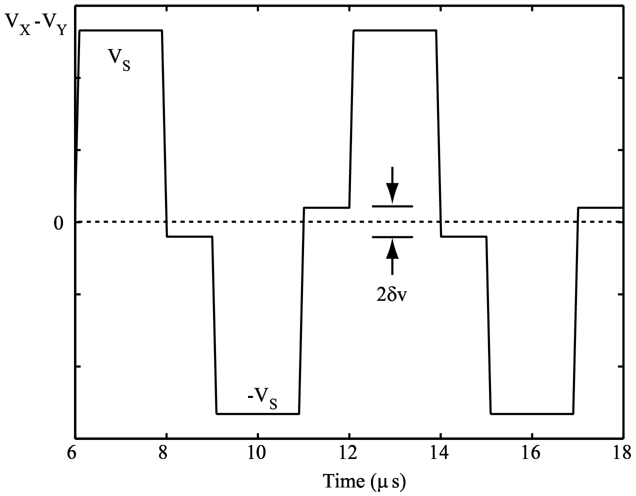

Figure 5.10 The self-erase discharge waveform used in the simulations of Section 5.4. The sustaining frequency is 167 kHz. The 2μs sustain pulses are followed by a 1μs assistant pulse. The address electrode is floating during the sustaining phase.

variation of the amplitude of the assistant pulse δv (Figure 5.10).

If no assistant pulse is used, the UV efficiency of the new waveform is ~17% higher than the UV efficiency of the standard waveform, in good agreement with the experimentally observed increase in the luminous efficiency [*Hashimoto and Iwata*, 1999]. When the new waveform is used, a self-erase discharge during the idle period erases part of the surface charge deposited by the previous sustain discharge, as mentioned above. As a result, the duration of the next sustain discharge, which is determined by the time required to cover the dielectric layer below the cathode with positive charge, is shorter. Every sustain discharge is characterized by an initial period where the electronic current dominates and a subsequent less efficient period where the ionic current in the sheath dominates. When the new waveform is used, the second less efficient period is shorter so that the overall efficiency is higher. In Figures 5.11a, 5.11b, and 5.11c we show the calculated UV efficiency, UV energy and dissipated energy per period respectively as a function of the assistant voltage δv. When comparing Figure 5.11b with Figure 5.2, it should be taken into account that time integration is over one period (6μs) in the first case, and over one sustain pulse (4μs) in the second case (Figs. 3.6, 5.10). The experimentally observed increase in luminance and luminous efficiency [*Hashimoto and Iwata*, 1999], when the assistant pulse is applied,

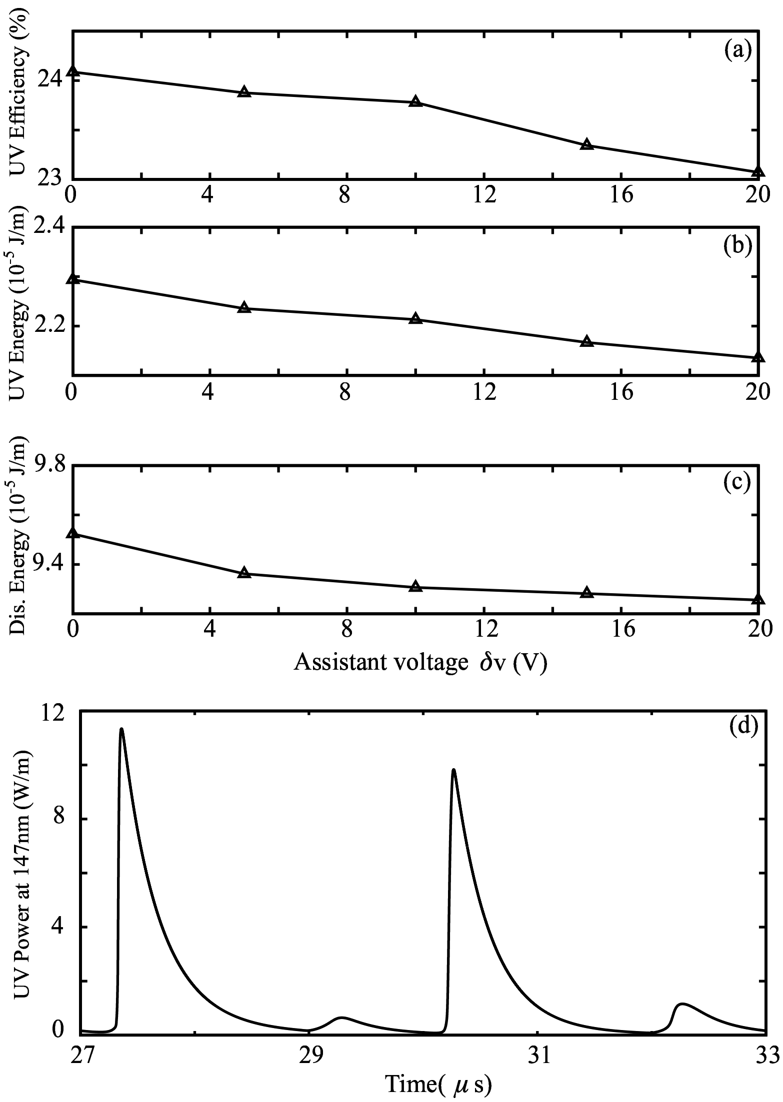

Figure 5.11 (a) UV efficiency as a function of the amplitude of the assistant pulse δv. (b) Total UV energy emitted per period as a function of the amplitude of the assistant pulse δv. (c) Dissipated energy per period as a function of the amplitude of the assistant pulse δv. (d) UV emission power at 147nm for δv=0. The two UV pulses caused by two subsequent sustain discharges have different amplitude. The two smaller UV pulses are caused by self-erase discharges during the idle period (Fig. 5.10).

is not reproduced by the simulation. When the standard waveform is used, UV light emission is periodic with period equal to one half of the sustaining period, due to the fact that UV pulses produced by sustaining pulses of opposite polarity are identical. When the new waveform is used, two subsequent sustain discharge pulses and consequently the two corresponding light pulses are not identical, as shown in Figure 5.11d. The two smaller UV pulses are caused by self-erase discharges during the idle period. This result is also observed in the experiment [*Hashimoto and Iwata*, 1999]. We found that in a sequence of two sustain discharge pulses, one of them has shorter duration and is more efficient for the reasons described above. In the experiment [*Hashimoto and Iwata*, 1999], it was observed that the luminance and luminous efficiency are maximized for δv=10V. This observation may be due to the fact that for the specific experimental conditions (cell geometry, driving scheme, gas mixture) this particular amplitude of the assistant pulse represents an optimal match between two subsequent sustain discharge pulses so that the overall efficiency is maximized.

Chapter 6

Efficient PDP cell geometry designs

6.1 Introduction

In this chapter, we consider several non-standard cell geometry designs and investigate in detail the effect of variations of the cell geometry design on the operating voltages and the efficiency of the device. The alternative cell designs are variations of the standard coplanar-electrode cell design used in most PDPs. In addition, we put forth new cell structures that result in optimum device performance and evaluate the dependence of PDP performance on the design parameters of these new structures. We use the two-dimensional (2-D) self-consistent model, which was described in Section 3.1, to simulate the microdischarges in PDP cells. In the remainder of the chapter, we present the results of our model for a new electrode-shaping geometry (Section 6.2), a dielectric-shaping geometry (Section 6.3), and the dependence of PDP cell performance on the design parameters of these new structures (Section 6.4).

6.2 Electrode-shaping geometry

The geometry of the standard coplanar-electrode PDP cell used in the simulations is as shown in Figure 3.2b. The output window of the device is supposed to be the top side of the upper dielectric layer, noting that the sustain electrodes are transparent. In all cases, the gas mixture filling the region between the dielectrics is a Xe-Ne mixture with 4% Xe at a pressure

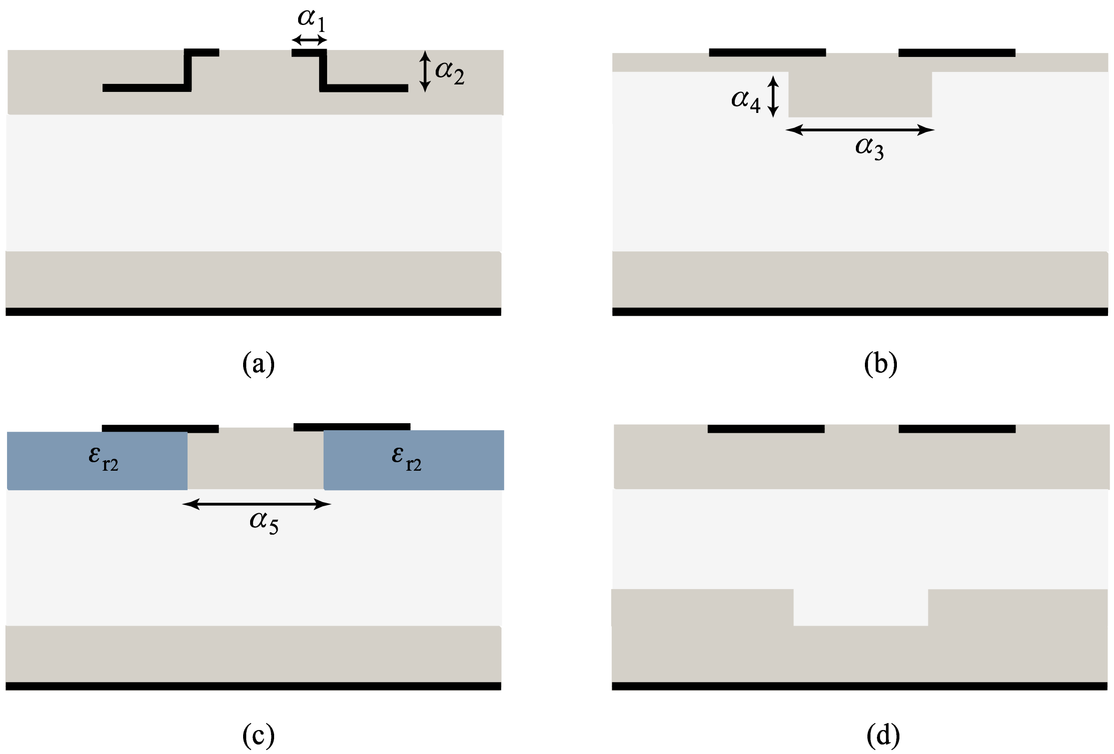

(a) (b) (c) (d)

Figure 6.1 (a) Schematic of the electrode-shaping geometry. (b) Schematic of the dielectric-shaping geometry. (c) Schematic of a geometry design involving two different dielectric layers. (d) Schematic of a geometry design with modified shape of the lower dielectric layer.

of 500 Torr. The height and width of the cell are H=210μm and L=1260μm respectively. Our reference case is characterized by the parameter values g=100μm, w=300μm, d_1=30μm, d_2=30μm, and ε_r=10, where g is the electrode gap length, w is the sustain electrode width, d_1,d_2 are the lengths of the upper and lower dielectric layers respectively, and ε_r is the dielectric constant. This reference case is the same as the one used in Chapter 5 (Section 5.2). The voltages applied to the three electrodes during the simulation are shown in Figure 3.6.

As in Chapter 5, we focus our attention on the operating voltages and the luminous efficiency of the PDP cell. In our studies, we investigate the effect of cell geometry design on the numerical values of the minimum sustaining voltage V_{Smin} and the firing voltage V_{f} (Section 1.2). The calculation of V_{Smin} and V_{f} is done as in Chapter 5 (Section 5.2.1). In cases of non-constant discharge gap length (e.g., Fig. 6.1b), we use the minimum value of the

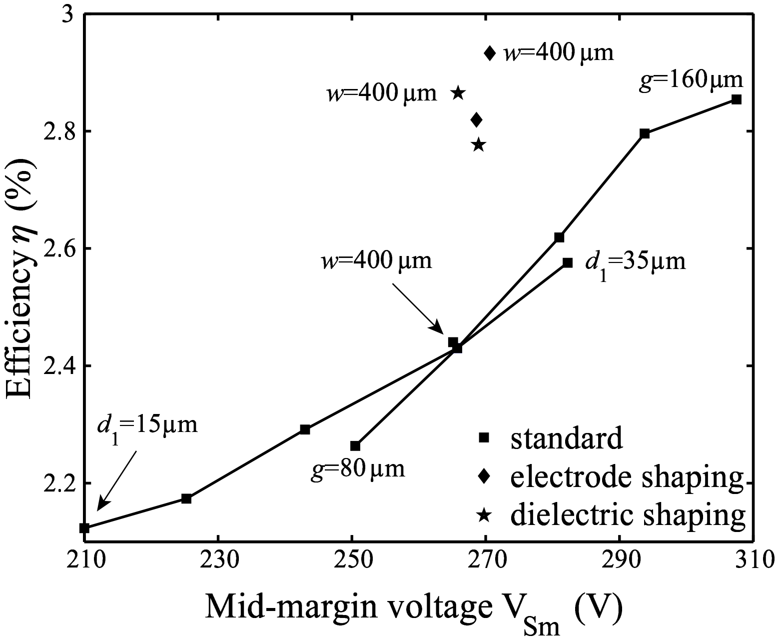

Figure 6.2 Luminous efficiency η and mid-margin voltage V_{Sm} of various cell geometry designs. Results are shown for the standard coplanar-electrode, the electrode-shaping, and the dielectric-shaping geometries. The effect of the variation of the sustain electrode gap length g and of the upper dielectric layer length d_1 is shown for the standard geometry. All other cell parameters are the same as in the reference case. Note that the reference case corresponds to the intersection point of the two curves.

gap length D_{min} in equation (5.1). As in Chapter 5, for the calculation of luminous efficiency η, as defined in (3.15), the sustaining voltage is chosen to be the mid-margin voltage, and the efficiency of the PDP cell is calculated in the periodic steady state, typically involving the application of at least 5 sustaining pulses (Section 5.2.2).

In the standard coplanar-electrode geometry there is a trade-off between high luminous efficiency and low operating voltages (Section 5.2.2)[*Veronis and Inan*, 2002a]. In Fig. 6.2 we show the effect of the variation of the sustain electrode gap length g (Fig. 3.2b) on the luminous efficiency η and the mid-margin voltage V_{Sm} of the PDP cell. We observe that larger values of g result in larger values of both η and V_{Sm}. Similarly, larger values of the length of the lower dielectric d_1 (Fig. 3.2b) results in larger values of both η and V_{Sm}.

Fig. 6.2, also shows the luminous efficiency η and mid-margin voltage V_{Sm} for alternative cell geometry designs. In Fig. 6.1a we show a PDP cell geometry with modified shape of sustain electrodes which for brevity will heretofore be referred to as the electrode-shaping geometry. This new design is characterized by the design parameters a_1 and a_2. Fig. 6.2 shows η and $V_{\rm Sm}$ for this electrode-shaping geometry with a_1=100μm and a_2=22.5μm, all other parameters being the same as in the reference case. We observe that the mid-margin voltage $V_{\rm Sm}$ is essentially the same as in the reference case, while the luminous efficiency η increases by ~16%. If a_1 and a_2 are kept constant, and the sustain electrode width w is increased from 300μm to 400μm, the increase in the luminous efficiency η with respect to the reference case is found to be ~20%, while the operating voltage increases by only a few volts. It should be noted that the substantial increase in η for the electrode-shaping geometry, when w is increased, is not observed in the standard coplanar-electrode geometry, as shown in Fig. 6.2. It should also be noted that for a given cell width L the sustain electrode width w has to be small enough to ensure that no undesired discharges occur with sustain electrodes of adjacent cells. Thus, there is a limit to the increase in efficiency that can be achieved in the electrode-shaping geometry by increasing w.

It is obvious from the results presented in Fig. 6.2 that the electrode-shaping geometry has better performance than the standard coplanar-electrode geometry of Fig. 3.2b. It results in increase in luminous efficiency without substantial increase of the operating voltages. The operating voltages remain the same because the structure in the middle of the cell is the same in both the standard coplanar-electrode and electrode-shaping geometries. Figures 6.3a and 6.3b show equipotential lines for the standard and the electrode-shaping geometries respectively. We observe that in both cases the electric field in the gap is maximum in the region between the two sustain electrodes in the cell center. As the applied voltage is increased, the breakdown condition first occurs in discharge paths in this high-field region. We observe that the electric field structure is the same for both designs in the high-field region and that the breakdown voltage is therefore not significantly different. In other words, the different shape of sustaining electrodes of the new structure does not significantly perturb the electric field distribution in the region where breakdown first occurs.

In order to better understand the reasons for the increase in the luminous efficiency, we focus our attention on the excitation efficiency $\eta_{\rm exc}$, as defined in (3.17). Our analyses indicate that the effect of cell geometry variations on η_3, as defined in (3.16), is small, because the rates of the reactions that lead to emission of UV photons from Xenon excited states are solely determined by the gas mixture composition. Similarly, the effect of cell geometry

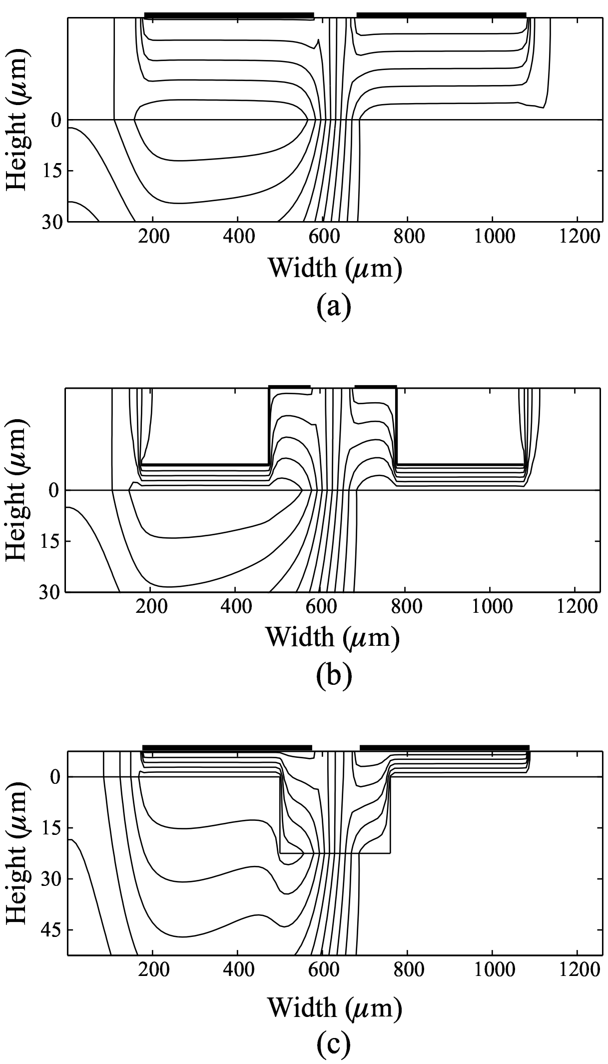

Figure 6.3 (a), (b), (c) Equipotential lines for the standard, the electrode-shaping, and the dielectric-shaping geometries respectively at the end of a sustaining period.

variations on η_4, as defined in (3.16), is small. Although we might expect that geometry variations could result in UV emission closer to the phosphor layer, and therefore higher η_4, the increase in η_4 is relatively small for the two-dimensional cell geometry variations considered herein. We therefore focus our attention on the excitation efficiency $\eta_{\mathrm{exc}} = \eta_1\eta_2$ representing the components of the overall efficiency most significantly affected by geometry variations.

In Figures 6.4a and 6.4b, we show the dissipated ion power, dissipated electron power, and power spent on Xe excitation in the PDP cell, as defined in (3.19), for the standard (Fig. 3.2b) and electrode-shaping (Fig. 6.1a) geometries respectively. Results are shown as a function of time, during the discharge caused by the 5th sustain pulse applied to the Y electrode starting at t=18μs. We observe that the duration of the discharge is shorter for the electrode-shaping geometry and that the peak power dissipation is higher by almost a factor of 3.

We may note that the excitation efficiency can also be written as in (5.2). Equation (5.2) suggests that the excitation efficiency η_{exc} is obtained by integrating (over space and time) the power spent for Xenon excitation (p_{exc}) normalized by the total energy dissipated in the discharge ($\varepsilon_{\mathrm{tot}}$). For purposes of brevity, this quantity, which is directly related to the excitation efficiency, will heretofore be referred to as the normalized power spent for Xenon excitation. In Figures 6.4c and 6.4d we show the normalized power spent for Xenon excitation, integrated over 5ns time intervals, for the standard (Fig. 3.2b) and electrode-shaping (Fig. 6.1a) geometries respectively. We observe that high excitation occurs both in the cathode sheath - plasma interface and in the bulk plasma regions [*Punset et al.*, 1999]. The bulk plasma excitation region is wider in the electrode-shaping geometry (snapshots 2, 3, 4 of Figs. 6.4c, 6.4d), for which the outer ends of the sustain electrodes are closer to the gap (Fig. 6.1a) so that the electric field is enhanced in the corresponding gap region. Due to the enhancement of the electric field in the outer parts of the gap, wider discharge paths become increasingly favorable in this new structure. We note that wider plasma region results in higher discharge efficiency. The cathode ion sheath region is characterized by high electric fields and high electron temperatures, while the bulk plasma region is characterized by much lower electric fields and consequently lower electron temperatures. In Fig. 6.5 we show $\eta_{\mathrm{exc},e}$, as defined in (3.21), as a function of electron mean energy, in constant uniform electric fields, obtained using ELENDIF [*Morgan and Penetrate*, 1990]. We observe that $\eta_{\mathrm{exc},e}$ is maximized at $\sim$4 eV. Our analyses indicate that, during the discharge, the electric

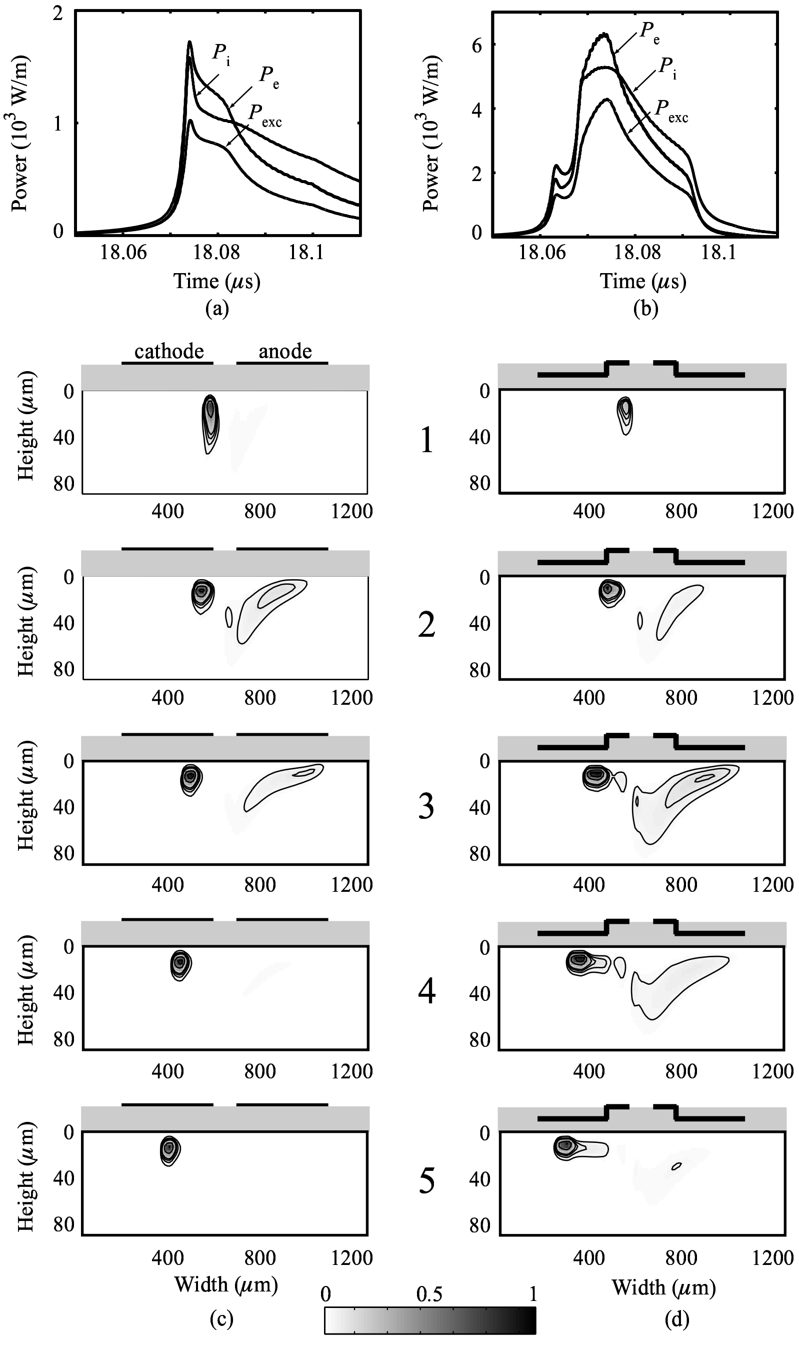

Figure 6.4 (a), (b) Dissipated ion power P_{i}, dissipated electron power P_{e}, and power spent on Xe excitation P_{exc} for the standard and electrode-shaping geometries respectively. (c), (d) Normalized power spent for Xenon excitation, integrated over 5ns consecutive time intervals, for the standard and electrode-shaping geometries respectively. The starting time for integration is 75ns and 70ns after the beginning of a sustaining period for the standard and electrode-shaping geometries respectively. The maximum in the gray scale corresponds to $1.73 \times 10^7\,\mathrm{m}^{-2}$. The contours correspond to 0.05, 0.1, 0.15, 0.2, 0.5, 0.8 of the maximum value. Note the different vertical scale in each plot. In all cases height is measured from the MgO layer surface.

field is high enough to sustain electron temperatures above this threshold in all regions of significant excitation. Local electron excitation efficiency $\tilde{\eta}_2$ [1] , as defined in (5.3), is therefore a decreasing function of electron temperature for PDP discharge conditions. It is for this reason that the bulk plasma region of the discharge is more efficient than the sheath region and that wider plasma region results in higher efficiency. In addition, we observe that the bulk plasma region in the electrode-shaping geometry is more efficient than the bulk plasma region of the standard structure (snapshots 2, 3 of Figs. 6.4c, 6.4d), due to lower electric fields and consequently lower electron temperatures in the bulk plasma region. Finally, we observe that the cathode sheath region is also more efficient in the electrode-shaping design (snapshots 4, 5 of Figs. 6.4c, 6.4d). Excitation is more confined in the cathode region of the standard structure. As mentioned above, the electric field is higher in the outer part of the gap in the electrode-shaping geometry. Electron temperatures are therefore higher and $\tilde{\eta}_2$ is lower. However, the excitation region in the cathode ion sheath for the electrode-shaping geometry includes a 'tail' region (snapshots 4, 5 of Fig. 6.4d) so that the cathode region is overall more efficient for this new structure. We found that the 'tail' excitation region is due to longer discharge duration in individual discharge paths in the electrode-shaping geometry, because it takes more time to produce (via ionization) the charge required to quench the discharge. For example, in the case presented in Fig. 6.4, the distance of the outer part of the sustain electrodes from the gap for the electrode-shaping design is 7.5μm, while that for the standard design it is 30μm. The equivalent capacitance and therefore the charge required to quench the discharge is thus four times larger in the electrode-shaping geometry. Although the electric field in the ion sheath is also much larger in the electrode-shaping geometry, the time required to quench the discharge is longer due to the highly nonlinear saturation effect of the ionization coefficient at high electric fields [*Raizer*, 1997, p. 57]. The partial covering of the dielectric layer with charge results in a prolonged discharge in a low electric field regime which favors high efficiency, as mentioned above. In summary, the new electrode-shaping geometry (Fig. 6.1a) is more efficient than the standard coplanar-electrode geometry (Fig. 3.2b), because the local excitation efficiency

---

[1] Note that, as we mentioned in Section 5.2.2, $\tilde{\eta}_2$ is not exactly the same as the fundamental inherent property of the gas mixture $\eta_{\mathrm{exc},e}$, defined by (3.21). The quantity $\eta_{\mathrm{exc},e}$ was defined to be a function of the reduced electric field E/N. Since we use the electron energy equation, the electron temperature in our model is determined by the solution of the electron energy equation and not by the local reduced electric field. In our model, the quantity $\tilde{\eta}_2$ is exactly the same as the quantity plotted in Fig. 6.5 if the electron mean energy (x-axis) is self-consistently calculated by solving the electron energy equation.

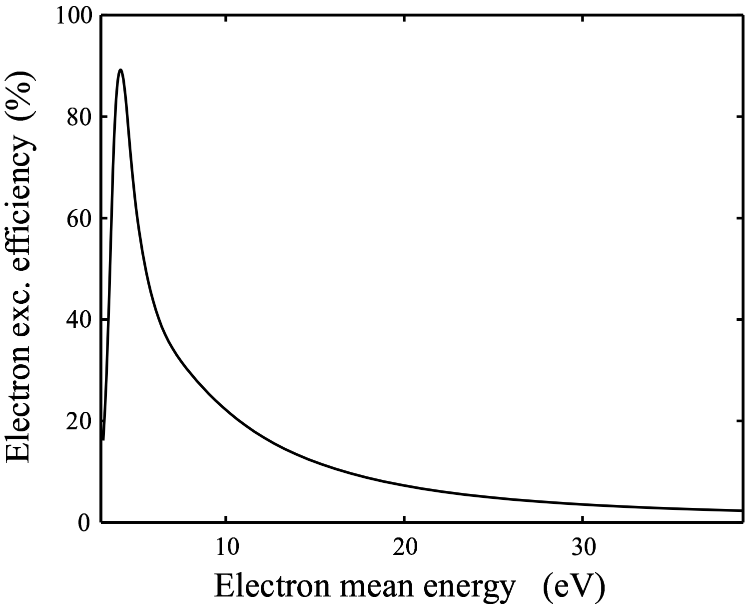

Figure 6.5 The electron excitation efficiency η_2 as a function of the electron mean energy.

is higher in both the cathode ion sheath and the bulk plasma region, and because the more efficient bulk plasma region is wider.

As we noted above, the overall duration of the discharge is shorter in the electrode-shaping geometry (Figs. 6.4a, 6.4b, and Figs. 6.4c, 6.4d). Once the sustain voltage pulse is applied, the time required to reach breakdown is shorter in discharge paths below the outer parts of the sustain electrodes in this new structure, due to the larger overvoltage [*Raizer*, 1997, p. 133]. Thus, the discharges in individual discharge paths in the electrode-shaping geometry initiate earlier but last longer.

6.3 Dielectric-shaping geometry

In Fig. 6.1b we show a PDP cell with modified shape of the upper dielectric which for brevity will heretofore be referred as the dielectric-shaping geometry. This design was first proposed (without the performance analysis presented here) in *Shon et al.* [2001] as a way to improve the efficiency of the PDP cell. The dielectric-shaping geometry is characterized by the design parameters a_3 and a_4. In Fig. 6.2 we show η and V_{Sm} for the dielectric-shaping geometry with $a_3=260\mu\text{m}$ and $a_4=22.5\mu\text{m}$. All other parameters are the same as in the reference case. We observe that the mid-margin voltage V_{Sm} is essentially the same as in the reference case, while the luminous efficiency η increases by $\sim$14%. As in the electrode-shaping geometry, if a_3 and a_4 are kept constant, and the sustain electrode width w is increased from $300\mu\text{m}$ to $400\mu\text{m}$, the increase in the luminous efficiency η with respect to the reference case is found to be $\sim$17%, while once again the operating voltage increases by only a few volts.

The dielectric-shaping geometry (Fig. 6.1b) has obviously better performance than the standard coplanar-electrode geometry (Fig. 3.2b) and results in larger luminous efficiency without substantial increases of the operating voltages, similarly to the electrode-shaping geometry (Fig. 6.1a). The similar behavior of the two new structures could be expected, since in both cases the modification in cell design basically results in larger equivalent capacitance of the outer part of the sustain electrodes. We found that the increase in the efficiency without any substantial increase of the operating voltages for the dielectric-shaping geometry can be interpreted in the same way as the improved performance of the electrode-shaping geometry, which was described above in detail. We should nevertheless note two important differences in the performance of these two new structures. Firstly, we observe in Fig. 6.2 that the electrode-shaping geometry has higher luminous efficiency than the dielectric-shaping geometry. Our analyses indicate that η_4 is higher for the electrode-shaping design. The region of high excitation and consequently high UV emission directly below the upper dielectric layer is closer to the phosphor layer in the case of the electrode-shaping design, so that more emitted UV photons reach the phosphor. Secondly, in Fig. 6.6a we show the dissipated ion power, dissipated electron power, and power spent on Xe excitation in the PDP cell, as defined in (3.19), for the dielectric-shaping geometry. We observe that the peak ionic current is much higher in the dielectric-shaping geometry in comparison with the electrode-shaping geometry. The very large increase in ionic current in the dielectric-shaping geometry is observed when the discharge in the cathode region reaches the point at which the upper dielectric layer length becomes shorter (Fig. 6.1b). We note that both of the alternative new structures are characterized by points of sharp variation of either the electrode shape (Fig. 6.1a) or the upper dielectric shape (Fig. 6.1b). The electric field is very large in the vicinity of the sharp points, as is shown in the equipotential contours in

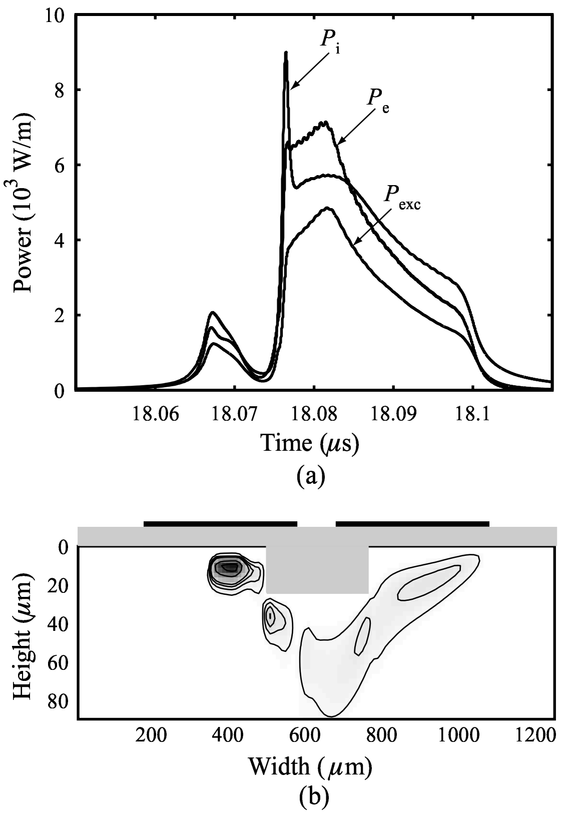

Figure 6.6 (a) Dissipated ion power P_i, dissipated electron power P_e, and power spent on Xe excitation P_exc for the dielectric-shaping geometry. (b) Normalized power spent for Xenon excitation, integrated over a 5ns time interval, for the dielectric-shaping geometry. The starting time for integration is 80ns after the beginning of a sustaining period. The increment between the contours and maximum in gray scale are the same as in Figures 6.4c and 6.4d. Note the different vertical scale. Height is measured from the MgO layer surface.

Figs. 6.3b and 6.3c for the electrode-shaping and the dielectric-shaping geometries respectively. However, in the case of the electrode-shaping geometry, the sharp point is inside the dielectric layer so that the increase in the ionic current in the cathode sheath region is not as dramatic as that observed in the dielectric-shaping geometry. Finally, in Fig. 6.6b we show the normalized power spent for Xenon excitation, integrated over a 5ns time interval, for the dielectric-shaping geometry for comparison with the standard (Fig. 6.4c) and the electrode-shaping geometries (Fig. 6.4d).

6.4 Dependence of cell performance on design parameters

We now investigate the effect of the design parameters of the new PDP cell structures on the luminous efficiency and the operating voltages of the PDP cell. Figs. 6.7a, 6.7c show the dependence of η, and of V_{f}, V_{Smin}, V_{Sm} respectively on parameter a_1 of the electrode-shaping geometry (Fig. 6.1a). We note that $a_1 = 0$ corresponds to a cell design with the sustain electrodes fully inserted in the upper dielectric layer. As expected, analyses indicate that this design has essentially no difference in performance from a standard coplanar-electrode design (Fig. 3.2b) having the same distance of sustain electrodes from the gap. We also note that $a_1 = w$ corresponds to the standard coplanar-electrode design. We observe that as a_1 is increased, both the efficiency and the operating voltages increase. The efficiency is maximized for $a_1 = 100\mu$m, with any further increases of a_1 leading only to increase in the operating voltages. We conclude that the electrode-shaping geometry has better performance than both the standard coplanar-electrode design (Fig. 3.2b) and the equivalent design with the standard sustain electrodes fully inserted in the upper dielectric layer. In addition, for a specific value of a_2 there appears to be an optimum value of a_1. In Figs. 6.7b, 6.7d we show the dependence of η, and of V_{f}, V_{Smin}, V_{Sm} respectively on the parameter a_2 of the electrode-shaping geometry, noting that $a_2 = 0$ corresponds to the standard coplanar-electrode design. We observe that the luminous efficiency of the PDP cell increases substantially as a_2 is increased, while the operating voltages remain essentially the same. The interpretation of the improved performance of this new structure (Fig. 6.1a) was discussed in detail in Section 6.2. Figure 6.7 further shows that the increase in efficiency is maximized for $a_2 = 22.5\mu$m. Analyses indicate that for large values of a_2 the efficiency of the discharge in heating the electrons η_1 is a decreasing function of a_2. As a_2 is increased, the electric field in the ion sheath region increases and the sheath length decreases. As a result,

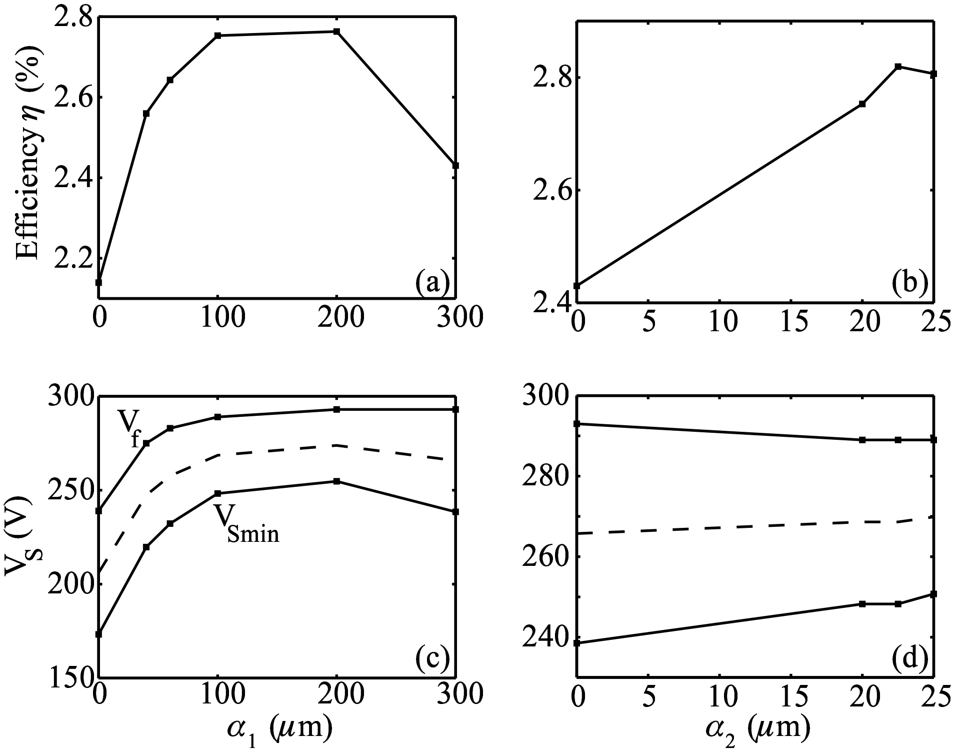

Figure 6.7 (a) Luminous efficiency η as a function of parameter a_1 of the electrode-shaping geometry for a_2 =20μm (Fig. 6.1a). All other cell parameters are the same as in the reference case. (b) η as a function of parameter a_2 of the electrode-shaping geometry for a_1 =100μm (Fig. 6.1a). All other cell parameters are the same as in the reference case. (c) The firing voltage V_f and the minimum sustaining voltage V_{Smin} as a function of a_1. The dashed line shows the mid-margin sustaining voltage V_{Sm} used for the calculation of the efficiency. (d) V_f, V_{Smin}, and V_{Sm} as a function of a_2.

the efficiency of the discharge in heating the electrons in the sheath region is a decreasing function of a_2. This effect dominates for large values of a_2 and results in a decrease of η_1 and subsequently of η.

Figs. 6.8a, 6.8c, and 6.8b, 6.8d show similar results for the dielectric-shaping design and the equivalent design of Fig. 6.1c respectively. The structure of Fig. 6.1c was first proposed (without the performance analysis presented here) in *Shon et al.* [2001] as a way to improve the efficiency of the PDP cell. The increase of the equivalent capacitance of the outer part of the sustain electrodes in this case is achieved by using a material with a larger dielectric constant ε_r in parts of the upper dielectric layer. Figs. 6.8a, 6.8c show the dependence of η,

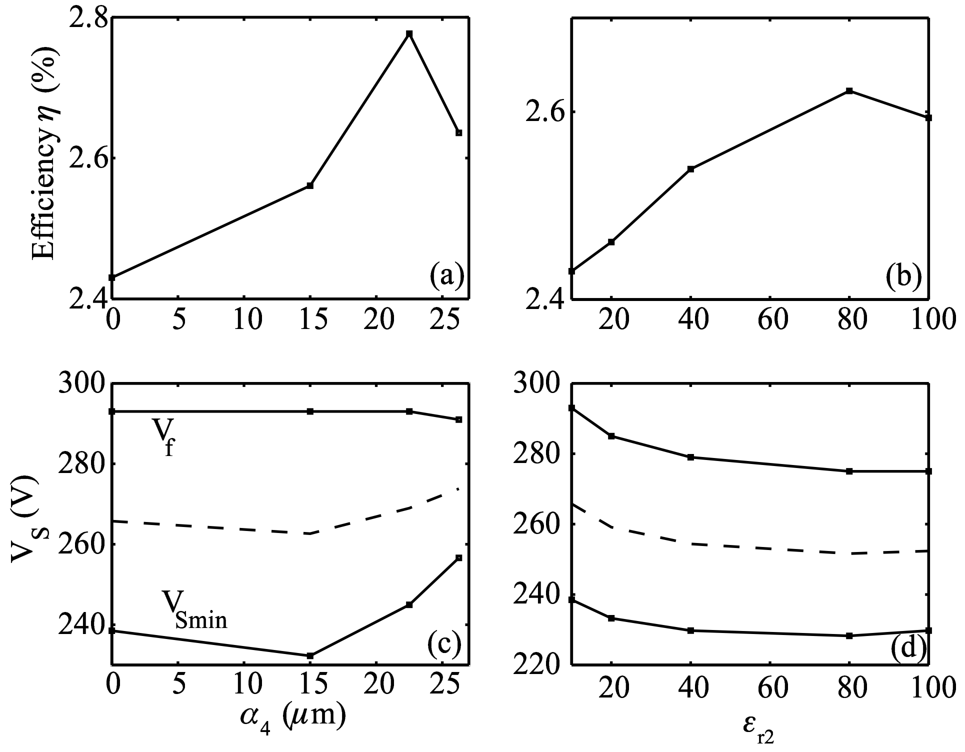

Figure 6.8 (a) Luminous efficiency η as a function of parameter a_4 of the dielectric-shaping geometry for a_3=260μm (Fig. 6.1b). All other cell parameters are the same as in the reference case. (b) η as a function of the dielectric constant ε_{r2} of the geometry of Fig. 6.1c for a_5=200μm. All other cell parameters are the same as in the reference case. (c) The firing voltage V_{f} and the minimum sustaining voltage V_{Smin} as a function of a_4. The dashed line shows the mid-margin sustaining voltage V_{Sm} used for the calculation of the efficiency. (d) V_{f}, V_{Smin}, and V_{Sm} as a function of ε_{r2}.

and of V_{f}, V_{Smin}, V_{Sm} respectively on parameter a_4 of the dielectric-shaping geometry (Fig. 6.1b), while Figs. 6.8b, 6.8d show the dependence of η, and of V_{f}, V_{Smin}, V_{Sm} respectively on the dielectric constant ε_{r2} of the geometry of Fig. 6.1c. In both cases, we observe dependences that are similar to those noted for the electrode-shaping geometry. In all three cases, the larger equivalent capacitance of the outer part of the sustain electrodes results in larger luminous efficiency of the PDP cell without significant change in the operating voltages. The increase in the efficiency of the device is maximized for a specific value of the corresponding design parameter in each case for reasons described above.

We note that combination of the three different ways of increasing the equivalent capacitance of the outer part of the sustain electrodes does not result in further increase in efficiency. For example, Figure 6.7 shows that the efficiency of the electrode-shaping geometry is maximized for $a_2 = 22.5\mu$m. If the equivalent capacitance is further increased by increasing a_2, the efficiency decreases. We verified that, as expected, if the equivalent capacitance is increased, by either the dielectric-shaping or the dielectric constant methods, the efficiency still decreases.

For the two-dimensional cell geometry variations considered in this article, the electrode shape of the structure of Fig. 6.1a is found to be optimal. For this purpose, we considered alternative shapes of sustain electrodes, for example, a cell design with slanted sustain electrodes [*Shin et al.*, 1999]. In such a design, the equivalent capacitance increases linearly with distance rather than sharply as in Fig. 6.1a, and results in lower efficiency. The structure of Fig. 6.1a is optimal because it is identical to the standard structure in the middle of the cell (Fig. 3.2b), so that the operating voltages do not change, while in the outer part of the cell it results in higher equivalent capacitance and higher luminous efficiency. We also examined the effect of variations of the lower dielectric layer on the performance of the cell, for example as shown in Fig. 6.1d. Such a design results in wider discharge area and consequently higher excitation efficiency η_{exc} for the reasons described above. However, the overall efficiency η is not larger than the efficiency of the standard structure (Fig. 3.2b). Analyses indicate that the modification of the lower dielectric layer shape and consequently of the phosphor layer shape in the structure of Fig. 6.1d results in lower η_4. This result is consistent with the fact that most of the visible photons emitted from the vertical sides of the phosphor layer are lost.

Chapter 7

Summary and suggestions for future work

7.1 Summary of results

We have considered the fundamental kinetic behavior under an applied electric field of homogeneous, unbounded inert gas mixtures to compare the breakdown field and electron excitation efficiency of Ne-Xe, He-Xe and Ne-Xe-Ar mixtures used in PDPs. Electron excitation efficiency is an increasing function of Xe concentration in Ne-Xe and He-Xe mixtures, although He-Xe mixtures were found to be less efficient than Ne-Xe mixtures with the same Xe concentration. The fractional increase in electron excitation efficiency is found to be very small for $N_{\mathrm{Xe}} > 0.1N$. For Ne-Xe mixtures with $N_{\mathrm{Xe}}/N_{\mathrm{Ne}} = 5/95$, addition of a small amount of Ar results in a slight minimum in the breakdown field at $N_{\mathrm{Ar}}/N \simeq 0.01$, while the electron excitation efficiency increases only slightly. For Ne-Xe mixtures with $N_{\mathrm{Xe}}/N_{\mathrm{Ne}} = 10/90$, addition of a small amount of Ar increases the breakdown field. Based on these results, addition of Ar to Ne-Xe mixtures does not lead to any significant improvement in PDP performance, either in terms of electron excitation efficiency or breakdown voltage level. Using a one-dimensional model of an AC PDP cell, we confirmed the validity of the conclusions derived by the homogeneous and unbounded kinetic model [*Veronis et al.*, 2000].

In addition, we used a two-dimensional self-consistent model to investigate the effect of the variation of the cell design parameters on the operating voltages and UV efficiency of a coplanar-electrode PDP cell. As the sustain electrode gap g or the upper dielectric length d_1

is increased, or as the dielectric constant ε_r is decreased both the efficiency and the operating voltages increase. If the sustain electrode width w is varied, there is no significant change in either the efficiency or in the operating voltages. Analysis of the factors that determine the UV efficiency showed that the wider the discharge area the higher the efficiency. We also used the model to investigate the effect of the insertion of floating electrodes in the upper dielectric layer. We found that, if this new structure is used, the same total amount of UV light can be emitted in a more confined area, thus limiting cross talk with adjacent cells, while efficiency decreases by ~8%. We also investigated the effect of applying a self-erase discharge sustaining voltage waveform. Use of this new waveform results in ~17% increase of the UV efficiency, although the experimentally observed further increase of the efficiency when assistant pulses are used was not reproduced by the simulation [*Veronis and Inan*, 2002a].

Finally, we used the two-dimensional self-consistent model to investigate the performance of several non-standard plasma display panel cell geometry designs. The model was used to calculate the voltage margin and the steady state luminous efficiency of PDP cells at their mid-margin sustaining voltage. A cell design with modified shape of sustain electrodes was found to have ~20% larger luminous efficiency, without substantial increase of the operating voltages, when compared to the standard coplanar-electrode design. A cell design with modified shape of the upper dielectric was found to have ~17% larger luminous efficiency, once again without substantial increase of the operating voltages. Similar performance improvement is achieved by a design involving two different dielectric layers. The new geometries are more efficient than the standard coplanar-electrode geometry, because the local excitation efficiency is higher in both the cathode ion sheath and the bulk plasma region, and because the more efficient bulk plasma region is wider, due to the increase of the equivalent capacitance of the outer part of the sustain electrodes. Detailed investigation of the dependence of cell performance on the design parameters of these structures indicates that the increase of luminous efficiency is maximized for specific values of the corresponding design parameter in each case. Other designs involving alternative shaping of the sustain electrodes or of the lower dielectric layer were found to be less efficient [*Veronis and Inan*, 2002b].

7.2 Suggestions for future work

The two-dimensional model of PDP cells should be extended in three dimensions. First, the two-dimensional variations of the standard coplanar-electrode PDP cell proposed in this dissertation (modified shape of sustain electrodes, modified shape of the upper dielectric, two different dielectric layers) should be optimized in three dimensions. In addition, a three-dimensional model will enable the investigation of new non-standard cell geometry designs involving three-dimensional variations of the coplanar-electrode PDP cell.

In this dissertation, we investigated the effect of gas mixture (Chapter 4), and cell geometry (Chapters 5, and 6) on the performance of PDP cells. The effect of non-standard voltage waveforms should also be investigated. In Section 5.4, we found that the self-erase discharge sustaining voltage waveform proposed by *Hashimoto and Iwata* [1999] results in ~17% increase of the UV efficiency. The effect of voltage pulse shape on the performance of the device should be investigated in detail. It is interesting to note that the models suggest that the discharge initiates during the rise time of the voltage pulse (Fig. 3.7). Thus, variation of the pulse shape during its rise time could possibly affect the PDP efficiency.

It is also important to fabricate and test the new geometries proposed in this dissertation (Chapter 6). Model displays should be fabricated and tested. The voltage margin as well as the luminous efficiency of the display should be measured. As we mentioned in Section 1.3, PDP cells are small and provide limited access for diagnostic measurements. As a result, experimental studies of the transient plasma discharges in PDPs are extremely difficult. Thus, experimental studies usually focus on measurement of operating voltages and luminous efficiency. Alternatively, macroscopic plasma display cells can be designed in order to more easily study the plasma evolution in PDP discharges [*Callegari et al.*, 2000]. The dimensions of the macro-cells are typically 100 times larger and the gas pressure is 100 times smaller. Although some of the properties of the discharge pulse do not follow the classical similarity laws [*Raizer*, 1997, p. 133], the macro-cells can be a useful tool for improving our understanding of discharges in PDP cells.

Over the last few years, PDP manufacturers developed displays with luminous efficiency of ~1.2 lm/W. With improvements in the cell geometry and voltage driving waveforms, there is a good prospect of achieving a luminous efficiency of 2-3 lm/W [*Uchiike and Hirakawa*, 2002].

Bibliography

[*Birdsall*, 1991] Birdsall, C. K., Particle-in-cell charged-particle simulations, plus Monte Carlo collisions with neutral atoms, PIC-MCC, *IEEE Trans. Plasm. Sci.* **19**, 65 (1991).

[*Bittencourt*, 1995] Bittencourt J. A., *Fundamentals of Plasma Physics*, (FAPESP, Sao Jose dos Campos, 1995).

[*Blanc*, 1908] Blanc A., Mobility of ions in gases, *J. Phys.* **7**, 825 (1908).

[*Boeuf*, 1987] Boeuf, J. P., Numerical model of RF glow discharges, *Phys. Rev. A* **36**, 2782 (1987).

[*Boeuf et al.*, 1997] Boeuf J. P., C. Punset, and H. Doyeux, Physics and modeling of plasma display panels, *J. Phys. IV* **7**, C4, 3 (1997).

[*Callegari et al.*, 2000] Callegari T., R. Ganter, and J. P. Boeuf, Diagnostics and modeling of a macroscopic plasma display panel cell, *J. Appl. Phys.* **88**, 3905 (2000).

[*Chen*, 1977] Chen F. F., *Introduction to Plasma Physics*, (Plenum Press, New York, 1977).

[*Ellis et al.*, 1976] Ellis H. W., R. Y. Pai, E. W. McDaniel, E. A. Mason, and L. A. Viehland, Transport properties of gaseous ions over a wide energy range, *At. Data Nucl. Data Tables* **17**, 177 (1976).

[*Ellis et al.*, 1978] Ellis H. W., E. W. McDaniel, D. L. Albritton, L. A. Viehland, S. L. Lin, and E. A. Mason, Transport properties of gaseous ions over a wide energy range II, *At. Data Nucl. Data Tables* **22**, 179 (1978).

[*Ellis et al.*, 1984] Ellis H. W., M. G. Thackston, E. W. McDaniel, and E. A. Mason, Transport properties of gaseous ions over a wide energy range III, *At. Data Nucl. Data Tables* **31**, 113 (1984).

[*Elsbergen et al.*, 2000] Elsbergen V., P. K. Bachmann, and T. Juestel, Ion-induced secondary electron emission: a comparative study, *SID'00 Digest*, (2000), p.220.

[*Hagelaar et al.*, 2000] Hagelaar G. J. M., and G. M. W. Kroesen, Speeding up fluid models for gas discharges by implicit treatment of the electron energy source term, *J. Comput. Phys.* **159**, 1 (2000).

[*Hagelaar et al.*, 2001] Hagelaar G. J. M., M. H. Klein, R. J. M. M. Snijkers, and G. M. W. Kroesen, Energy loss mechanisms in the microdischarges in plasma display panels, *J. Appl. Phys.* **89**, 2033 (2001).

[*Hashimoto and Iwata*, 1999] Hashimoto T., and A. Iwata, Improvement of luminance efficiency in an ACPDP by self-erase discharge waveform, *SID'99 Digest*, (1999), p.540.

[*Hashimoto et al.*, 2001] Hashimoto Y., Y. Seo, O. Toyoda, K. Betsui, T. Kosaka, and F. Namiki, High-luminance and highly luminous-efficient AC-PDP with DelTA cell structure, *SID'01 Digest*, (2001), p.1328.

[*Hockney and Eastwood*, 1981] Hockney R. W., and J. W. Eastwood, *Computer Simulation Using Particles*, (McGraw-Hill, New York, 1981).

[*Holstein*, 1947] Holstein T., Imprisonment of resonance radiation in gases, *Phys Rev.* **72**, 1212 (1947).

[*Holstein*, 1951] Holstein T., Imprisonment of resonance radiation in gases II, *Phys Rev.* **83**, 1159 (1951).

[*Kamegaya*, 1990] Kamegaya T., *Electronic Display Devices*, edited by S. Matsumoto, (Wiley, New York, 1990).

[*Kanazawa et al.*, 1999] Kanazawa Y., T. Ueda, S. Kuroki, K. Kariya, and T. Hirose, High-resolution interlaced addressing for plasma displays, *SID'99 Digest*, (1999), p.154.

[*Kang et al.*, 2000] Kang J., O. D. Kim, W. G. Jeon, J. W. Song, J. Park, J. R. Lim, and J. P. Boeuf, Panel performance of RF PDP, *IDW'00*, (2000), p.643.

[*Kannari et al.*, 1983] Kannari F., A. Suda, M. Obara, and T. Fujioka, Theoretical simulation of electron-beam-excited xenon-chloride (XeCl) lasers, *IEEE J. Quantum Electron.* **QE-19**, 1587 (1983).

[*Kim et al.*, 2000] Kim J. S., C. H. Jeon, E. C. Lee, Y. J. Ahn, S. D. Kang, S. Y. Ahn, Y. K. Shin, J. H. Ryu, and J. D. Schemerhorn, Application of the new panel structure for high luminous efficiency in AC-PDPs, *SID'00 Digest*, (2000), p.102.

[*Levin et al.*, 1981] Levin L. A., S. E. Moody, E. L. Klosterman, R. E. Center, and J. J. Ewing, Kinetic model for long-pulse XeCl laser performance, *IEEE J. Quantum Electron.* **QE-17**, 2282 (1981).

[*Lieberman and Lichtenberg*, 1994] Lieberman M. A., and A. J. Lichtenberg, *Principles of Plasma Discharges and Materials Processing*, (Wiley, New York, 1994).

[*Meek and Craggs*, 1978] Meek J. M. and J. D. Craggs, *Electrical Breakdown of Gases*, (Wiley, New York, 1978).

[*Meunier et al.*, 1995] Meunier J., Ph. Belenguer, and J. P. Boeuf, Numerical model of an ac plasma display panel cell in neon-xenon mixtures, *J. Appl. Phys.* **78**, 731 (1995).

[*Morgan and Penetrate*, 1990] Morgan W. L., and B. M. Penetrante, ELENDIF: a time-dependent Boltzmann solver for partially ionized plasmas, *Comp. Phys. Com.* **58**, 127 (1990).

[*Noborio et al.*, 1994] Noborio M., T. Yoshioka, Y. Sano, and K. Nunomura, (He,Ne)-Xe gas mixtures for high-luminance color ac PDP, *SID'94 Digest*, (1994), p.727.

[*Oversluizen et al.*, 2000] Oversluizen G., S. de Zwart, S. van Heusden, and T. Dekker, Dependence of PDP efficacy on the gas pressure, *IDW'00*, (2000), p.631.

[*Penning*, 1934] Penning F. M., The starting potential of the glow discharge in neon argon mixtures between large parallel plates, *Physica* **1**, 1028 (1934).

[*Penning*, 1957] Penning F. M., *Electrical Discharges in Gases*, (The Macmillan Company, New York, 1957).

[*Phelps and Petrovic*, 1999] Phelps, A. V., Z. L. Petrovic, Cold-cathode discharges and breakdown in argon: surface and gas phase production of secondary electrons, *Plasma Sources Sci. Technol.* **8**, R21 (1999).

[*Punset et al.*, 1998] Punset C., J. P. Boeuf, and L. C. Pitchford, Two-dimensional simulation of an alternating current matrix plasma display cell: Cross-talk and other geometric effects, *J. Appl. Phys.* **83**, 1884 (1998).

[*Punset et al.*, 1999] Punset C., S. Cany, and J. P. Boeuf, Addressing and sustaining in alternating current coplanar plasma display panels, *J. Appl. Phys.* **86**, 124 (1999).

[*Raizer*, 1997] Raizer Y. P., *Gas Discharge Physics*, (Springer, Berlin, 1997).

[*Rauf and Kushner*, 1999a] Rauf S., and M. J. Kushner, Dynamics of a coplanar-electrode plasma display panel cell. I. Basic operation, *J. Appl. Phys.* **85**, 3460 (1999).

[*Rauf and Kushner*, 1999b] Rauf S., and M. J. Kushner, Dynamics of a coplanar-electrode plasma display panel. II. Cell optimization, *J. Appl. Phys.* **85**, 3470 (1999).

[*Sahni et al.*, 1978] Sahni O., C. Lanza, and W. E. Howard, One-dimensional numerical simulation of ac discharges in a high-pressure mixture of Ne+0.1% Ar confined to a narrow gap between insulated metal electrodes, *J. Appl. Phys.,* **49**, 2365 (1978).

[*Sakai et al.*, 1991] Sakai Y., S. Sawada, and H. Tagashira, Boltzmann equation analyses of electron swarm parameters in Ar/Ne, Kr/Ne, Xe/Ne, Hg/Ar and Hg/Kr mixtures and derived effective excitation cross sections for metastable states of rare atoms, *J. Phys. D* **24**, 283 (1991).

[*Scharfetter and Gummel*, 1969] Scharfetter D. L., and H. K. Gummel, Large-signal analysis of a silicon Read diode oscillator, *IEEE Trans. Electron Devices* **ED-16**, 64 (1969).

[*Seager*, 1988] Seager M. K., A SLAP for the masses, *LLNL Technical Report UCRL-100195* (1988).

[*Shin et al.*, 1999] Shin K. J., J. H. Ryu, and M. H. Park, A high luminous efficiency V-shaped electrode structure with a high Xe ratio gas, *SID'99 Digest*, (1999), p.544.

[*Shinoda*, 1998] Shinoda, T., Research and development of surface-discharge color plasma display technologies, *Asia Display '98*, (1998), p. 1065.

[*Shinoda et al.*, 2000] Shinoda T., M. Wakitani, T. Nanto, N. Awaji, and S. Kanagu, Development of panel structure for a high-resolution 21-in-diagonal full-color surface-discharge plasma display panel, *IEEE Trans. Electron Devices* **47**, 77 (2000).

[*Shon et al.*, 2001] Shon C. H., J. K. Lee, H. C. Kim, S. Dastgeer, S. S. Yang, and S. W. Shin, Striation phenomenon of plasma display panel (PDP) cell and its application to efficiency improvement, *SID'01 Digest*, (2001), p.767.

[*Siglo Series*, 1998] http://www.siglo-kinema.com/database/xsect/siglo.sec

[*Slottow and Petty*, 1971] Slottow H. G. and W. D. Petty, Stability of discharge series in the plasma display panel, *IEEE Trans. Electron Devices* **ED-18**, 650 (1971).

[*Sobel*, 1998] Sobel A., Television's bright new technology, *Sci. Am.* **278**, 70 (1998).

[*Sommerer et al.*, 1991] Sommerer, T. J., W. N. G. Hichon, R. E. P. Harvey, and J. E. Lawler, Self-consistent kinetic calculations of helium RF glow discharges, *Phys. Rev. A* **43**, 4452 (1991).

[*Straaten and Kushner*, 2000] Straaten T., and M. J. Kushner, A Monte-Carlo model of xenon resonance radiation transport in a plasma display panel cell: Transition from optically thick to thin regimes, *J. Appl. Phys.* **87**, 2700 (2000).

[*Uchiike and Hirakawa*, 2002] Uchiike H., and T. Hirakawa, Color plasma displays, *Proc. IEEE* **90**, 533 (2002).

[*Veerasingam et al.*, 1995] Veerasingam R., R. B. Campbell, and R. T. McGrath, One-dimensional fluid and circuit simulation of an AC plasma display cell, *IEEE Trans. Plasma Sci.* **23**, 688 (1995).

[*Veerasingam et al.*, 1996] Veerasingam R., R. B. Campbell, and R. T. McGrath, One-dimensional single and multipulse simulations of the ON/OFF voltages and the bistable margin for He, Xe, and He/Xe filled plasma display pixels, *IEEE Trans. Plasma Sci.* **24**, 1399 (1996).

[*Ventzek et al.*, 1994] Ventzek P. L. G., R. J. Hoekstra, and M. J. Kushner, Two-dimensional modeling of high plasma density inductively coupled sources for materials processing, *J. Vac. Sci. Technol. B* **12**, 461 (1994).

[*Veronis et al.*, 2000] Veronis G., U. S. Inan, and V. P. Pasko, Fundamental properties of inert gas mixtures for plasma display panels, *IEEE Trans. Plasma Sci.* **28**, 1271 (2000).

[*Veronis and Inan*, 2002a] Veronis G., and U. S. Inan, Simulation studies of the coplanar-electrode and other plasma display panel cell designs, *J. Appl. Phys.* **91**, 9502 (2002).

[*Veronis and Inan*, 2002b] Veronis G., and U. S. Inan, Cell geometry designs for efficient plasma display panels, *J. Appl. Phys.* (submitted).

[*Yoon et al.*, 2001] Yoon C. K., Y. J. Kim, J. H. Seo, M. S. Yoo, C. B. Park, W. J. Chung, J. H. Yang, K.-W. Whang, and K. C. Choi, Luminous characteristics analysis of a new SDR cell structure AC PDP, *SID'01 Digest*, (2001), p.1332.